UT GSBS Dissertations and Theses (Open Access)   Graduate School of Biomedical Sciences

12-2013

Scanned Ion Beam Therapy for Thoracic Tumors

John Gordon Eley

The TMC LIBRARY
Health Sciences Resource Center

SCANNED ION BEAM THERAPY
FOR THORACIC TUMORS

by

John Gordon Eley, M.S.
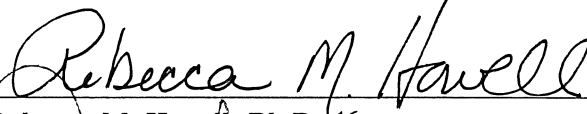
APPROVED

_____

Wayne D. Newhauser, Ph.D., Advisor

_____
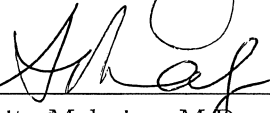
Christoph Bert, Ph.D.

_____
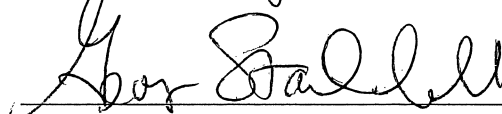
Rebecca M. Howell, Ph.D.

_____

Carol Etzel, Ph.D.

_____

Anita Mahajan, M.D.

_____

George Starkschall, Ph.D.

SCANNED ION BEAM THERAPY
FOR THORACIC TUMORS

A

DISSERTATION

Presented to the Faculty of
The University of Texas
Health Science Center at Houston
and
The University of Texas
M. D. Anderson Cancer Center
Graduate School of Biomedical Sciences

in Partial fulfillment
of the Requirements
for the Degree of

DOCTOR OF PHILOSOPHY

by

John Gordon Eley
M.S., Louisiana State University, 2009
B.S., College of Charleston, 2005

December 2013

This work is dedicated to Dargan Lee.

I am grateful for her love and her constant support during my education.

Acknowledgements

I thank my advisor Wayne Newhauser for leading me into a wonderful research field and for encouraging my research abroad in Germany during my dissertation work. His dedication to teaching students how to think logically and to see new opportunities in science has been inspiring, and I hope to pass on similar gifts to my own students in the future.

I thank Marco Durante for hosting my research visits to the GSI Helmholtzzentrum für Schwerionenforschung in Darmstadt. I especially thank Christoph Bert for supervising my research work at GSI. His mentorship was exceptional, and I will always look to him as a role model as I strive to become an excellent teacher and leader.

I am grateful for the support of the entire medical physics group at GSI: Robert Lüchtenborg, Christian Graeff, Anna Constantinescu, Daniel Richter, Sebastian Hild, Nami Saito, Robert Kaderka, Peter Steidl, Jens Woelfelschneider, Jan Trautmann, and Romain Brevet. I also thank Thomas Friedrich, Michael Scholz, Till Detmerring, and Rebecca Grün, whose helpful conversations on radiobiology gave me an introduction to that field. Overall, I thank all of my colleagues at GSI for including me in the cutting edge aspects of their scientific work and for including me in their personal lives outside of work in social and sporting events that I will cherish for my entire life.

I am grateful for the support and mentorship given to me by Rebecca Howell. She is a dedicated teacher and scientist who cares deeply about the successes of her students. Also, I thank my classmates Kenneth Homann, Laura Rechner, and Annelise Giebeler for daily scientific discussions and debate that has sharpened my thinking and helped me through the challenge of completing a doctoral degree.

Table of Contents

List of Tables

List of Figures

Abstract

Although frequently cured of Hodgkin lymphoma, adolescents and young adults can develop radiation induced second cancers. These patients could potentially benefit from scanned ion radiotherapy yet likely would require motion mitigation strategies. In theory, four-dimensional (4D) optimization of ion beam fields for individual motion states of respiration can enable superior sparing of healthy tissue near moving targets, compared to other motion mitigation strategies. Furthermore, carbon-ion therapy can sometimes provide greater relative biological effectiveness (RBE) for cell sterilization in a target but nearly equivalent RBE in tissue upstream of the target, compared to proton therapy. Thus, we expected that for some patients with Hodgkin lymphoma, carbon-ion therapy would reduce the predicted risk of second cancer incidence in the breast compared with proton therapy.

The purpose of this work was to determine whether 4D-optimized carbon-ion therapy would significantly reduce the predicted risk of radiation induced second cancers in the breast for female Hodgkin lymphoma patients while preserving tumor control compared with proton therapy. To achieve our goals, we first investigated whether 4D-optimized carbon beam tracking could reduce dose to volumes outside a moving target compared with 3D-optimized carbon beam tracking while preserving target dose coverage. To understand the reliability of scanned carbon beam tracking, we studied the robustness of dose distributions in thoracic targets to uncertainties in patient motion. Finally, we investigated whether using carbon-ion therapy instead of proton therapy would significantly reduce the predicted risk of second cancer in the breast for a sample of Hodgkin lymphoma patients.

We found that 4D-optimized ion beam tracking therapy can reduce the maximum dose to critical structures near a moving target by as much as 53%, compared to 3D-optimized ion beam tracking therapy. We validated these findings experimentally using a scanned carbon ion synchrotron and a motion phantom. We found scanned carbon beam tracking to be sensitive to a number of motion uncertainties, most notably phase delays in tracking, systematic spatial errors, and interfractional motion changes. Our findings indicate that a lower risk of second cancer in the breast might be expected for some Hodgkin lymphoma patients using carbon-ion therapy instead of proton therapy. For our reference scenario, we found the ratio of risk to be 0.77 ± 0.35 for radiogenic breast cancer after carbon-ion therapy versus proton therapy. Our findings were dependent on the RBE values for tumor induction and the radiosensitivity of breast tissue, as well as the physical dose distribution.

Chapter 1

Introduction

1.1 Goal of Radiotherapy

Since the discovery of radioactivity and x-rays in the late 1890s, scientists and medical doctors have worked together to harness the energy of ionizing radiation to diagnose and treat patients. For many patients, radiotherapy offers a localized or regionalized, minimally invasive treatment option, which can sterilize diseased cells. Radiotherapy is routinely used today to treat cancer patients, and roughly 50% of all cancer patients will receive radiotherapy during some phase of their treatment, which may also include surgery, chemotherapy, and other treatment. In particular, radiation may be beneficial when surgical resection of the diseased tissue is not possible, for example, due to the presence of critical structures near the tumors, the inability of the patient to undergo anesthesia, or due to undesired functional or cosmetic side effects of surgery.

Whereas surgery can, in principle, remove the entire tumor and with it every single cell of cancer from the patient, radiotherapy, as a primary treatment, functions more on the basis of stochastic probability, that is, a certain dose of radiation will sterilize cancer cells in the radiation field with a given probability. Even when treatment is delivered "perfectly" and the radiation strikes every cell of cancer in the patient, a non-zero probability will always exist that a cancer cell survives the irradiation and can possibly seed another tumor. Increasing the dose of radiation reduces this probability for most cancers but increases the damage to healthy tissues in or near the radiation field. Fortunately, cancer cells are often more susceptible to radiation damage than healthy tissue cells, and thus a prescribed radiation dose can deliver both lethal damage to the cancer cells and sublethal damage to healthy tissue, which can often be repaired by the healthy cells. Unfortunately, side effects of radiation therapy can be devastating, including radiogenic second cancer, cardiac toxicity, lung fibrosis, esophageal fibrosis, tissue necrosis, skin desquamation, and loss of

fertility, among others (Marks *et al.*, 2010). For these reasons, radiation doses are kept as low as possible, and the main research problem posed to scientists in radiation oncology during the last century has been: *How do we sterilize the most cancer cells and preserve the most healthy tissue for these patients?*

1.2   Physical Principles of Ion Radiotherapy

Particle Selection

Most radiation treatments are currently delivered by external beam photon radiation, for example, 6 MV x-ray beams, but other radiation fields are also used clinically, such as electrons, neutrons, protons, and carbon ions. *Ion* radiotherapy using protons or carbon ions offers theoretical advantages for many patients compared with photon therapy but presently requires an immense financial investment, that is, hundreds of millions of dollars, to build and maintain the treatment facility. Nonetheless, there is increasing construction worldwide of new proton facilities and, to a lesser degree, new carbon ion facilities. To illustrate the theoretical benefit of ion therapy, a comparison of physical dose distributions as a function of depth in water for various radiation beams is shown in Figure 1.1. To further illustrate the physical differences between photon therapy and ion therapy, treatment plans are shown for a spherical target in water in Figure 1.2 for 18 MV photon beams and 200 MeV passively scattered proton beams.

Due to the physical energy loss characteristics of charged particles stopping in matter, ion beams are particularly promising for treating deep tumors while sparing large volumes of normal tissue both upstream and downstream of the tumor. The two physical phenomena that most influence the shape of the dose distribution in ion radiotherapy are inelastic collisions with atomic electrons and elastic scattering with atomic nuclei, both governed by the electromagnetic force.

Energy Loss of Ions via Inelastic Collisions

Uncharged radiations, *e.g.*, photons and neutrons, mainly pass unperturbed through free space in matter, occasionally colliding with nuclei or orbital electrons. In contrast, charged particles, like protons or carbon ions, quasi-continuously lose energy via inelastic Coulomb collisions with atomic electrons in matter, leaving a wake of ionized and excited atoms in their path.

The energy loss of ion projectiles per unit pathlength in an absorber $(-dE/dx)$ is
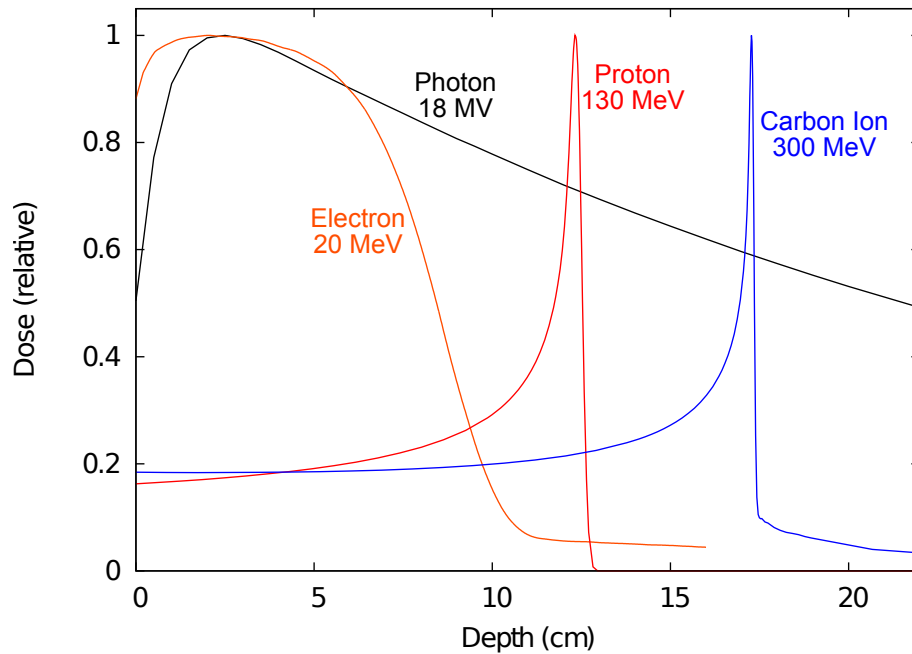
Figure 1.1: Absorbed dose distributions as a function of depth in water shown for various clinical radiation beams. The 18 MV photon dose distribution (black curve) exhibits an initial rise in dose at shallow depths, as the photons produce cascades of secondary electrons, followed by an exponential attenuation of dose at increasing depth as the primary photons are removed from the beam. The 20 MeV electron beam (orange curve) provides a fairly flat high dose region at shallow depths that falls off as electrons reach the end of their range. An exit dose "tail" is seen on the electron distribution due to the production of secondary *Bremsstrahlung* photons. Both 130 MeV proton (red curve) and 300 MeV carbon ion (blue curve) beams provide an inverted depth-dose profile that reaches a sharp maximum, termed the "Bragg peak", near the end of the particle range. An exit dose "tail" is also seen on the carbon ion distribution due to fragmentation of the carbon projectiles, which results in lower-z fragment projectiles having a longer range in water. The depth-dose profile seen for the proton and carbon ion beams may be utilized to treat deeper targets while sparing healthy tissue both upstream of the target and downstream of the target.
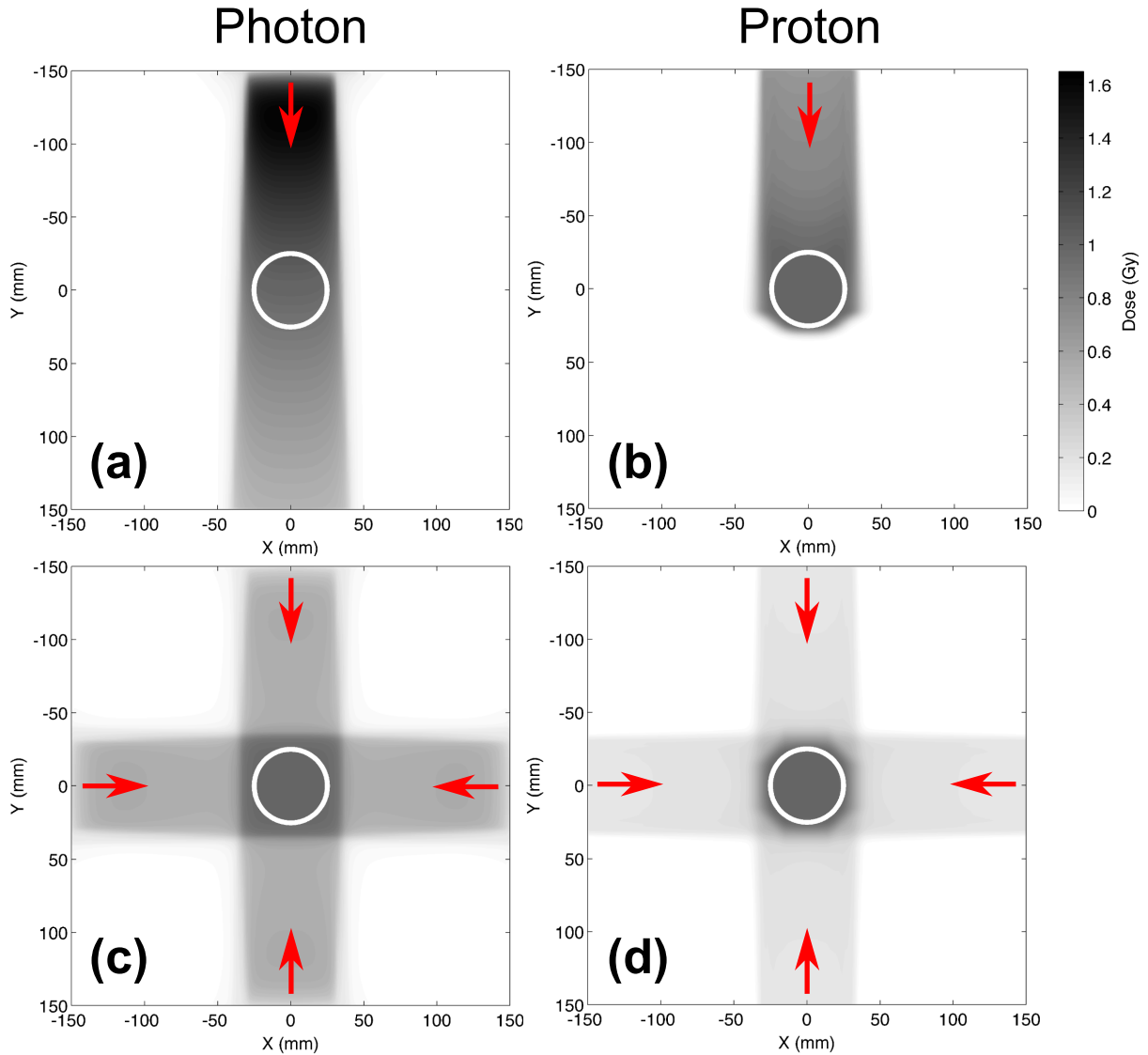
Figure 1.2: Comparison of dose distributions for 18 MV photon (left) and 200 MeV proton (right) radiotherapy for a 5-cm spherical target in water (depth of 150 mm). All plans were normalized to provide 1 Gy to the center of the target (white circle) using: (a) a single photon field, (b) a single proton field, (c) 4 photon fields, and (d) 4 proton fields. Beam directions are indicated by red arrows. For the single field plans (a and b), the proton field deposits much less dose in the volumes both upstream of the target and downstream of the target, compared with the photon field. Increasing the number of beam angles to 4 (c and d) can reduce the dose magnitude to volumes outside of the target but increases the total volume exposed to radiation.

described theoretically by the Bethe-Bloch Equation (Leo, 1994), which is valid for relativistic particle velocities greater than approximately one-tenth of the speed of light, such as are commonly used in radiotherapy,

$$-\frac{dE}{dx} = 2\pi N_a r_e^2 m_e c^2 \rho \frac{Z}{A} \frac{z^2}{\beta^2} \left[\ln\left(\frac{2m_e c^2 \gamma^2 \beta^2 W_{\max}}{I^2}\right) - 2\beta^2 - \delta - 2\frac{C}{Z} \right], \qquad (1.1)$$

where N_a is Avogadro's number, r_e is the classical electron radius, $m_e c^2$ is the rest mass energy of an electron, ρ is the mass density of an absorber, Z is the atomic number of the absorber, A is the atomic mass of the absorber, z is the charge of the ion projectile, β is the velocity of the projectile, as a fraction of the speed of light in vacuum, γ is the Lorentz factor, $W_{\max}$ is the maximum energy transfer by a head-on collision with a single electron, I is the mean excitation potential of the absorber, δ is a "density correction" factor to account for polarization of the absorber by the projectile, and C is a "shell correction" factor to account for the influence of dynamic electron fields near the projectile, which is more important at lower velocities.

The inverse relation between energy loss and the projectile velocity ($-dE/dx \propto 1/\beta^2$) explains the inverted depth dose profile and the characteristic "Bragg peak" as the projectile slows down and stops in matter, seen for the proton beam and carbon ion beam in Figure 1.1. Conceptually, slower ions have more *time* to perturb the local orbital electrons in the absorber whereas faster ions pass through the local environment quickly, with less time to exert force on local orbital electrons.

Elastic Scattering of Ions

Whereas inelastic collisions with orbital electrons are the main mechanism of energy loss and most responsible for the shape of the depth dose distribution for ion beams along the depth axis, *elastic scattering* with atomic nuclei is most responsible for the shape of the off-axis or lateral dose distribution. The degree of elastic scattering is fundamentally described by Rutherford scattering, *i.e.*, the charged projectile is deflected as it passes through the electric field of a positively charged nucleus in the absorber. The differential scattering cross section ($d\sigma$) for a projectile scattering into a given solid angle ($d\Omega$) about an angle (θ) from its initial trajectory is given by (Leo, 1994)

$$\frac{d\sigma}{d\Omega} = z^2 Z^2 r_e^2 \frac{(m_e c/\beta p)^2}{4 sin^4(\theta/2)} \qquad (1.2)$$

The degree of scattering is seen here to be directly proportional to the square of the projectile charge z^2 and inversely proportional to the square of the projectile velocity β^2 and momentum p^2. The many individual Rutherford scattering events that influence a single projectile path can be described by multiple Coulomb scattering theory, which predicts the lateral and angular probability distributions of a particle beam that undergoes many elastic scattering events after traversing a given thickness of matter (Rossi and Greisen, 1941). Ultimately, these theories can be used to predict the shape of dose distributions from ion beams in patients, an important requirement for radiotherapy treatment planning.

One important principle regarding elastic scattering for radiotherapy is that higher z particles typically require higher velocity than lighter particles to achieve the same range in matter and, despite their higher charge, are less influenced by elastic Coulomb scattering due to their higher momentum. Thus, for heavier ions, *e.g.*, carbon ions *versus* protons, it is usually possible to deliver a beam with sharper definition at depth in the patient. Weber and Kraft (2009) reported that carbon dose gradients in the lateral beam penumbra can be approximately 3 times sharper than those of protons, which can reduce dose to healthy tissues near the target. This is especially important when critical structures are very near the lateral edge of a target boundary and is a major impetus to use carbon ions instead of protons or electrons.

Beam Delivery Systems for Ion Therapy

In order to deliver a therapeutic beam that is useful for patients with a wide range of tumor sizes, a system must be implemented to spread the Bragg peak to cover the three-dimensional (3D) extent of the tumor. The two most common delivery systems for ion therapy are passive scattering and active scanning, illustrated in Figure 1.3. Both of these systems are capable of spreading the Bragg peak over a 3D tumor volume. The passively scattered system has the advantage that the beam is delivered to the entire treatment volume almost instantaneously but the disadvantages that the dose distribution is generally not conformal to both the proximal and distal surfaces of the target. Furthermore, heterogeneities in the patient may introduce dose heterogeneity in the passively scattered ion dose distribution due to lateral scatter disequilibrium. The actively scanned system potentially improves the conformity and uniformity of dose to a target but has a high sensitivity to uncertainties in patient setup and motion, since the individual ion scan paths can potentially overlap or miss regions of the target when the patient is misaligned or moves during treatment.
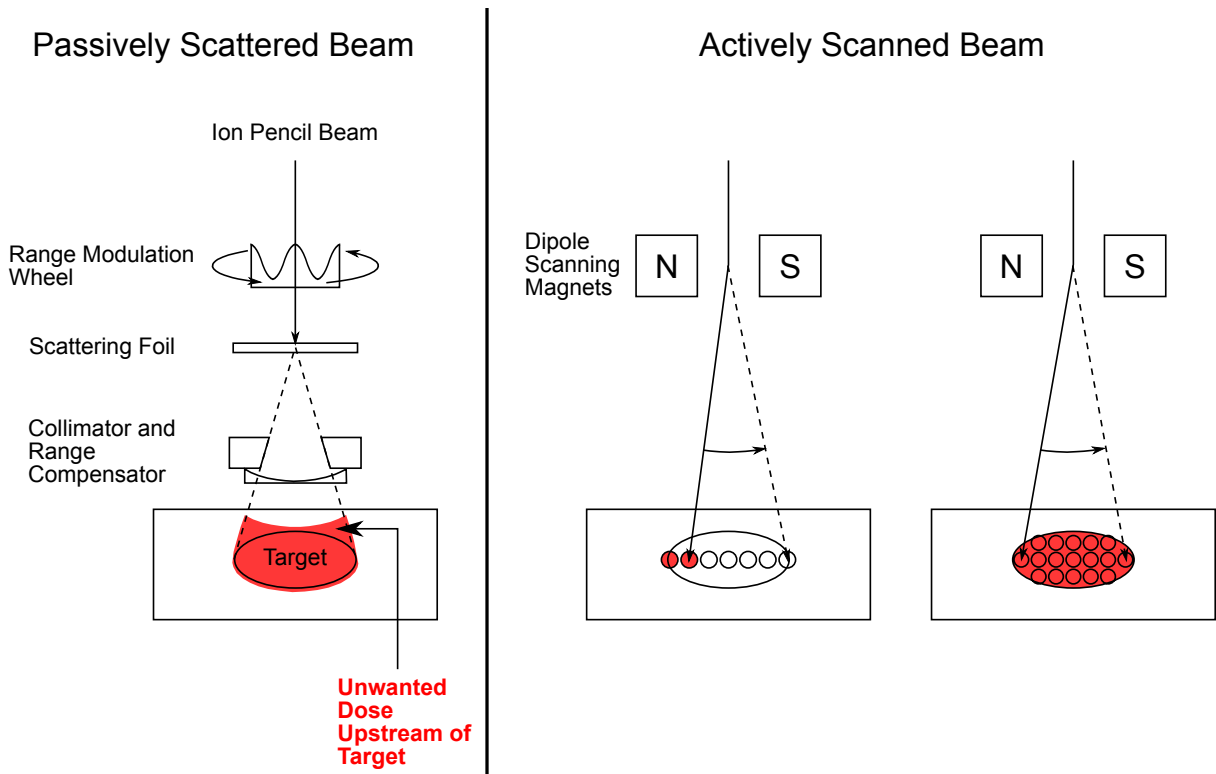
Figure 1.3: Comparison of passively scattered ion beam delivery system *versus* an actively scanned ion beam delivery system. Initially, a narrow diameter (few mm) ion beam is produced by a particle accelerator, *e.g.*, synchrotron or cyclotron. In order to produce a useful therapeutic beam, the narrow beam and sharp Bragg peak must be spread to cover the lateral extent and depth variation of a 3D target volume in a patient. The *passively scattered* system (left) uses a range-modulation wheel, *e.g.*, a spinning disk of acrylic with variable thickness, to quickly scan the ion beam over the depth-thickness of the target, producing a spread-out Bragg peak. A scattering foil is used to spread the pencil beam into a broad field, which is then collimated to match the lateral boundary of the target. A range compensator modulates the range of the broad ion beam to match the off-axis distal depth of the target surface, providing a target dose (red region) that is conformal to the distal target surface but not conformal to the proximal target surface, giving unwanted dose upstream of the target. In contrast, an *actively scanned* beam delivery system (right) uses magnetic deflection to scan the ion pencil beam across the lateral extent of the target. The beam typically stops at prescribed spots (small circles) throughout the target and delivers a prescribed number of ions. After a single iso-energy layer is finished, the energy of the pencil beam is actively changed, *e.g.*, by resetting the acceleration scheme, and all other iso-energy layers are delivered to provide dose to all depths of the target (see filled small red circles at right). The advantages of an actively scanned delivery system include the ability to conform dose to both the deep and shallow surfaces of the target and the ability to optimize the particle numbers for each spot throughout the target, which can improve target dose homogeneity when the target lies in heterogeneous tissue or be used for intensity-modulated particle therapy.

1.3 Biological Effects of Ion Beam Radiation

RBE

Although the physical interactions of radiation beams in matter are fairly well understood, the biological effects of radiation are not entirely understood at a mechanistic level and, generally, are less understood for ion therapy than for photon therapy. However, what is clearly known is that there can be a different biological effect for the same physical dose given by different types of radiation and different ion species (Hall and Giaccia, 2006). To allow intercomparison of the biological effectiveness of various radiation types, a common standard has been defined, the relative biological effectiveness (RBE), which is defined as the ratio of doses between a reference radiation $D_{\text{reference}}$ and a test radiation D_{test} under the condition that both doses produce an identical biological endpoint on the system studied, expressed as

$$\text{RBE} = \frac{D_{\text{reference}}}{D_{\text{test}}}. \tag{1.3}$$

The reference radiation is typically 250 kVp x-rays. Ultimately, the RBE depends on many factors including the test radiation field and particle type(s), the energy spectrum of the radiation field, the dose magnitude, the dose rate, the tissue type and cell type, the exact biological endpoint studied, the oxygenation status of cells, the phase of cells in their division cycle, the presence or deficiency of DNA damage repair proteins, and a continuing list of beam specific and subject specific variables. Thus, the most useful RBE values are those that are experimentally determined under very similar, if not identical, conditions for a given irradiation where one wishes to know an expected RBE.

RBE *versus* LET

RBE is known to depend on the linear energy transfer (LET) of charged particles. LET quantifies the kinetic energy lost by a charged particle traveling through matter per unit distance. The LET of charged particles is directly related to the inelastic collision cross section described above and, thus, is also dependent on the charge and velocity of ions passing through matter. Examples of ion RBE as a function of LET from the literature are shown in Figure 1.4. For a given ion species, RBE typically increases with LET up to a certain peak value. The peak RBE *versus* LET is reached when the average distance between ionization events roughly coincides with the 2 nm diameter of the DNA double helix (Hall and Giaccia, 2006). At LET values higher than that of the peak RBE, the "overkill" phenomena is observed where RBE decreases with further increasing LET. This
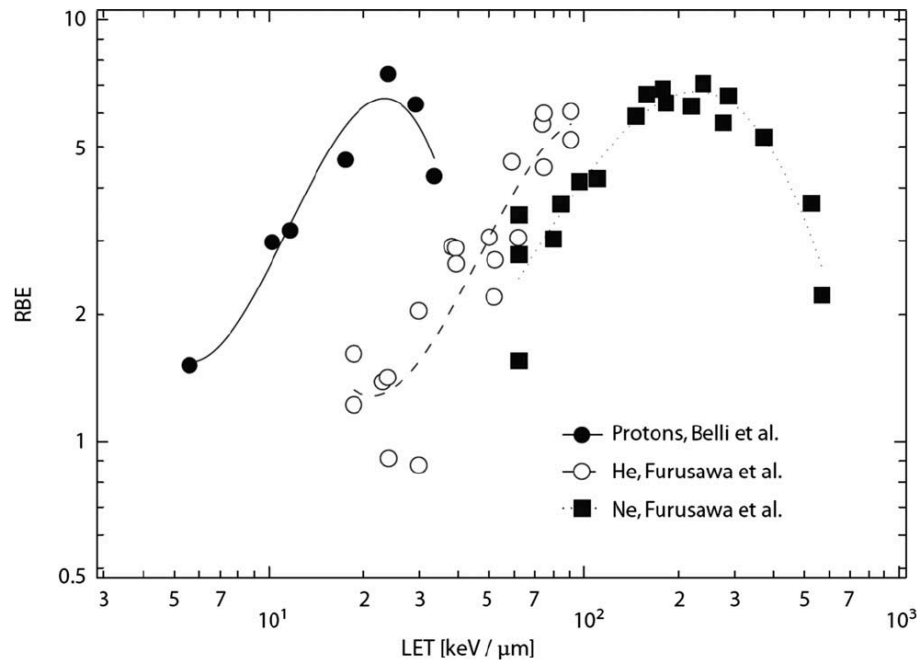
Figure 1.4: Example of RBE dependence on ion LET and particle species for proton, helium, and neon irradiation in cell sterilization experiments. Note that RBE generally increases with LET until reaching a peak RBE, at an LET value depending on the ion species. After this peak RBE, a further increase in LET leads to a decrease in RBE, *i.e.*, the "overkill effect." Figure reproduced with permission from Schardt *et al.* (2010). Data from Scholz (2003).

can be understood considering that the absolute number of ions needed to deliver a fixed macroscopic dose decreases with increasing LET. When the number of ions decreases low enough, the hitting probability drops significantly. The effectiveness of a single ion track is very high, but the probability that the ion tracks hit the cell nuclei decreases at very low particle fluence (Schardt *et al.*, 2010).

The increase of RBE with increasing LET can be better understood by looking at the distribution of ionization and secondary electrons produced near the projectile track. Figure 1.5 shows the distribution of secondary electron tracks produced by proton and carbon ion tracks in water. The high density of secondary electrons near the tracks of carbon ions leads to the higher RBE seen for carbon. If the ion tracks cross the DNA, the high density of secondary electrons can cause highly clustered DNA damage that is harder for the cell to repair than the more diffused damage produced by low LET particles, such as protons or photons.

An important rationale for choosing an nucleus like carbon, out of all possible elements, is that carbon ions have both a high LET at low energies, such as found near the Bragg peak, and a low LET at higher energies such as in the beam entrance channel. Therefore, carbon ions used for cancer therapy can provide a favorable combination of high RBE in diseased tissues near the Bragg peak and a relatively low RBE in normal tissues that lie upstream of the Bragg peak, *e.g.*, closer to the patient skin surface. This relation was recently studied in cell survival experiments by Elsässer *et al.* (2010), shown in Figure 1.6. Their results suggest that carbon ion therapy might be expected to provide an equivalent tumor control, with reduced damage to tissues in the beam entrance channel, compared to proton therapy.

Calculation of Ion Beam RBE for Radiotherapy Planning

For ion radiotherapy, a method to calculate RBE at different locations in the patient is essential due to the changing energy spectrum of the particle beam with depth in the patient. The ion therapy project at Lawrence Berkeley Laboratory (LBL) (Berkeley, California, USA) performed extensive cell survival experiments with passively scattered heavy ion beams using helium, carbon, neon, and argon Lyman and Howard (1977); Chapman (1977); Chapman *et al.* (1978). Based on those cell sterilization data, passive scattering filters were designed to produce a spread-out Bragg peak with decreasing physical dose near the deeper region of the target which could achieve uniform biological response, *i.e.*, cell sterilization, throughout the target. Similar to that approach, the clinical carbon ion therapy project at National Institute of Radiological Sciences (NIRS) (Chiba, Japan) used
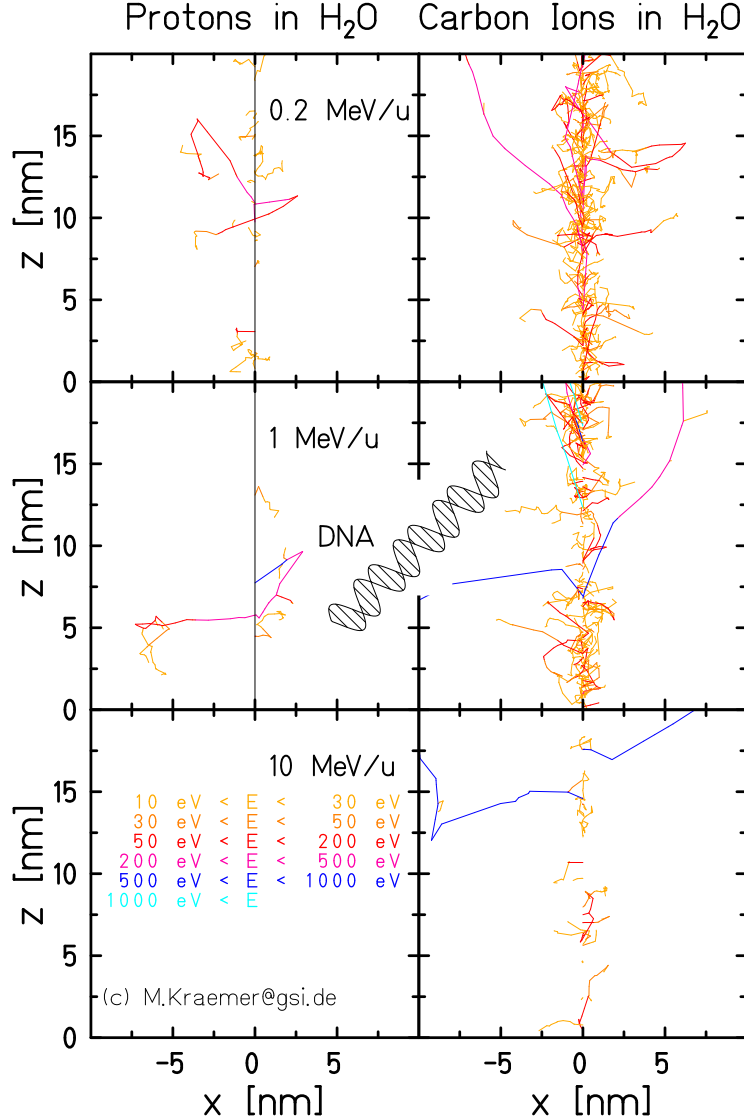
Figure 1.5: Distribution of secondary electron tracks produced by proton and carbon ion tracks in water. A single carbon ion track produces many more secondary electrons than a single proton track, due to the higher charge (+6) of the carbon ion. The few nanometer range of secondary electrons roughly coincides with the diameter of the DNA double helix (see inset diagram), which means that a single traversal of a carbon ion across the DNA can lead to highly localized, complex damage to the DNA. For an equivalent macroscopic dose, many more protons are needed than carbon ions, which produces a more diffused damage to the DNA for protons compared with carbon ions. The diffused damage is easier for many cells to repair than the clustered damage seen with carbon ions, which explains the higher RBE of carbon ions compared to protons, especially at low energies (≤ 1 MeV) found near the Bragg peak. Figure reproduced from Lüchtenborg (2011).
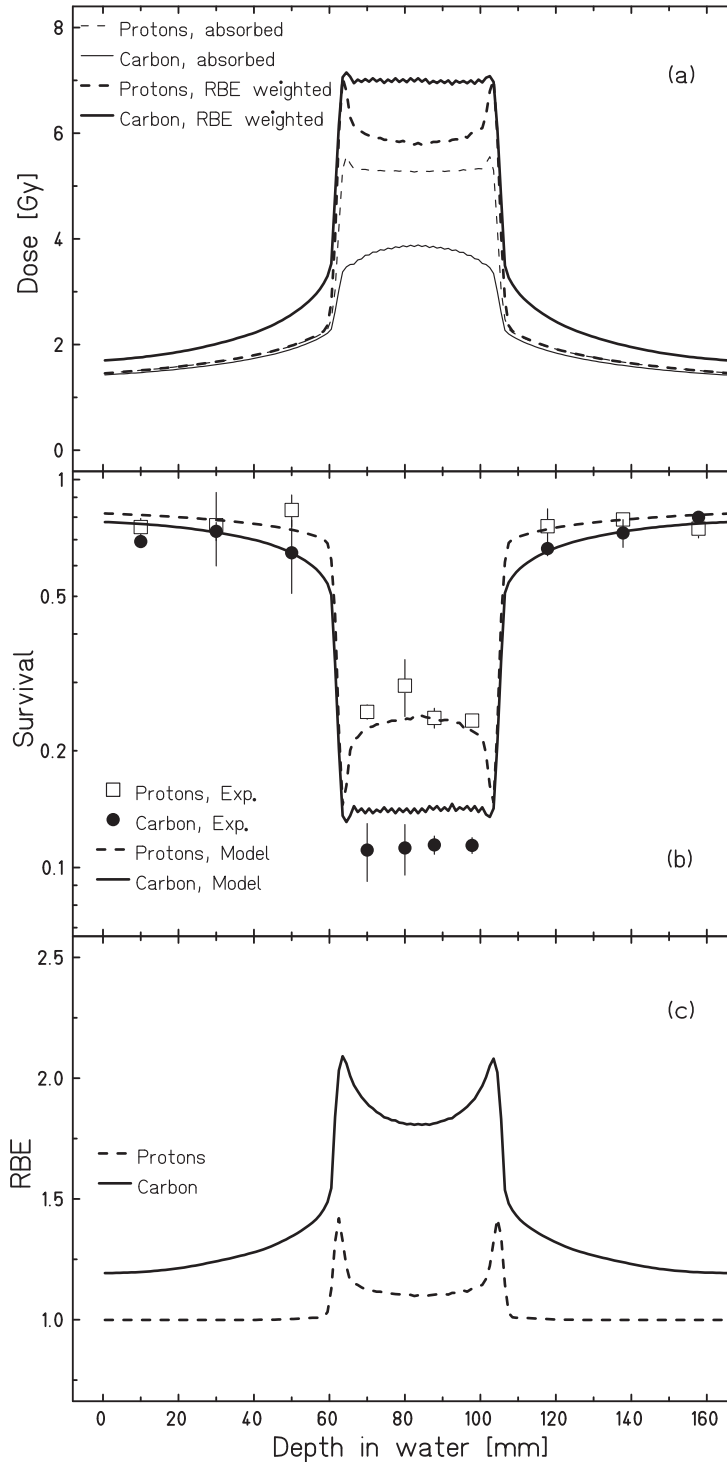
Figure 1.6: RBE-weighted dose, cell survival, and predicted RBE for proton and carbon ion irradiation of Chinese hamster ovary cells. When the cell survival was nearly identical near the phantom surface, carbon-ion therapy is seen to provide a lower predicted and measured cell survival in the spread-out Bragg peak region (at 60-100 mm depth). Curves show the predictions of the Local Effect Model (Scholz *et al.*, 1997; Friedrich *et al.*, 2012) for RBE-weighted dose, cell survival, and RBE. Data points represent experimental cell survival measurements. Figure reproduced with permission from Elsässer *et al.* (2010).

cell survival measurements from human salivary gland tumor cells to design their spread-out Bragg peak for uniform biological effect and established an *in-vitro* link to their clinical experience with neutron therapy to prescribe patient doses (Kanai *et al.*, 1997, 1999).

For the clinical carbon ion therapy project at GSI Helmholtzzentrum für Schwerionen-forschung (GSI) in Darmstadt, Germany, the "Local Effect Model" (LEM) was developed to predict ion RBE and enable biological treatment plan optimization for scanned carbon ion fields with mixed particle types and energy spectra (Scholz *et al.*, 1997; Krämer and Scholz, 2000; Elsässer *et al.*, 2010). A major premise of the LEM approach is that the known biological effectiveness of photons can be used to predict the biological effectiveness of ions on a microscopic dose level. Further, by integrating that microscopic biological damage pattern predicted for ions over the cell nucleus, one can estimate the *macroscopic* RBE, which can be used for treatment planning for cancer therapy.

1.4   Current Challenges for Ion Therapy

Moving Targets

While ion therapy may reduce dose to healthy tissues and thus decrease the potential for severe side effects of radiation therapy, only a few approaches have been used on patients with moving thoracic tumors, such as lung cancer patients, who experience the highest number of deaths each year from cancer in the United States, or Hodgkin lymphoma patients, who respond well to radiotherapy but are vulnerable to radiation side effects. Ion beam therapy requires special consideration for moving tumors, compared to photon therapy, since the motion of heterogeneous tissue can cause large changes in the range of ion beams.

For passive ion beam delivery, beam-specific margins can be used to encompass target motion and account for variation in radiological depth of the target (Bush *et al.*, 2004; Mayahara *et al.*, 2007; Nihei *et al.*, 2005; Slater *et al.*, 1998; Tsuji *et al.*, 2005; Park *et al.*, 2012). To reduce required motion margins, controlled breathing techniques such as breath-hold (Hanley *et al.*, 1999; Wong *et al.*, 1997), jet ventilation (Hof *et al.*, 2003), and even induced apnea (RPTC, 2011), can be used to minimize organ motion. Alternatively, beam gating systems also allow reduced motion margins and are used clinically with passive ion beam delivery at several centers (Hashimoto *et al.*, 2006; Iwata *et al.*, 2008; Koto *et al.*, 2004; Lu *et al.*, 2007; Minohara *et al.*, 2000; Nihei *et al.*, 2006). Bert and Durante (2011) recently reviewed a number of motion strategies for particle therapy used at several institutions worldwide, and report that, while passive ion beam therapy is used to treat
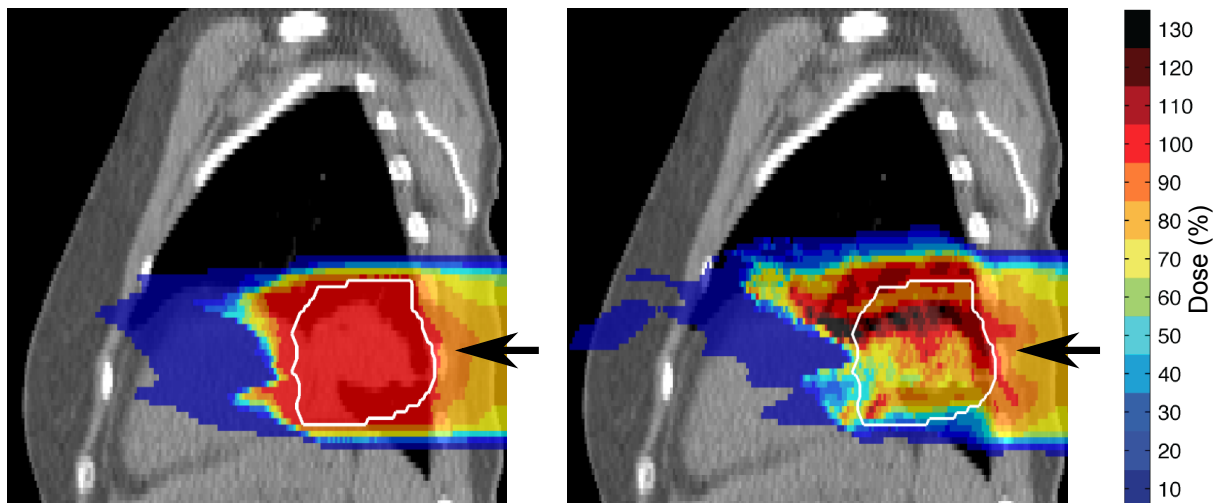
Figure 1.7: Sagittal view of scanned carbon ion treatment plans for a lung target (white contour) with single posterior-to-anterior beam directions (indicated by the black arrows). Static 3D dose calculation (left) shows highly uniform target dose coverage but ignores motion. If the same treatment plan is simulated using 4D dose calculation (right), a severe interplay effect between ion scanning and organ motion is seen, with large regions of overdose occurring outside of the target region and very low underdosage occurring even near the center of the target.

patients with moving tumors, scanned ion therapy is not yet used routinely, except for patients with very small motion.

Given the theoretical dosimetric advantages of using actively scanned ion therapy instead of passively scattered ion therapy, it would appear desirable to use the scanned beam for thoracic tumors. However, it has been cautioned that scanned ion therapy may not provide reliable dose distributions for cancer sites subject to respiratory motion (Newhauser *et al.*, 2009), and, indeed, irradiating a moving tumor with a scanned ion beam without specific countermeasures to address motion has been experimentally shown to cause unacceptable dose coverage of the therapy target, due to *interplay* between target motion and delivery of the scanned ion beam (Lambert *et al.*, 2005; Bert *et al.*, 2008). Figure 1.7 shows 3D and 4D dose distributions calculated for scanned carbon ion therapy of a lung cancer patient and illustrates the dosimetric failure that can occur when no motion mitigation strategy is used. This calculation demonstrates target underdosage due to interplay near the very center of the target, which supports that the interplay problem can not be solved by simple geometric margin expansion of the treatment field.

Motion mitigation studies have been reported that advance the possibility of irradiating a moving tumor with scanned ion therapy (Bert and Durante, 2011). One method, the use of an internal target volume (ITV) that includes beam-specific range uncertainty

14

margins combined with *rescanning* potentially achieves sufficient target coverage (Phillips *et al.*, 1992), relying on averaging effects between successive, randomly heterogeneous dose distributions in the target. However, the motion and range-uncertainty margins required for the ITV include normal tissue and, therefore, degrade conformity of the dose distribution to the cancer target, potentially reducing one of the main advantages of scanned ion therapy. Also, the random dose patterns may not always combine to provide uniform dose with rescanning, which could compromise the tumor control probability. Another method, *gating* the irradiation to a small phase window of the respiratory cycle may allow ideal tumor coverage while maintaining sharp target dose conformity (Minohara *et al.*, 2000). However, smaller gating windows can lead to longer treatment times and reduce the number of patients that can be treated in a given timeframe. Increasing the gating window, *e.g.*, from 10% to 30% of the respiratory cycle, reduces the treatment time but potentially increases required motion margins and increases the chances of interplay effects within the residual motion window. More elaborate techniques to synchronize the accelerator spill sequence with the respiratory gating window have been reported and promise to reduce the treatment time for gating of scanned ion therapy (Tsunashima *et al.*, 2008). Another method, *beam tracking* with scanned ion beams is an approach where individual pencil beams are steered throughout the patient respiratory cycle such that each individual pencil beam Bragg peak position remains in the same local subvolume of the target for the entire respiratory cycle (Grözinger *et al.*, 2004; Bert *et al.*, 2007; Saito *et al.*, 2009). This approach uses magnetic deflection to track lateral target motion and requires a fast, *i.e.*, within several milliseconds, energy modulation system to track changes in radiological depth of the target. This beam tracking system is further discussed in Chapter 2. One or more of these motion mitigation strategies might enable the effective use of scanned ion beams for thoracic cancers in the near future, potentially reducing dose to normal tissue compared with passively scattered ion therapy. However, the optimal solution to this problem is not yet known.

Predicting Risks of Radiogenic Second Cancers after Ion Therapy

Along with the technical complexity of delivering scanned ion therapy to moving thoracic tumors, biological uncertainties make it particularly challenging to estimate risks of long term side effects of ion therapy, such as radiation-induced malignant neoplasms. This is particularly important to understand for young patients and those with long expected survival after radiotherapy. One population that might greatly benefit from scanned ion therapy is Hodgkin lymphoma patients, who are particularly vulnerable to radiation side

effects. Lymphomas constitute the highest proportion, that is, nearly 20%, of all incident primary cancers in adolescents and young adults (Bleyer *et al.*, 2006). Patients diagnosed with early stage HL and treated with combined chemotherapy and radiation can expect survival higher than 90% at 5 years (Armitage, 2010) and 60-80% at 20 years, with survival rates decreasing with age at diagnosis (Bleyer *et al.*, 2006). For this population of patients, side effects of therapy can in some cases be as devastating as the initial HL diagnosis, *e.g.*, second primary cancers, cardiac toxicity, and infertility (Robison *et al.*, 2002). In particular, radiation therapy can induce malignant neoplasms, *i.e.*, second cancers, presumably by initiating genomic instability via direct DNA damage or by promoting carcinogenesis via inflammatory tissue response to radiation (Newhauser and Durante, 2011). In a 25-year study of 32,591 HL patients with 1,111 25-year survivors, Dores *et al.* (2002) reported a 10.5% absolute excess risk of cancer in the female breast for patients treated with radiation, mainly using photon mantle fields. In response to this, research for HL treatment in the past decades has focused on reducing radiation dose to healthy tissue and the overall size of therapy fields.

For some HL patients, scanned carbon ion therapy might reduce physical dose to normal tissues upstream of the target, *e.g.*, breast tissue, compared with scanned proton therapy, due to the variable RBE and LET discussed above. However, estimation of the risks of secondary malignant neoplasms for these patients is not straightforward and likely depends on complex, competing relations between the RBE for HL tumor control, RBE for normal tissue tumor induction, and RBE for normal tissue sterilization, which likely all depend on the radiation particle spectrum and the radiosensitivity of individual tissues. To our knowledge, a study comparing second cancer risk in the breast for HL patients after carbon ion *versus* proton radiotherapy has not been reported in the literature.

1.5   Objective of this Study

Objective

The objective of this work was to develop and investigate a new strategy for treating moving tumors using 4D optimization for scanned ion therapy with beam tracking. We sought to better understand the robustness of scanned ion beam tracking to motion uncertainties. We also sought to demonstrate that using carbon-ion therapy instead of proton therapy might offer the ability to reduce risks of secondary malignant neoplasms in healthy tissue upstream of cancer targets in the thorax.

Hypothesis

We hypothesized that using 4D-optimized carbon-ion therapy would reduce the predicted risk of radiation induced second cancers in the breast for female Hodgkin lymphoma patients while preserving tumor control compared with proton therapy.

Specific Aims

① Determine whether 4D-optimized carbon tracking therapy can reduce dose to volumes outside a moving target while maintaining adequate target dose coverage. We developed a new scanned ion beam tracking approach using 4D optimization. We performed water phantom studies and patient studies using computer simulations to compare dose distributions for moving targets and avoidance volumes for 4D *versus* 3D-optimized carbon tracking. In addition, we demonstrated the feasibility of our 4D-optimized carbon tracking approach in an experiment using a moving phantom and a scanned carbon ion beam.

② Quantify the impact of uncertainties in patient respiratory motion on dose distributions in moving targets for scanned carbon ion beam tracking. We simulated dose for scanned carbon ion beam tracking using mathematical phantoms and lung cancer patient 4D computed tomograms (4DCTs). We tested the sensitivity of dose distributions in the target to various systematic and random errors that are characteristic for lung motion and for the scanned carbon tracking system at GSI. We also investigated the effects of interfractional changes in organ motion on target dose coverage for the lung cancer patients by simulating treatment on multi-week 4DCTs.

③ Determine whether using carbon-ion therapy instead of proton therapy reduces the predicted risk of second cancer incidence in the breast for a sample of Hodgkin lymphoma patients. We simulated scanned proton and scanned carbon ion treatment for 6 HL patients using a research treatment planning system for ion radiotherapy. We calculated relative predicted risks of second cancer in the breast using a linear-non-threshold tumor induction model and a linear-quadratic breast cell inactivation model. In addition, we explicitly modeled RBE for the ion fields for both breast tumor induction and cell inactivation.

Rationale

The optimal approach for using scanned ions to treat thoracic targets is not yet known. We expected that a delivery system that utilized 4D-optimized beam tracking would provide improved sparing of healthy tissue near a moving target, while achieving equivalent tumor control, when compared to an existing approach using 3D-optimized beam tracking. Further, we expected that using carbon-ion therapy instead of proton therapy would further reduce dose to normal tissue upstream of the target and might reduce the risk of treatment side effects for patients with thoracic tumors, due to the variable RBE of carbon beams stopping in tissue.

To test these working hypotheses, we chose to study lung patients as a test case for 4D-optimized beam tracking, since lung tumors can exhibit large motion and dramatic changes in radiological depth of the tumor, a particularly challenging case for scanned ion beam tracking. To evaluate the potential of carbon to reduce risks of late effects compared to protons, we studied HL patients, a test population with a long life expectancy after therapy and at high risk to develop long term side effects of radiotherapy, including radiogenic second cancers.

Chapter 2

4D Optimization for Scanned Ion Beam Tracking Therapy of Moving Targets

2.1 Introduction

In order to treat patients with moving thoracic tumors using scanned ion beams, motion mitigation strategies are needed to ensure uniform dose coverage of the moving target and to best minimize dose to normal tissues near the moving target. *Beam tracking* is one of the more technically challenging motion mitigation strategies to implement for scanned ion beams but potentially provides a highly conformal dose to moving targets. In this approach, individual ion beams are steered throughout the patient respiratory cycle such that each individual ion-beam Bragg-peak position remains in the same local subvolume of the target for the entire respiratory cycle. A 4D treatment control system for scanned ion beam tracking has been implemented for experimental studies at the GSI Helmholtz Centre for Heavy Ion Research (GSI) in Darmstadt, Germany (cf. Figure 2.1) (Grözinger *et al.*, 2004). In this system, ion beams can be delivered in any phase of respiration since the ion beams track all positions of the tumor for the entire respiratory cycle. In addition, dosimetric target margins for scanned ion beam tracking theoretically remain as sharp and conformal as that possible for a non-moving cancer site.

For treatment planning of scanned ion beam tracking (Bert and Rietzel, 2007), particle numbers for each pencil beam are first optimized to provide target dose coverage for a single respiratory motion state, *e.g.*, at end-exhale, and, then, required tracking offsets for each pencil beam are computed for all other motion states of respiration. Tracking offsets are calculated using both 4DCT image data and deformable image registration vectors, which register anatomic motion through the discrete temporal states of respiration, represented by the 4DCT. Lateral-tracking offsets are calculated by projecting the deformable image registration vectors onto a plane perpendicular to the beam axis. Range-tracking offsets
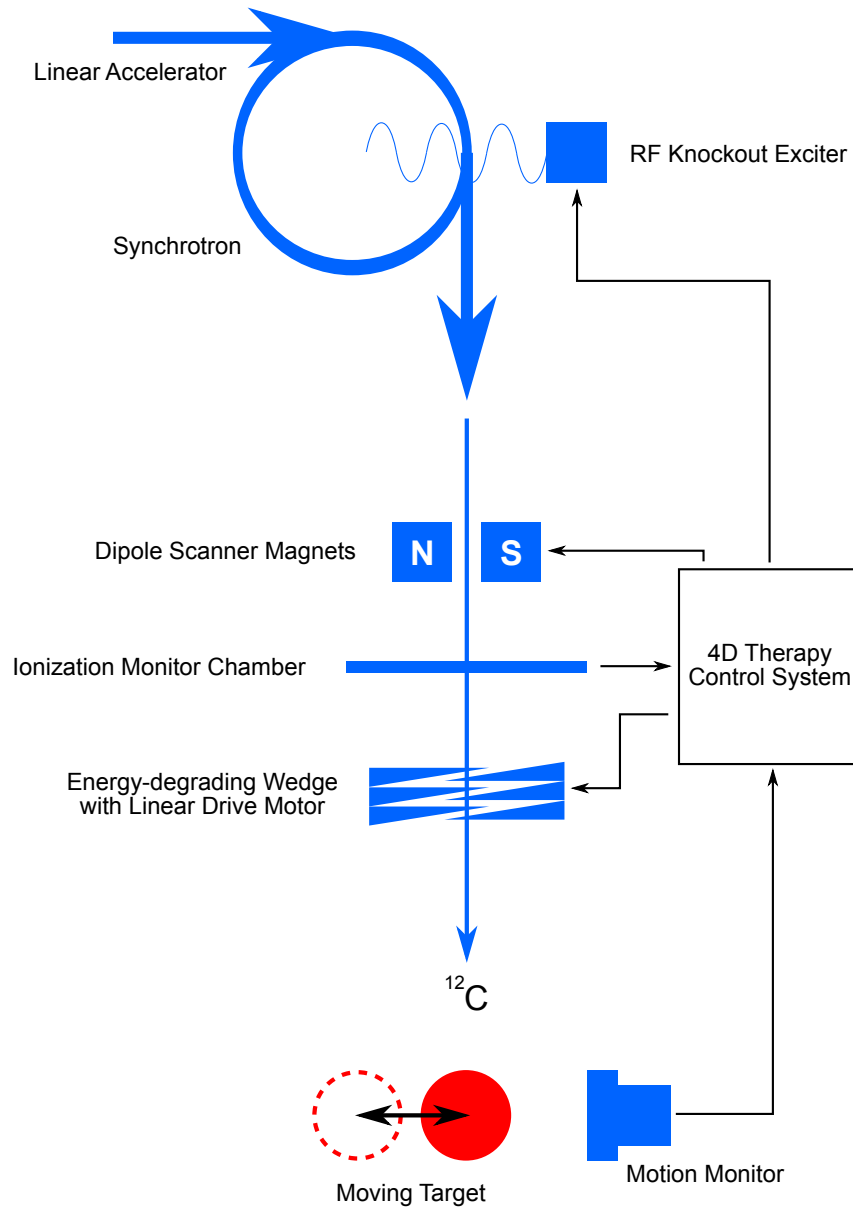
Figure 2.1: Beam tracking system for scanned ion therapy implemented at GSI. The ion beam is produced by linear and synchrotron acceleration and extracted by a radiofrequency (RF) knockout exciter. Dipole scanner magnets steer the ion pencil beams laterally to achieve target coverage and to track target motion. A system of acrylic wedges mounted on linear drive motors modifies the range of individual pencil beams to track changes in radiological depth of the target (Saito *et al.*, 2009). A motion monitoring system provides feedback to the 4D therapy control system, which transmits precomputed beam tracking offsets for each pencil beam and each motion state to the scanner magnets and wedge system, so that each pencil beam follows the target motion.

require a more complex calculation using both the deformable image registration vectors and a recalculation of the radiological depth of the target for each motion state. This beam tracking approach of Bert and Rietzel (2007) can achieve adequate target dose coverage for some patients but does not provide a solution for patients with tumors that deform or rotate significantly during respiration. To address this problem, Lüchtenborg *et al.* (2011) recently developed a real-time dose compensation method for beam tracking that improves target dose coverage for scanned ion beam tracking by adapting particle numbers in real-time based on the motion status of the target during the delivery of each pencil beam. We wish to emphasize that each of these beam-tracking approaches are novel and have not yet been applied to patient treatment. The ideal method to apply scanned ion beam tracking therapy to patients is not yet known. Based on the approach of Lüchtenborg *et al.* (2011), we were inspired to investigate 4D optimization as a strategy to further improve target dose coverage and potentially control dose to healthy tissue for scanned ion beam tracking. Whereas many motion mitigation strategies attempt to eliminate or reduce the impact of time and motion as factors in therapy, we sought to *exploit* time and motion as potential advantages in therapy using 4D optimization.

Several studies have reported 4D optimization strategies for *photon* therapy. Zhang *et al.* (2004) incorporated respiratory motion data into optimization of photon tomotherapy plans and demonstrated improved target dose conformity. Trofimov *et al.* (2005) developed four new approaches to optimize intensity-modulated photon fields for lung and liver patients with moving tumors. Nohadani *et al.* (2010) reported another 4D optimization approach for photon therapy that improved dose coverage compared to beam gating for lung cancer patients and reduced dose to healthy lung and was also more robust to irregular breathing than beam gating. Chin and Otto (2011) further demonstrated in phantom studies that 4D optimization can be applied to volumetric modulated arc therapy to spare avoidance volumes near a moving target. These studies suggest that the added degree of freedom, *i.e.*, time, in optimization can be used to improve target dose coverage and to spare avoidance volumes near a moving target. However, to our knowledge, 4D optimization for *ion* therapy has not been previously reported in the literature.

The purpose of our study was to develop and test a new beam tracking approach using 4D optimization for scanned ion therapy of moving tumors. We tested the working hypothesis that 4D-optimized scanned ion beam tracking can reduce dose to avoidance volumes outside a moving target compared with 3D-optimized scanned carbon beam tracking while maintaining adequate target dose coverage. The following section begins with a description of our implementation of a 4D-optimization algorithm in a treatment planning system for scanned ion therapy. Then, we describe two treatment-planning studies, one for a water

phantom and another for a lung cancer patient, in which we compared our 4D-optimized beam-tracking approach against an existing 3D-optimized beam-tracking approach. Finally, we discuss a simple experiment using moving films and a scanned carbon ion beam-tracking system that provides preliminary evidence that our approach is technically feasible.

2.2 Methods

2.2.1 4D Optimization

In this work, we designed a 4D-optimization approach for scanned ion beam tracking therapy. Our approach involves planning of a *4D field* composed of ion pencil beams, each with a unique geometric position, energy, and particle number (*i.e.*, number of particles incident on the patient in that pencil beam), determined for individual motion states. To illustrate our theoretical concept, a diagram comparing 4D-optimized scanned ion beam tracking *versus* an existing 3D-optimized scanned ion beam tracking method is shown in Figure 2.2. By optimizing the particle numbers for each pencil beam for each motion state, we sought to calculate 4D fields that could accumulate a uniform dose to a moving target, but, possibly, reduce dose to avoidance volumes near the moving target, compared with a 3D-optimized beam tracking approach.

We implemented our approach in the TRiP4D research treatment planning system (TPS) code for scanned ion therapy (Krämer *et al.*, 2000; Bert and Rietzel, 2007; Richter *et al.*, 2013) using the C programming language. We used much of the existing TPS code, which could already calculate 4D dose distributions and plan beam-tracking offsets. In addition, we substantially extended the optimization routines to incorporate 4DCT data, deformable image registration vectors, and beam tracking offsets that were necessary to enable optimization of a 4D field.

Our treatment planning workflow for 4D-optimized scanned ion beam tracking included a sequence of the following steps.

(1) A 3D scanned ion field was planned to cover a 3D representation of the 4D clinical target volume (CTV) in a reference motion state, with Bragg peaks for each pencil beam evenly spaced throughout the target volume. This step required a 3D computed tomogram (CT) extracted from a 4DCT, *i.e.*, representing the patient in the reference state, and CTV contours to determine the necessary energies and lateral coordinates of ion pencil beams.

(2) Particle numbers were optimized for the 3D scanned ion field to provide uniform dose

22
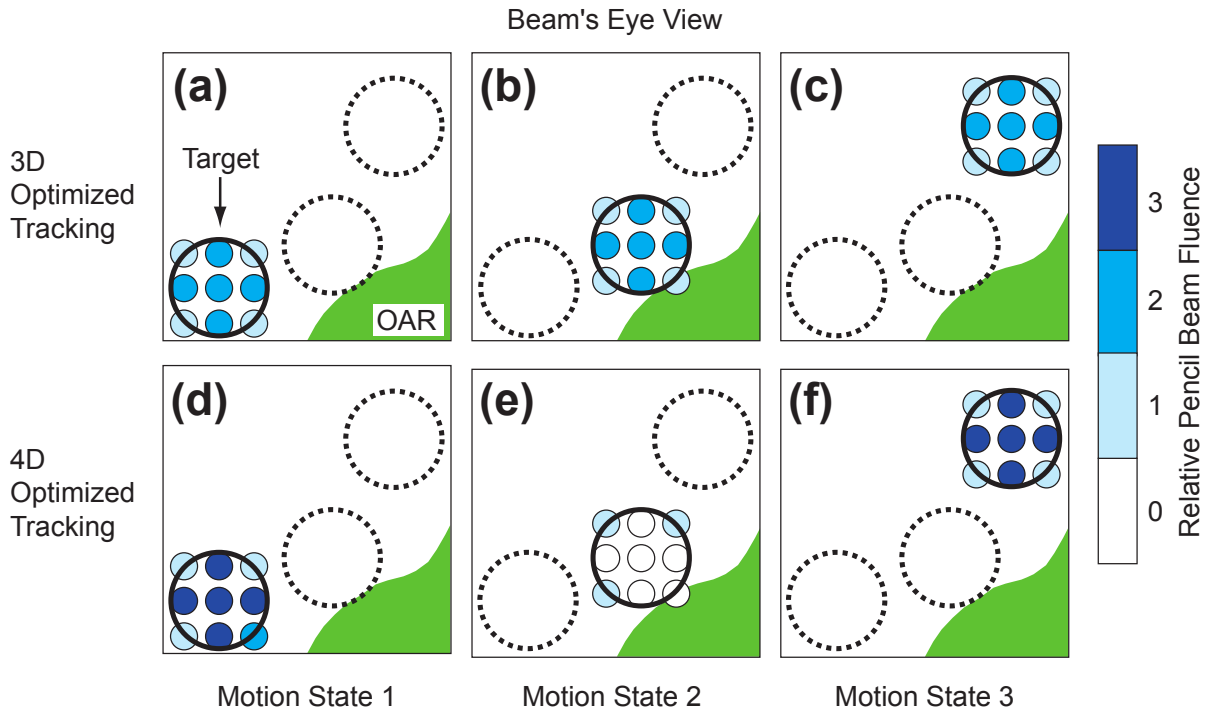
Figure 2.2: Schematic drawing comparing 4D- *versus* 3D-optimized scanned ion beam tracking in beams eye view. A circular target (black) moves between three motion states. For 3D-optimized tracking (a, b, and c) pencil beams (smaller blue circles) track the target motion and deliver identical particle fluence for each motion state. For 4D-optimized tracking, fluence is reduced for Motion State 2 (e) when the target is closest to the organ at risk (green). To compensate, fluence must be increased for pencil beams in Motion States 1 and 3 when the target is furthest from the organ at risk (d and f). Relative fluence is indicated by the shade of blue for each pencil beam.

throughout the CTV for the reference motion state.

(3) To plan beam tracking, deformable image registration vectors and 4DCTs were used to calculate beam tracking offsets for each pencil beam for each motion state, so that each pencil beam would track changes in target position and radiological depth during treatment. Thus, the treatment plan at this stage was composed of a 3D field and a 4D look-up table of tracking offsets (Bert and Rietzel, 2007).

(4) As the starting condition for the 4D field, the 3D field, created in Steps 1 and 2, was copied for each of M motion states, corresponding to states of the 4DCT, to produce a 4D field. Tracking offsets for each pencil beam for each motion state were included in the 4D field description. Initially, particle numbers for each pencil beam in all motion states of the 4D field were identical to those in the 3D field, though scaled uniformly by $1/M$.

(5) For 4D optimization of the particle numbers $\mathbf{N}$ in the 4D fields, a dose correlation matrix $\mathbf{A}$ was calculated that contained the dose contribution, per incident particle number (n_{ijk}), for each ion pencil beam (i) in each motion state (j) for each field (k) to each voxel (p) in the target and avoidance volumes. To calculate the dose correlation matrix elements (a_{ijkp}) of $\mathbf{A}$, 4D pencil beam dose calculations were performed similarly to 3D pencil beam dose calculations except that (1) individual voxel coordinates, defined in a reference motion state, for the target and avoidance volumes were transformed for non-reference motion states using deformable image registration vectors, (2) individual ion pencil beams were offset by their tracking offsets that were determined in Step 3, and (3) the appropriate 3DCT state from the 4DCT was used in dose calculation. The resulting dose correlation matrix was used to calculate 4D dose to the pth (moving) voxel by

$$D_p(\mathbf{N}) = \sum_{k=1}^{B} \sum_{j=1}^{M} \sum_{i=1}^{L_{jk}} a_{ijkp} \, n_{ijk} \tag{2.1}$$

where L_{jk} is the number of pencil beams in an individual motion state j for a given field k. B is the number of fields used, $e.g.$, with different gantry angle or couch angle. In this study, we only used single fields $(B = 1)$, but our TPS developments can be used for multi-field intensity-modulated optimization.

(6) An objective function $\chi^2(\mathbf{N})$ was defined to express differences between the prescribed and actual dose to the target (T) and to penalize dose to avoidance volumes (V) above

a given threshold dose for each avoidance volume (Horcicka, 2011).

$$\chi^2(\mathbf{N}) = \sum_{p \in T} w_T \left(D_{\text{Rx}} - D_p(\mathbf{N})\right)^2 + \sum_{p \in V} w_V \left(D_{\text{Max}} - D_p(\mathbf{N})\right)^2 \Theta \left(D_p(\mathbf{N}) - D_{\text{Max}}\right)$$

(2.2)

where D_{Rx} was the prescribed target dose and the terms w_T and w_V were adjustable parameters to weight the objective function to greater emphasize either prescribed target dose coverage or avoidance volume dose exceeding a maximum allowed value D_{Max}, as desired. The Heaviside step function Θ served to exclude voxels receiving a dose below a user specified maximum dose limit D_{Max} from adding penalty to the objective function. Specifying D_{Max} for avoidance volumes near the target allowed fine control over tradeoffs between the competing objectives of uniform target dose coverage and minimal dose to avoidance volumes.

(7) Conjugate gradients minimization with the Fletcher-Reeves extension (Press *et al.*, 2007) was used to solve for particle numbers $\mathbf{N}$ in the 4D scanned ion field that minimized the objective function.

After optimizing the 4D fields, we were able to compute 4D dose distributions using the existing functionality of TRiP4D (Richter *et al.*, 2013). It should be noted that, in this chapter, we only worked with *absorbed* dose and further development of TRiP4D is needed to allow 4D-optimization of *RBE-weighted* dose. The treatment planning steps described above were used in the following studies for both a moving phantom and a lung cancer patient to test our working hypothesis.

2.2.2 Water Phantom Study

To compare our 4D-optimized scanned ion beam tracking approach against an existing 3D-optimized scanned ion beam tracking approach, we designed a water phantom test case with a moving spherical target deep to a static rectangular solid avoidance volume (cf. Figure 2.3). The mathematical phantom consisted of two rectangular solid slabs. A proximal slab $10 \times 10 \times 2$ cm^3 contained a stationary rectangular solid avoidance volume $2 \times 10 \times 2$ cm^3, upstream of the target, and did not move. A distal slab $10 \times 10 \times 8$ cm^3 contained a 3-cm spherical target volume and oscillated along the x-axis, perpendicular to the beam direction, with sinusoidal motion with 2-cm peak-to-peak amplitude and a 4 s period. We designed this phantom to allow two distant motion states in which beams could deliver dose to portions of the target and while missing the avoidance volume.

For treatment planning simulations, voxelized 4DCT data and contours were gener-
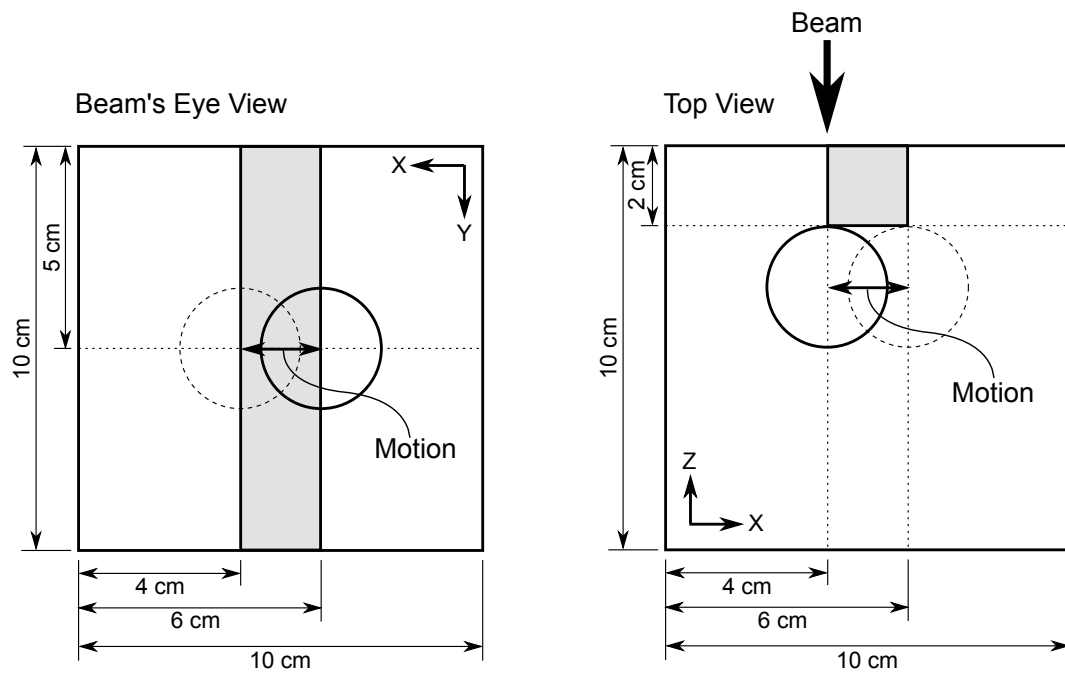
Figure 2.3: Diagram of water phantom test case from 2 viewpoints. A spherical target (black circle) with 3-cm diameter moves laterally along the x-axis with sinusoidal motion ($A_x = 2$ cm, $T = 4$ s) deep to a static proximal avoidance volume (grey shaded rectangle). Beam direction indicated by black arrow. The target is shown by the solid circle in the reference motion state and by the dashed circle at maximal displacement.

ated to represent this phantom, and corresponding image registration vectors were created to describe the sinusoidal motion of the phantom for 11 discrete motion states equally spaced, *i.e.*, in distance, between the minimal and maximal displacement of the moving phantom. Using the TPS, a single scanned carbon ion field was designed to irradiate the spherical target uniformly with 1 Gy, with the beam first passing through the stationary slab containing the avoidance volume. Carbon pencil beam Bragg peak positions were distributed throughout the target with 2 mm lateral spacing and 3 mm water-equivalent depth spacing and focused to approximately 6 mm full-width at half-maximum (FWHM) spot size each, *i.e.*, at the center of the target. A 3-mm ripple filter was used to broaden the width of the carbon Bragg peaks along the depth axis.

The 3D-optimized beam tracking plan was prepared using only steps 1-3 in our described procedure in Section 2.2.1 and was composed of a 3D field and a list of tracking offsets for each pencil beam for each motion state. We did not restrict dose to the avoidance volume in 3D optimization for this water phantom case. For 3D optimization, our solution was considered to have converged and optimization was stopped on once the relative change in our objective function after each iteration dropped below 1×10^{-3}. The 4D-optimized scanned carbon tracking plan was prepared as described in Steps 1-7. For 4D optimization objectives, we included a uniform target dose of 1 Gy ($w_T = 1$) and a maximum dose to the avoidance volume of 0.01 Gy ($w_V = 0.01$). To prevent the occurrence of overly high doses in regions outside the target and avoidance volume, we also added a thin avoidance volume layer, 2-mm depth-thickness at 2-cm depth, throughout the entire proximal slab, with a maximum allowed dose of 1 Gy ($w_V = 1$).

We investigated the rate of convergence of the 4D objective function as a function of the number of iterations. Based on our initial findings, we decided not to use the stopping criteria discussed above but, rather, to continue until 1000 iterations were completed. We will return to this topic in our discussion. 4D dose calculations were performed for both 3D- and 4D-optimized scanned carbon beam tracking for the moving phantom. A 3D dose calculation was also performed for a static reference case without motion.

In summary, our water phantom study compared calculated dose to the target and avoidance volume for (1) static 3D irradiation with the target fixed in the reference motion state, (2) 3D-optimized scanned carbon beam tracking, and (3) 4D-optimized scanned carbon beam tracking. 4D dose distributions were transformed to the reference motion state and visualized using 2D colorwash plots of dose.

2.2.3   Lung Cancer Patient Study

In order to demonstrate that our 4D-optimized beam tracking approach could optimize 4D scanned carbon fields for patients with moving organs, we tested our method for a lung cancer patient, who we will refer to as Lung Patient #1 throughout this work. The 59-year-old woman in our study was diagnosed with stage IV, T2/N2/M1, non-small-cell lung cancer and a 4.5-cm primary tumor in the left lower lobe near the heart. She received stereotactic x-ray radiosurgery at The University of Texas M. D. Anderson Cancer Center (UTMDACC) (Houston, TX). Prior to her treatment, 4DCT image data were acquired with a 16-slice CT scanner (Philips, Mx8000 IDT, Amsterdam, The Netherlands) and binned into 10 phases of the respiratory cycle with equal duration (Keall *et al.*, 2004). Data for this patient were collected under a retrospective research protocol approved by the UTMDACC Institutional Review Board. All protected health information was removed from our copy of the electronic medical record.

In order to plan beam tracking and to perform 4D dose calculations, deformable 4D image registration vectors were calculated from the 4DCT data using the Plastimatch software system (Shackleford *et al.*, 2010). Deformable image registration vectors are shown over a CT slice for the reference phase at end-exhale in Figure 2.4 to illustrate the extent of organ motion in this patient case.

Using the TPS, we designed a single posterior-to-anterior scanned ion field to irradiate the CTV. Although a lone field would most likely not be used clinically, we chose this to evaluate performance of our algorithm at the distal target edge near the heart. For a reference motion state at end-exhale, positions of the carbon pencil beam Bragg peaks were planned to cover the CTV with a uniform 2-mm lateral spacing and focal size of 6-mm FWHM. We used a 3-mm water-equivalent spacing between isoenergy slices and a corresponding 3 mm ripple filter. Particle numbers for each pencil beam were initially optimized in 3D to provide 100% of the prescribed dose to the CTV ($w_T = 1.0$) and zero dose to the heart ($w_V = 10.0$). 3D optimization was stopped once the relative change in the objective function dropped below 1×10^{-3} between each iteration. Where the CTV contours overlapped the heart volume, that volume was treated as target. After planning a 3D field to irradiate the target in the reference motion state, beam tracking offsets were computed for each pencil beam in each motion state using 4D deformable image registration vectors and 4DCT data, as described in steps 1-3 in Section 2.1. For 4D-optimized beam tracking, we performed steps 1-7 in Section 2.1. For 4D optimization, we specified criteria of uniform CTV dose coverage ($w_T = 1.0$) and a limit of zero dose to the heart ($w_V = 10.0$). As in the water phantom study, we investigated convergence of the 4D objective function
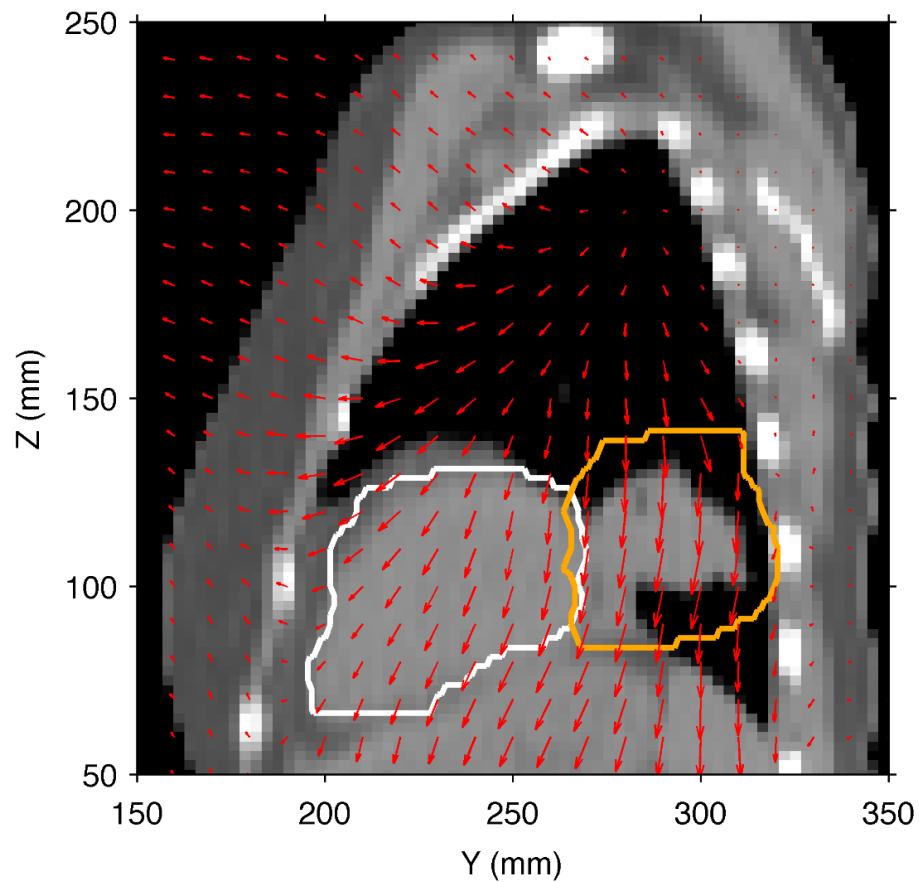
Figure 2.4: Sagittal CT slice for the lung cancer patient in the reference motion state at end-exhale. The CTV is indicated by the orange contour, and the heart contour is shown in white. The overlaid red vectors indicate the YZ components of the deformable image registration vectors and show the movement of tissue to a different motion state at full-inhale.

as a function of the number of iterations. Based on this, we used 1000 iterations with no stopping criteria.

We computed 4D dose distributions in the lung patient for static irradiation, 3D-optimized beam tracking, and 4D-optimized beam tracking. All 4D dose distributions were transformed to a 3D reference state at end-exhale for analysis. Dose distributions were compared using 2D dose colorwash planes, dose volume histograms, and dose-volume statistics.

2.2.4 Validation Experiment

To demonstrate feasibility of delivering 4D-optimized beam tracking therapy, we performed an experiment using the GSI synchrotron with a carbon beam, a motion phantom, and radiographic films. Similar to the mathematical phantom described in Section 2.2.2, a disk-shaped moving target was defined with 3-cm diameter and sinusoidal motion with 2-cm amplitude and 4-s period perpendicular to the beam central axis. We planned a single isoenergy layer of carbon ion pencil beams with 2-mm spacing to deliver uniform dose to the moving target and minimal dose to the static avoidance volume upstream of the target.

Experimentally, this case was represented by 1 radiographic film (Eastman Kodak, X-OMAT V, Rochester, USA) placed, in its jacket, on a motorized table at isocenter on the patient couch and 1 film placed upstream of the motorized table, which did not move. A laser distance indicator was used to detect target motion for our 4D treatment control system. Our experimental setup is shown in Figure 2.5. We delivered our 4D scanned carbon fields to the films using a sequential gating technique. For example, all particles prescribed for motion state 1 were delivered before any particles were delivered for motion state 2. In the case that a motion state change occurred before irradiation was finished, the particle spill was gated by stopping the radiofrequency knockout exciter until the motion table returned to the unfinished motion state and the spill extraction was resumed. In this manner, we irradiated scanned carbon ion treatment plans using both 3D-optimized beam tracking and 4D-optimized beam tracking. Films were processed and digitally scanned using standard methods, and we analyzed the film exposure, *i.e.*, optical density, in both the moving target region and the avoidance region of the films for both 3D- and 4D-optimized beam tracking.
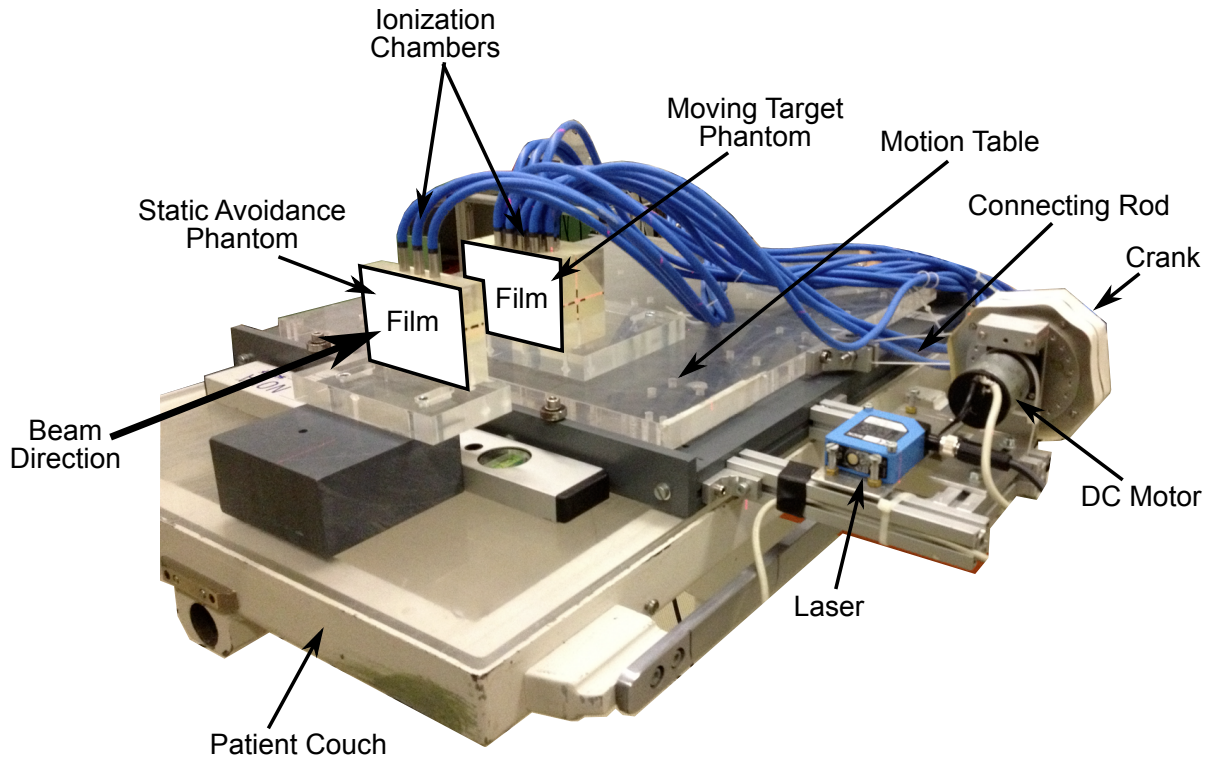
Figure 2.5: Experimental setup for the 4D-optimized beam tracking experiment. The phantom consisted of 2 acrylic pieces (built at the GSI machine shop), which were designed to house an array of ionization chambers and radiographic films. The first phantom piece was positioned stationary upstream of the target. The second moving target phantom piece was mounted on a motion table designed for sinusoidal 1D motion with 2-cm amplitude, driven by an electric DC motor. A laser distance indicator monitored the position of the motion table and transmitted a signal to the 4D treatment control system, which determined the motion state of the phantom for 4D treatment delivery. Although we designed our phantom to hold ionization chambers (shown), these were not installed during our experiment due to severe time constraints.
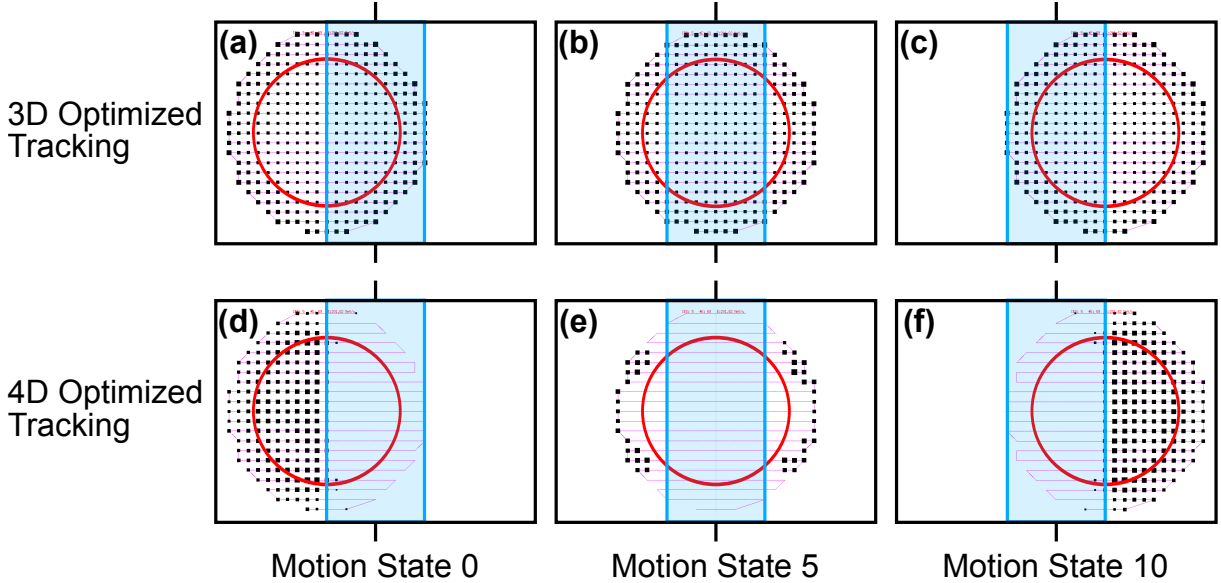
Figure 2.6: Beams eye views of carbon ion scan patterns, *i.e.*, fluence maps, for a single energy (201.65 MeV/u) comparing 3D-optimized beam tracking (a, b, c) and 4D-optimized beam tracking (d, e, f). The ion scan path (thin pink line), stationary avoidance volume (blue rectangle) and moving target (red circle) are shown for exemplary motion states 0 (a, d), 5 (b, e), and 10 (c, f). Relative particle numbers for each pencil beam are indicated by the size of the black squares.

2.3 Results

Overall, we observed that 4D optimization performed as expected. The added degrees of freedom attained by adjusting particle numbers for each pencil beam for each motion state allowed advantages such as reduced dose to avoidance volumes and improved target dose uniformity.

2.3.1 Water Phantom Study

Carbon ion particle numbers $\mathbf{N}$ were determined for 3D- and 4D-optimized beam tracking. Fluence maps for a single energy-slice are shown in Figure 2.6. As expected, particle numbers were reduced by 4D optimization for certain motion states for pencil beams that passed through the static avoidance volume to reach the deeper target. To compensate this, particle numbers were increased using 4D optimization for those motion states that allowed pencil beams to irradiate the target without passing through the proximal avoidance volume.

In 4D optimization, the evaluation of the objective function $\chi^2(\mathbf{N})$ is shown as a

function of iteration number in Figure 2.7. To better visualize dosimetric improvements as a function of iteration number, 4D dose distributions are plotted for various iteration numbers in Figure 2.8. Due to our choice of optimization constraints, the target dose was drastically decreased in the first iteration to spare dose to the avoidance volume. However, after a large number of iterations the target dose coverage was restored, even though a reduction of dose to the avoidance volume was maintained.

Figure 2.9 plots 2D dose colorwash planes comparing 4D-optimized beam tracking against 3D-optimized beam tracking, along with a static irradiation. Dose to the avoidance volume for 4D-optimized beam tracking was greatly reduced, mean dose decreased by 70% and maximal dose decreased by 53%, compared to 3D-optimized plans. Dose statistics for the moving sphere and avoidance volume are presented in Table 2.1 for each treatment plan. For all treatment plans, dose coverage to the moving target was nearly identical. For the avoidance volume, dose distributions for the 3D-optimized beam tracking plan and the static irradiation plan were similar, though the dose distribution for 3D-optimized tracking appeared generally blurred along the x-axis in the proximal, stationary slab containing the avoidance volume, as expected because the carbon pencil beams were laterally tracking the deeper moving target during irradiation.

2.3.2   Lung Cancer Patient Study

For the lung cancer patient, we observed a lesser ability to minimize dose to the avoidance volume, *i.e.*, the heart, than observed for our water phantom study, using 4D-optimized beam tracking instead of 3D-optimized beam tracking. However, we achieved a highly uniform target dose using 4D optimization, similar to that for a static irradiation. Dose colorwash planes comparing 4D-optimized tracking against 3D-optimized tracking and static irradiation are shown in Figure 2.10 for the lung cancer patient. The same data are shown in DVH form in Figure 2.11. In addition, the evaluation of the objective function $\chi^2(\mathbf{N})$ is shown as a function of iteration number in Figure 2.12 for the lung patient. For the static irradiation, the target dose distribution appeared uniform throughout the CTV. 3D-optimized beam tracking provided a dose distribution that remained conformal to the geometric target boundary. However, degradation of dose uniformity was observed inside the target with regions of overdose and underdose. In particular, a region of overdose extends distally beyond the CTV into the heart. This non-ideal dose coverage likely results because 3D-optimized tracking does not compensate for dosimetric effects of rotating or deforming tissues or for changes in the scattering properties of material upstream of the target. We describe these issues in further detail in the discussion section. In summary,

Figure 2.7: Objective function (top) and relative change in objective function (bottom) *versus* number of iterations for 4D-optimized beam tracking for the water phantom. The erratic shape of the relative change in objective function in early iterations led us to abandon our typical criteria for terminating optimization, *i.e.*, to stop when the relative change dropped below 1×10^{-3}. Instead, we estimated from these plots that the relative change in the objective function become stable and remains below 1×10^{-3} near 1000 iterations. Thus we used 1000 iterations of 4D optimization without any abort criteria for the rest of our study, and we visually confirmed that the objective function did not worsen by neglecting the typical stopping criteria.
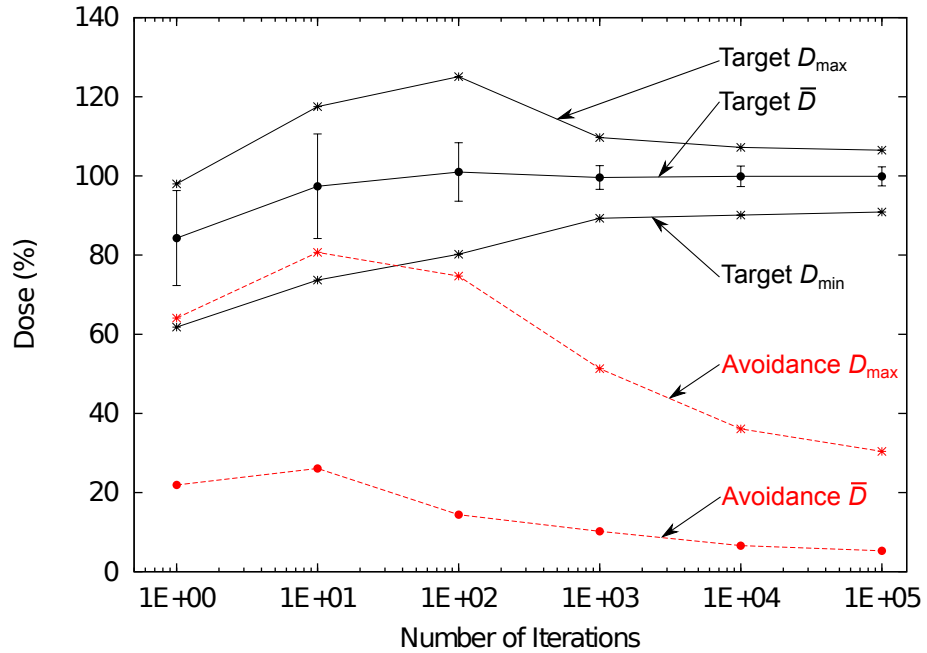
Figure 2.8: Target and avoidance volume dose statistics *versus* number of iterations for 4D-optimized beam tracking for the water phantom. Target mean ($\bar{D}$), standard deviation (error bars), minimum ($D_{\min}$), and maximum dose ($D_{\max}$) are shown by the black markers connected by solid lines. Avoidance volume mean and maximum dose are shown by the red markers connected by dashed lines. During the first 10 iterations, dose is increased both to the target and the avoidance volume. After the target dose stabilizes near iteration 1000, a continued reduction in maximum dose to the avoidance volume is seen even up to 100,000 iterations, inspiring us to investigate other minimization algorithms in future studies.
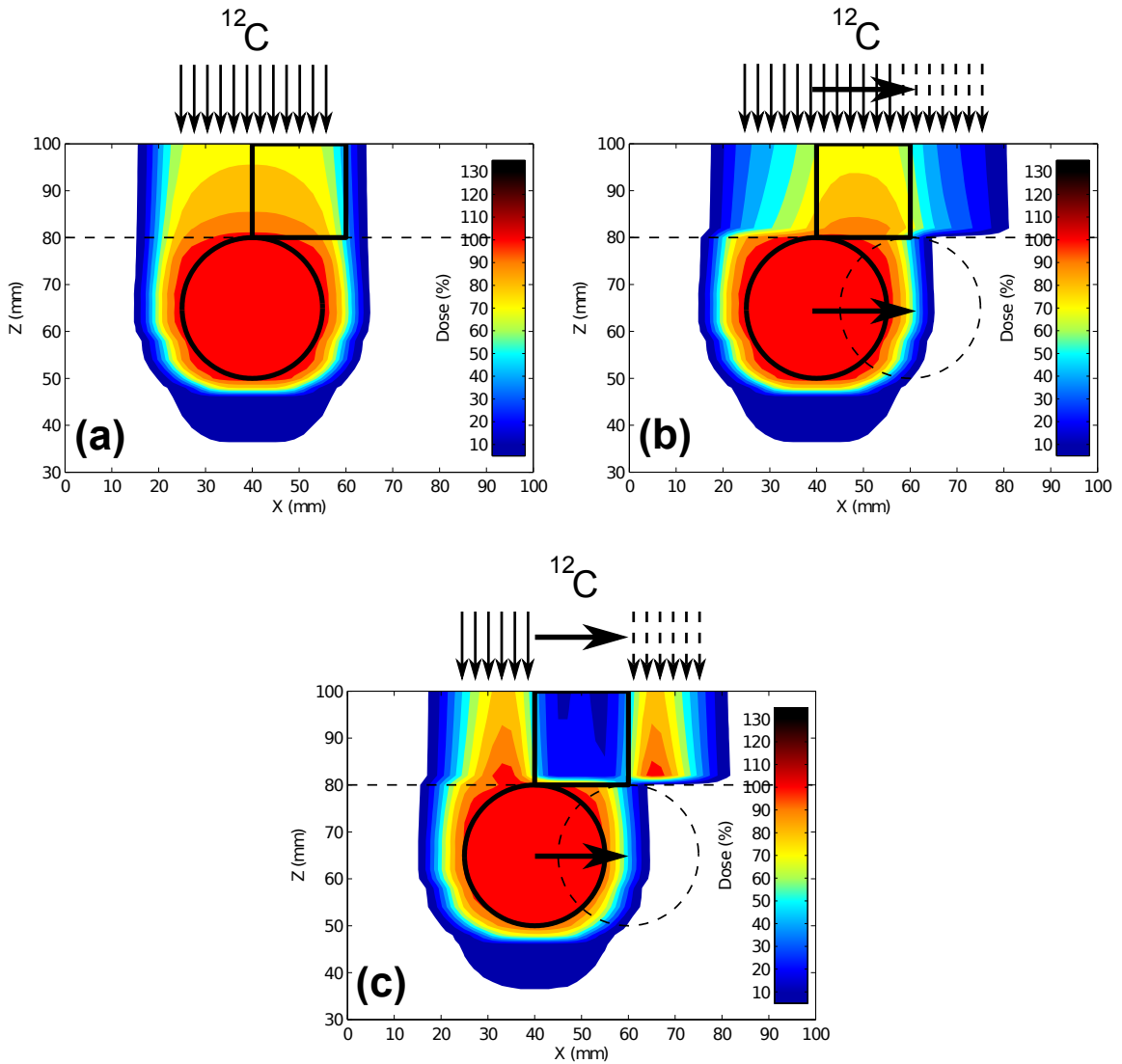
Figure 2.9: XZ dose colorplanes for the moving sphere target in a water phantom with a static proximal avoidance volume. 4D dose distributions were calculated for (a) 3D-optimized carbon static plan for a non-moving target in the reference motion state, (b) 3D-optimized carbon beam tracking plan for a moving target, and (c) 4D-optimized carbon beam tracking plan for a moving target. Sphere target shown in the reference position (solid circle) and at maximal displacement (dashed circle). The proximal avoidance structure (solid square) and water above Z = 80 mm (dashed line) did not move. Illustrations of carbon pencil beam fluence for each case are shown above the phantoms to demonstrate: (a) pencil beams do not move, (b) pencil beams track the lateral motion of the sphere target, but fluence for each pencil beam is identical to the static 3D plan, and (c) pencil beams track the lateral motion of the target with pencil beam fluence optimized for each motion state to best spare the avoidance structure and maintain target coverage.

Table 2.1: Dose and volume statistics comparing 3D optimized static delivery, 3D optimized beam tracking, and 4D optimized beam tracking for both the water phantom and lung cancer patient studies. Data reported as percentages. Difference calculated as $100\% \times$ (4DOBT − 3DOBT)/3DOBT.

Study	Volume	Metric	Static	3DOBT	4DOBT	Difference (%)
Phantom	Target	$\bar{D}$	100.0	100.0	99.9	0
		σ_D	0.3	0.3	0.4	+58
		$D_{\min}$	98.3	98.3	97.3	-1
		$D_{\max}$	101.2	101.2	101.5	0
		V_{95}	100.0	100.0	100.0	0
		V_{107}	0.0	0.0	0.0	0
		$D_5 - D_{95}$	1.8	1.8	1.9	+1
	Avoidance	$\bar{D}$	23.8	26.1	7.7	**-71**
		$D_{\max}$	91.5	89.4	42.2	**-53**
Patient	CTV	$\bar{D}$	99.9	95.4	100.0	+5
		σ_D	1.9	12.0	0.9	-93
		$D_{\min}$	34.2	37.9	54.7	+44
		$D_{\max}$	114.5	126.7	108.9	-14
		V_{95}	99.7	50.4	99.9	+98
		V_{107}	0.2	19.5	0.1	-100
		$D_5 - D_{95}$	2.0	38.7	1.9	-95
	Heart	$\bar{D}$	7.0	6.9	7.1	**+3**
		$D_{\max}$	104.7	119.4	103.8	**-13**
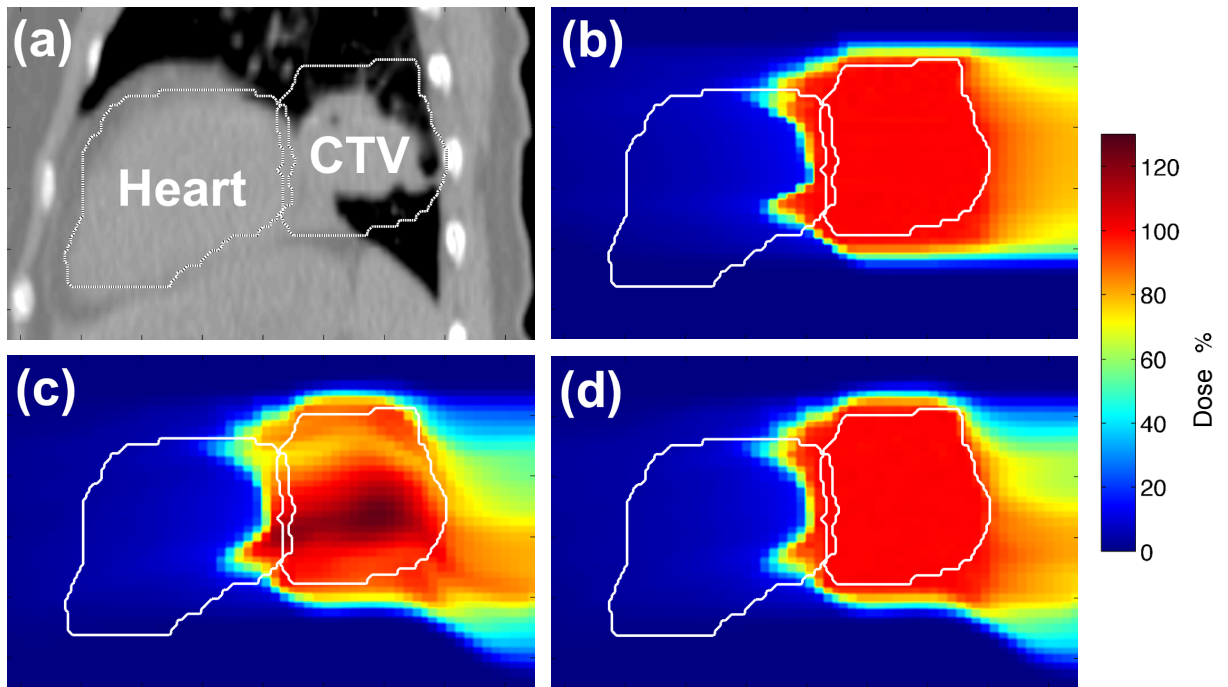
Figure 2.10: Sagittal cuts showing (a) CT image of lower thorax, (b) 3D dose for the 3D-optimized carbon static plan ignoring motion, (c) 4D dose for the 3D-optimized beam tracking plan, (d) 4D dose for the 4D-optimized carbon beam tracking plan. All 4D dose distributions were transformed to the reference motion state at end-exhale for analysis. Note the increased uniformity of CTV dose using 4D-optimized beam tracking (d) instead of 3D-optimized beam tracking (c).
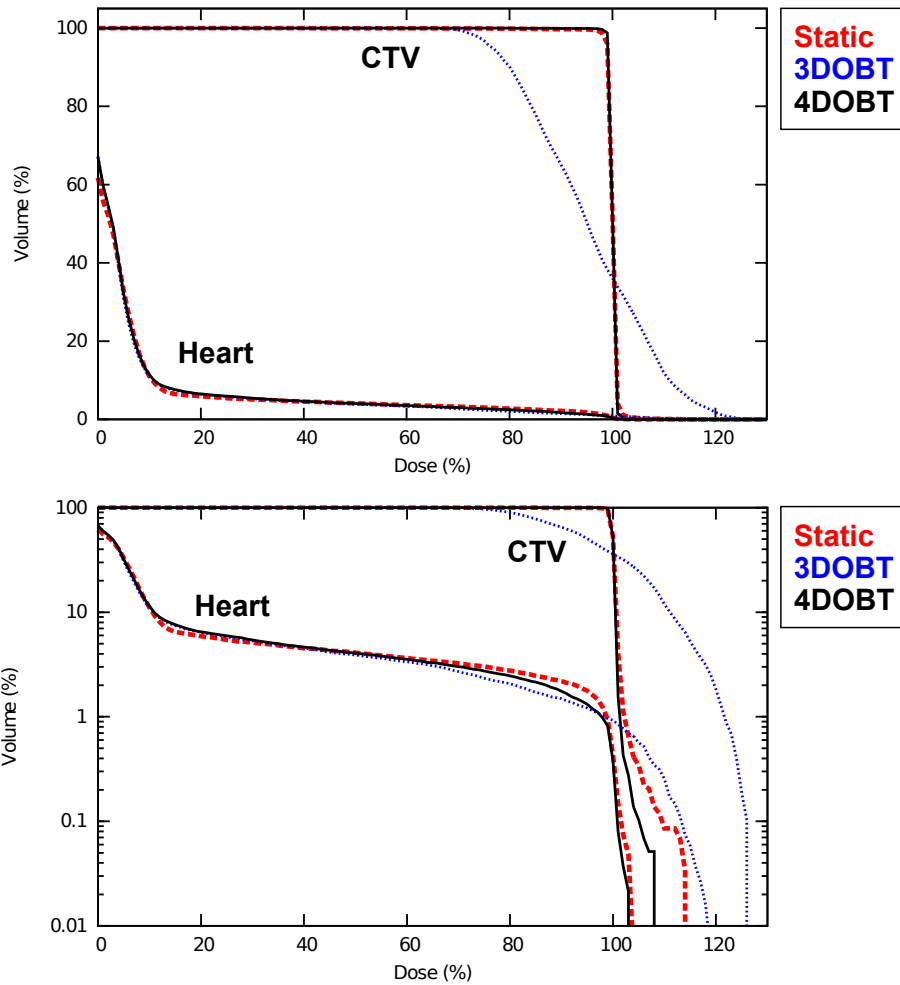
Figure 2.11: 4D cumulative DVHs for the lung CTV and the heart shown in linear (top) and semilog (bottom) scales comparing (1) 3D-optimized static plan (dashed red line), (2) 3D-optimized beam tracking (dotted blue line), and (3) 4D-optimized beam tracking (solid black line). 4D-optimized beam tracking appears similar to the static plan with more uniform target dose coverage and slightly reduced maximal dose to the heart, compared with 3D-optimized beam tracking.
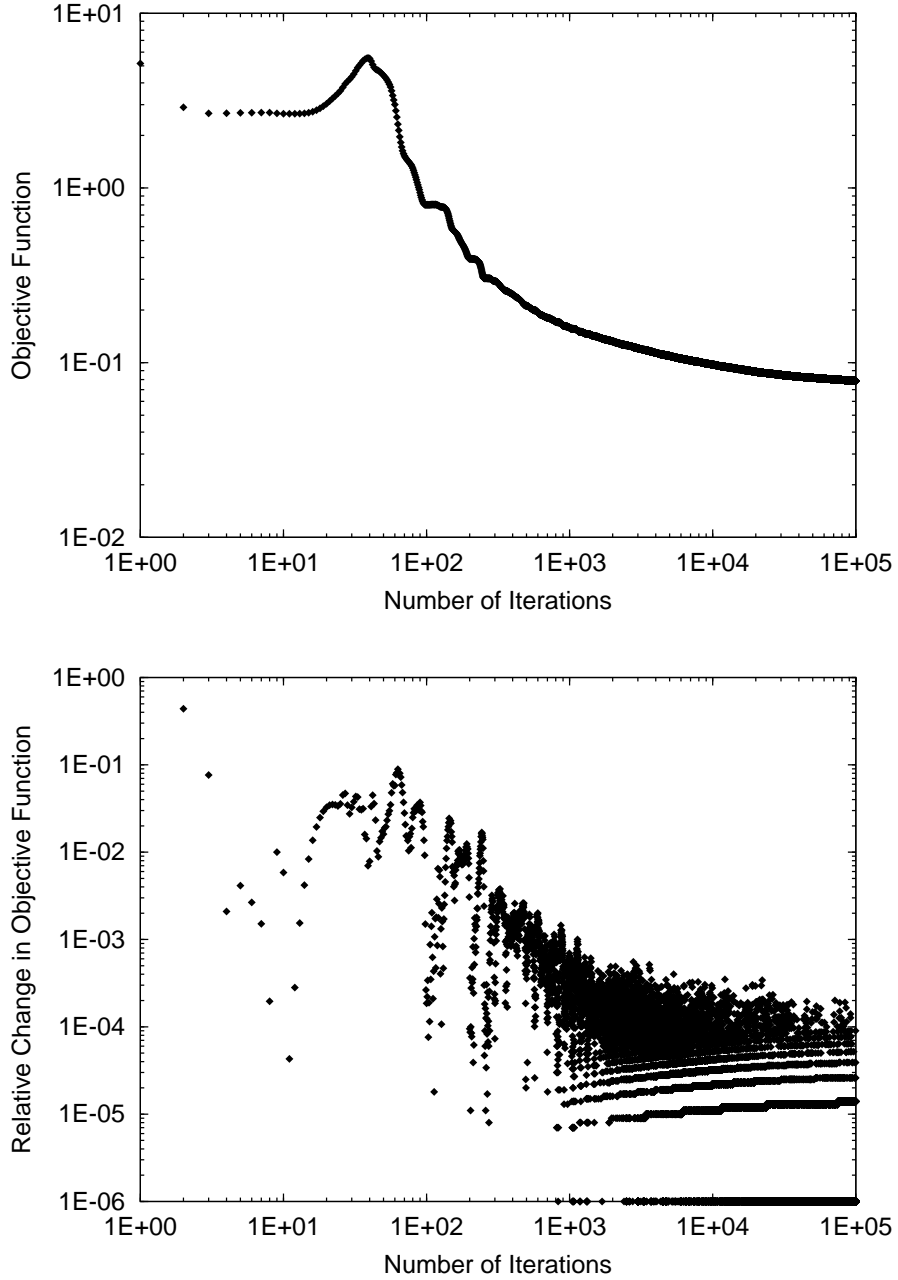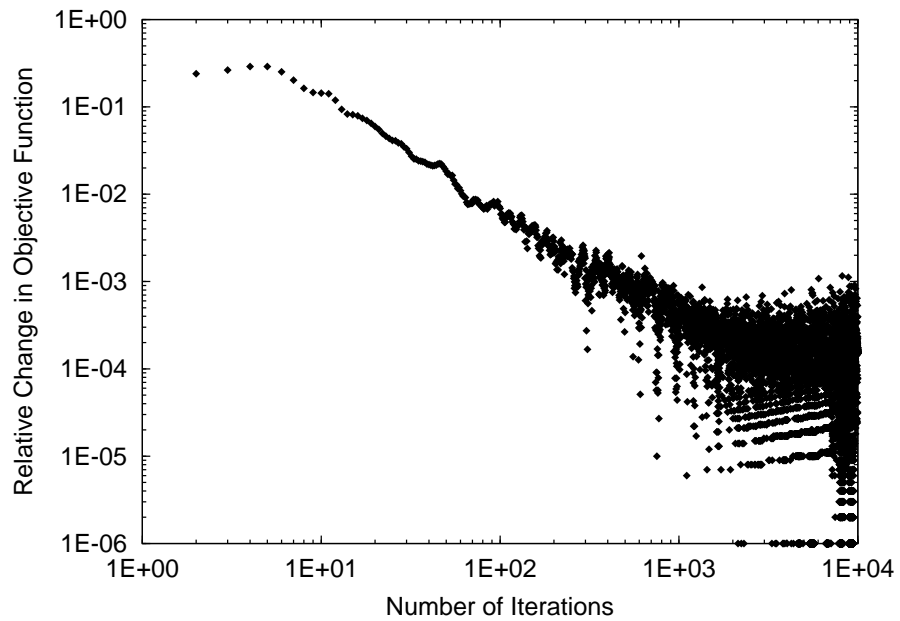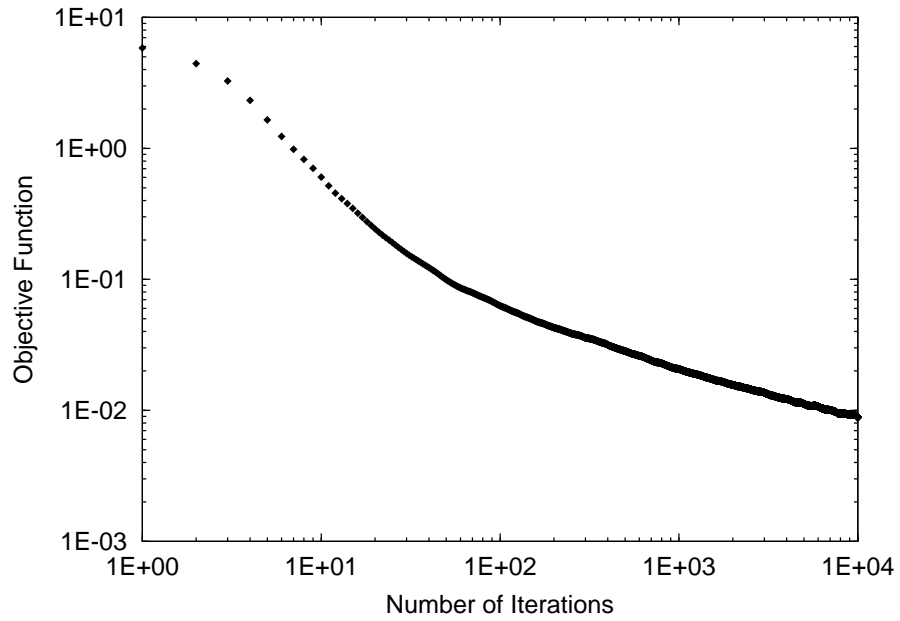
Figure 2.12: Objective function (top) and relative change in objective function (bottom)*versus* number of iterations for 4D-optimized beam tracking for the lung patient. Similar to the water phantom results (cf. Figure 2.7), we observed from these plots that the relative change in the objective function is somewhat erratic but seems to fall consistently below 1×10^{-3} near 1000 iterations.

4D-optimized beam tracking improved target dose uniformity, compared to 3D-optimized beam tracking. In addition, by using 4D-optimized tracking we observed a 13% decrease in maximum dose to the heart, compared to 3D-optimized tracking (cf. Table 2.1). Analysis of the organ motion seen in the deformable image registration map (cf. Figure 2.4) suggests that similar motion between the lung CTV and the heart restricted our ability to reduce dose to the heart as greatly as that possible in our water phantom study.

2.3.3 Validation Experiment

We experimentally confirmed the ability of 4D-optimized beam tracking to reduce dose to an avoidance volume near a moving target compared with 3D-optimized beam tracking for our moving target phantom using a scanned carbon ion beam at GSI. Figure 2.13 shows our film measurements from the 4D-optimized beam tracking validation experiment. We observed that 4D-optimized beam tracking provided a similar uniformity of film darkening to 3D-optimized beam tracking for the moving target, with mean optical densities of film in the target region of 1.00 ± 0.14 and 1.00 ± 0.10, respectively. However, 4D-optimized beam tracking provided much less dose to the avoidance region than 3D-optimized beam tracking, as seen in the lighter film exposure in that region, with mean optical densities in the avoidance region of 0.26 and 0.71, respectively, and max optical densities in the avoidance region of 0.79 and 1.37, respectively. Thus, using 4D-optimized beam tracking instead of 3D-optimized beam tracking reduced the mean film exposure in the avoidance region by 63% and reduced the max film exposure in the avoidance region by 42%. These measurements support our findings *in-silico* and provide evidence that our 4D-optimized beam tracking approach is technically feasible to deliver using a carbon ion synchrotron.

2.4 Discussion

In conclusion, we confirmed our hypothesis that 4D-optimized scanned ion beam tracking can reduce the maximum dose to avoidance volumes near a moving target compared with 3D-optimized scanned ion beam tracking. In addition, 4D-optimized beam tracking substantially improved target dose homogeneity for a lung tumor, compared with 3D-optimized beam tracking.

In our water phantom study, we demonstrated that a drastic reduction in dose to avoidance volumes near a moving target is possible using 4D-optimized beam tracking instead of 3D-optimized beam tracking. The clinical significance of this finding will likely depend greatly on the exact motion characteristics of the target and avoidance tissues for
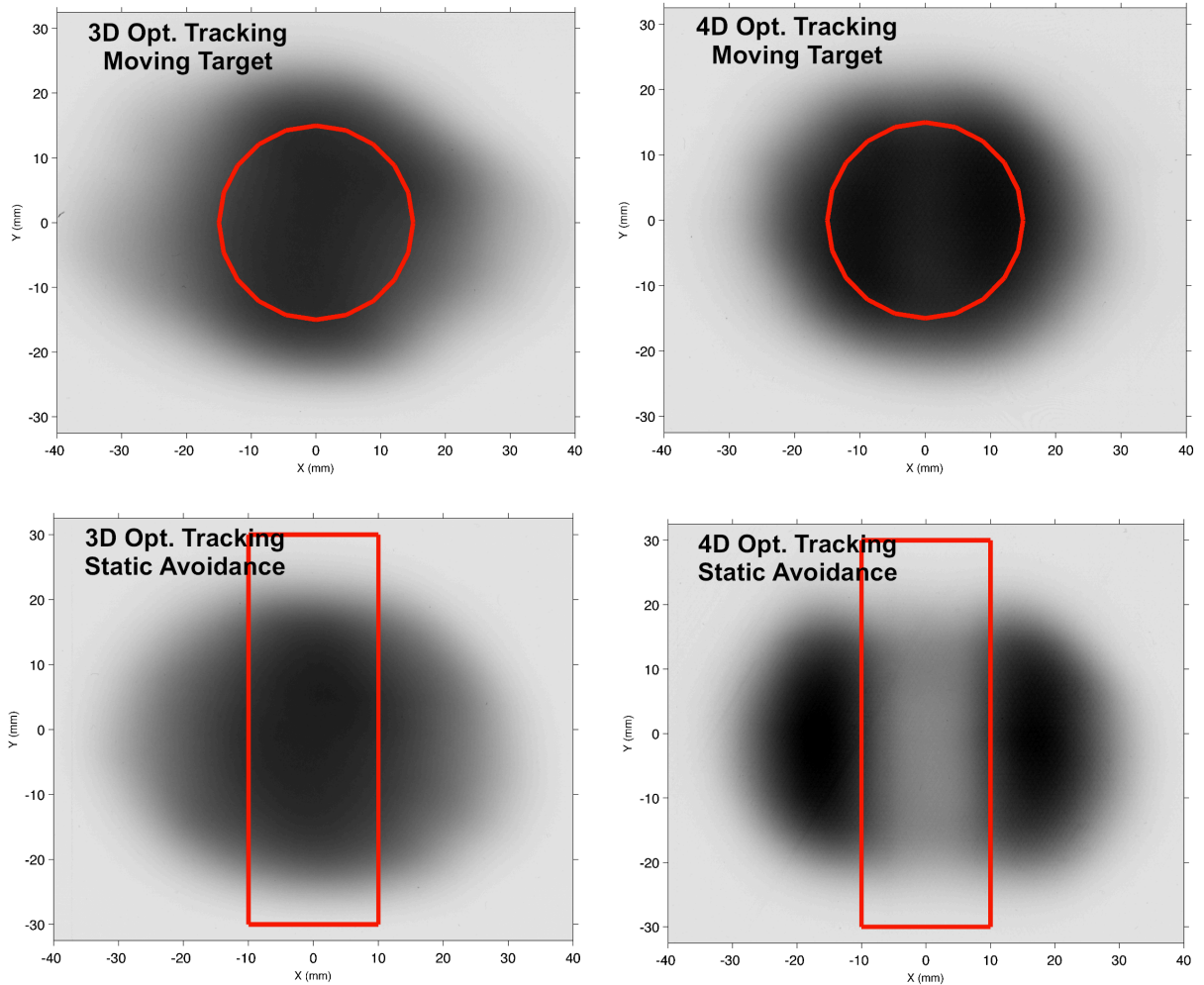
Figure 2.13: Experimental film results for scanned carbon ion delivery of 4D-optimized beam tracking (right) *versus* 3D-optimized beam tracking (left) using the GSI synchrotron facility. We found that 4D-optimized beam tracking drastically reduced dose to the static avoidance volume (red rectangle), as seen by less film darkening compared to 3D-optimized beam tracking, while both approaches produced similar uniform darkening of the moving circular target.

individual patients. In our lung cancer patient study, we observed a less dramatic sparing of dose to the heart using 4D optimization. The less dramatic sparing of the avoidance volume seen in the patient compared with the water phantom is likely a consequence of the nearly identical motion between the target and the avoidance volume, *i.e.*, the heart.

Thus, it appears that differential motion between target and avoidance volumes is a likely prerequisite to achieve clinically significant reductions in dose to avoidance volumes using 4D-optimized scanned ion beam tracking. Therefore, more patient studies are required to isolate patient populations that would benefit most from this therapy. Of perhaps equal importance, we found that 4D-optimized beam tracking could drastically improve target dose coverage and dose uniformity for the lung cancer patient. This finding potentially benefits a large class of patients with targets that undergo periodic motion during treatment. Also, 3D-optimized beam tracking seems to pose a risk for degraded uniformity of tumor dose, compared to both 4D-optimized beam tracking and static dose simulations. This cautions that using beam tracking for deforming tissue *without* using 4D optimization or other correction methods (*e.g.*, those of Lüchtenborg *et al.* (2011)) may provide dosimetrically worse coverage than beam gating.

For 3D-optimized beam tracking for the lung patient, this finding of non-uniform target dose for "perfect" tracking agrees with previous studies of Bert and Rietzel (2007) and van de Water *et al.* (2009) who reported that dose degradation can result from issues that are not considered in 3D-optimized beam tracking, namely rotations, deformations, and changes in scattering properties of tissue upstream to the target. For example, if the target rotates, the entrance channel dose for individual pencil beams can overlap in irregular patterns. If the target deforms, the geometric spacing between pencil beams may change, and due to the high dose gradients for each pencil beam, one may observe overdose when volume contraction occurs and underdose when volume dilation occurs. Further, if the target moves, even rigidly, beneath heterogeneous tissue upstream of the target, *e.g.*, lung tumor moving beneath ribs, the multiple Coulomb scattering of individual pencil beams, and thus distribution of off-axis target dose contributions, will not be uniform for all motion states even if the range variations are compensated by beam tracking. Some of these issues were recently addressed by the study of Lüchtenborg *et al.* (2011), who developed a real-time 4D dose correction method that achieved improved target dose coverage compared with 3D-optimized beam tracking. The advantage of their method compared to ours might be faster patient throughput, since their technique allows irradiation of the patient during any given motion state. In contrast, our approach solves a 4D field that potentially better spares avoidance volumes and might offer slightly more uniform target dose but must be delivered during specific motion states, similar to gating.

In comparison to published literature on 4D-optimization for photon therapy, our approach was similar to that of Trofimov *et al.* (2005), using a deforming dose calculation grid and discrete motion states, though scanned ion beam therapy includes an additional degree of freedom compared to photon therapy, due to the multiple isoenergy layers. Our findings for the lung patient are consistent with those of Trofimov *et al.* (2005), who found only slight reductions of dose to avoidance volumes for lung and liver patients using 4D-optimized photon beam tracking instead of photon beam gating. Similar to Chin and Otto (2011), we observed large ability to spare avoidance volumes near moving target for phantom cases.

Our study had several notable strengths. To our knowledge, this is the first study of 4D optimization for scanned ion beam therapy of moving tumors reported in the literature. We achieved improved target dose coverage and reduced dose to avoidance volumes by incorporating the entire 4DCT data set into 4D optimization of the scanned ion fields. Since we use the 4DCT and deformable image registration vectors in optimization, our approach provided a more uniform target dose than 3D-optimized beam tracking for a moving target in heterogeneous tissue. In addition, we validated our work with an experiment using a scanned carbon ion beam and a moving phantom.

Our study had several limitations. One was that we did not consider uncertainties in patient motion, and we assumed that the exact characteristics of patient anatomy and motion could be represented by a single planning 4DCT. Though our approach allows variation in respiratory rate, we ultimately assumed that motion was periodic. Any substantial deviations from that assumption could result in treatment failure. However, this limitation was not important in the context of this study because we only sought to demonstrate proof-of-principle that 4D optimization could potentially provide a benefit for scanned ion therapy for moving organs. A second limitation was that we only considered *absorbed* dose from scanned carbon ion therapy, *i.e.*, our modifications of the TRiP4D research code to allow simulation of 4D-optimized beam tracking did not allow optimization of RBE-weighted dose for our lung patient. Further work is needed to connect our approach with a method to optimize RBE-weighted dose, *e.g.*, the Local Effect Model used at GSI. Third, in this work, we encountered computer memory limitations during 4D optimization due to the large problem size when using our current 32-bit treatment planning system. Therefore, we downsampled the 4DCT images from original voxel sizes of (0.98 x 0.98 x 2.5) mm^3 to voxel sizes of (2.93 x 2.93 x 2.5) mm^3. This limitation is currently being addressed by extension of TRiP4D to utilize 64-bit computer architecture. A fourth limitation was that we only investigated one minimization algorithm, *i.e.*, conjugate gradients, which may converge on local minima rather than a global minimum. Fifth, we only investigated one

beam angle for each test case. However, our codes can be used to optimize multiple beams simultaneously to plan 4D-optimized intensity modulated particle therapy. Some of these limitations were intended by the design of our study and allowed us to see things that could have otherwise been confounded by increasing the complexity of our study. While we acknowledge these limitations of our work, they did not prevent us from achieving our goals, which were to demonstrate proof-of-concept for a new beam tracking approach using 4D optimization and to investigate possible dose reductions for avoidance volumes near moving targets. In addition, some of these limitations are addressed in the following chapter.

4D optimization for scanned ion therapy has many possible avenues for future work. For example, 4D optimization might be used to simplify the beam tracking system at GSI. By using an appropriate starting condition, such as a 4D scanned ion field with a pencil beam grid covering the full range of target motion and range changes, one might eliminate the need for tracking offsets and, rather, achieve tracking solely by optimizing the particle numbers for pencil beams in the rigid grid for each motion state. For patients with slightly irregular motion trajectories, it should be theoretically possible to incorporate several 4DCT series into the optimization of a single beam tracking plan that is more robust to each possible trajectory represented by the individual 4DCTs. For chaotic motion, such as seen in the abdomen near the bowel, the 4D optimization concept could potentially be modified to provide a robust 3D field solution that is optimized using multiple 3DCT image sets acquired, *e.g.*, on different days prior to treatment.

In summary, we developed and tested a 4D-optimized beam tracking approach for scanned ion therapy that provided reduced dose to avoidance volumes and improved target dose coverage for a patient with a moving target, compared with 3D-optimized beam tracking. Theoretically, these dosimetric advantages can be used either to provide reduced risk of treatment side effects when target doses are designed for a standard tumor control probability or can allow increased target doses and improved tumor control probability when risks of treatment side effects are allowed to approach those risk levels typical of standard care. Either avenue may be valuable to improving patient outcomes.

Chapter 3

Robustness of Target Dose Coverage to Motion Uncertainties for Scanned Carbon Ion Beam Tracking Therapy of Moving Targets

3.1 Introduction

Actively scanned carbon ion beams have been use to safely treat a number of static tumors such as chordomas, chondrosarcomas, and osteosarcomas of the skull base, spine, and sacrum as well as adenoid cystic carcinomas of the salivary glands (Kraft, 2000; Schulz-Ertner *et al.*, 2004). Given the high tumor control rates and low toxicity observed for those patients (Schulz-Ertner *et al.*, 2004), there is motivation to utilize the scanned carbon ion beam for new cancer sites, for example, non-small-cell lung cancer and hepatocellular carcinoma. Indeed, these sites have already been treated successfully with passively scattered carbon ion beams (Tsujii *et al.*, 2004). However, one of the strongest arguments against using *scanned* ion therapy is that the dose distributions are highly sensitive to errors and uncertainties in treatment planning and treatment delivery. For the same reasons that scanned ion beams are beneficial, namely the sharp dose gradients and high LET found near the ion Bragg peaks, scanned ion beams can be dangerous to patients if delivered incorrectly. In Chapter 2, we investigated the theoretical dosimetric advantages of using scanned carbon ion beam tracking for moving tumors, when treatment was delivered perfectly, *i.e.*, with no errors. In this chapter, we investigate the robustness of scanned carbon ion beam tracking in order to understand whether its theoretical benefits can persist in the presence of uncertainties in patient motion, also considering the limited precision of a scanned carbon ion beam tracking system.

Several investigators have studied the robustness of scanned ion therapy to uncertainties in treatment planning, treatment delivery, and patient alignment (Pflugfelder *et al.*, 2007; Lomax, 2008a,b; Meyer *et al.*, 2010). For example, if the patient is misaligned or exhibits a change in anatomy during a course of therapy, ion Bragg peaks may miss their planned target position, leading to potential underdosage of the target or overdose to critical structures outside of the target. If the target is moving, interplay effects between organ motion and ion scanning, as discussed in Section 1.4, can further complicate this problem, potentially leading to treatment failure if adequate motion mitigation strategies are not used (Bert and Durante, 2011). Beam tracking might enable the use of scanned carbon ion therapy for moving tumors, but robustness analyses are needed to understand the reliability of such a strategy.

As discussed in Section 2.1, scanned carbon ion beam tracking relies on a real-time motion state detection system and applies tracking offsets to each scanned pencil beam coordinate for each motion state so that the beams are steered to follow motion of the target for all phases of respiration (Grözinger *et al.*, 2004). Currently, beam-tracking offsets are computed prior to treatment using a planning 4DCT. Deformable image registration vectors are calculated from this 4DCT to map the motion of tissues throughout the respiratory cycle, and these vector maps are used to compute tracking offsets required for each pencil beam for each phase of respiration (Bert and Rietzel, 2007). Similar to beam gating, this approach relies on the assumption that the planning 4DCT adequately represents the internal motion of the patients organs during treatment delivery, and that a correlation between the patient respiratory phase and the position of internal organs is reliable for the duration of treatment.

It is not yet known how robust scanned carbon tracking is against errors and uncertainties in these treatment elements. Due to the high dose gradients found in scanned carbon-ion therapy, uncertainties in organ motion and technical limitations of a beam-tracking delivery system might lead to unacceptable target dose coverage when correlations are lost between respiratory phase and internal organ position. van de Water *et al.* (2009) studied beam tracking with scanned *proton* beams and reported deterioration of target dose coverage when simulated time delays or position errors were introduced to tracking simulations, which was improved by combining the principles of rescanning and beam tracking. To our knowledge, the robustness of target dose coverage to uncertainties in scanned carbon ion beam tracking therapy for moving tumors has not been reported in the literature.

The purpose of this study was to evaluate the robustness of target dose coverage to motion uncertainties for scanned carbon ion beam tracking therapy of moving targets. To accomplish this, we simulated scanned carbon ion beam tracking for moving targets in both

water phantoms and a sample of lung cancer patients using a research treatment planning system for ion radiotherapy. We modeled various deviations from perfect tracking that could arise due to uncertainty in organ motion and limited precision of a scanned ion beam tracking system. We calculated 4D dose to moving targets for many combinations of these modeled uncertainties. We also investigated the effects of interfractional changes in organ motion on target dose coverage by simulating treatment using multi-week 4DCTs for 6 lung cancer patients. In relation to our central hypothesis (cf. Section 1.5), this study seeks to quantify the reliability, efficacy, and safety of 3D-optimized beam tracking, which might one day be used to deliver scanned ion therapy to patients with thoracic tumors.

3.2   Methods

3.2.1   Robustness of Beam Tracking to Motion Uncertainties for 4 Phantoms

Design of Water Phantoms

We designed 4 mathematical phantoms with increasing degrees of complexity to evaluate scanned carbon ion beam tracking. The phantoms are shown in Figures 3.1, 3.2, and 3.3. Phantoms 1 and 2 were inspired by patients with liver cancer, *i.e.*, a moving tumor in relatively homogeneous tissue, and Phantoms 3 and 4 were inspired by patients with lung cancer, *i.e.*, a moving tumor in heterogeneous tissue. All phantoms were $10 \times 10 \times 10$ cm^3, consisting of cubic voxels with dimension $1 \times 1 \times 1$ mm^3. In all phantoms, a 3-cm diameter spherical target oscillated with sinusoidal motion, with displacement s as a function of time t expressed as $s = A sin^4(\pi t/\tau)$ (Lujan *et al.*, 1999). We studied respiratory periods τ of 3, 4, and 5 s. In Phantom 1, the sphere oscillated along the x-axis, perpendicular to the beam axis (z), in a homogeneous water box with amplitude (A) of $A_x = 2$ cm, *i.e.*, no depth changes. In Phantom 2, the sphere moved in 3 dimensions, again in a homogeneous water box, with $A_x = 2$ cm, $A_y = 0.5$ cm, and $A_z = 1$ cm, with depth changes up to 1 cm along the z-axis. In Phantom 3, the target moved along the x-axis in water as in Phantom 1, but a simulated rib heterogeneity was positioned upstream of the target in water to introduce changes in radiological depths of the target voxels. The rib was approximated as a cylinder with 1-cm diameter, inferred from anatomical cross-section measurements of human ribs reported by Mohr *et al.* (2007), and 10-cm length parallel to the y-axis with uniform Hounsfield value of 750 (Schneider *et al.*, 2000). In Phantom 4, the rib heterogeneity of Phantom 3 was replaced by an air cavity with identical dimensions to the rib cylinder, but with uniform Hounsfield value of -1000. For each phantom, we generated target contours, 4DCT data, and image registration vector maps to use in treatment planning,
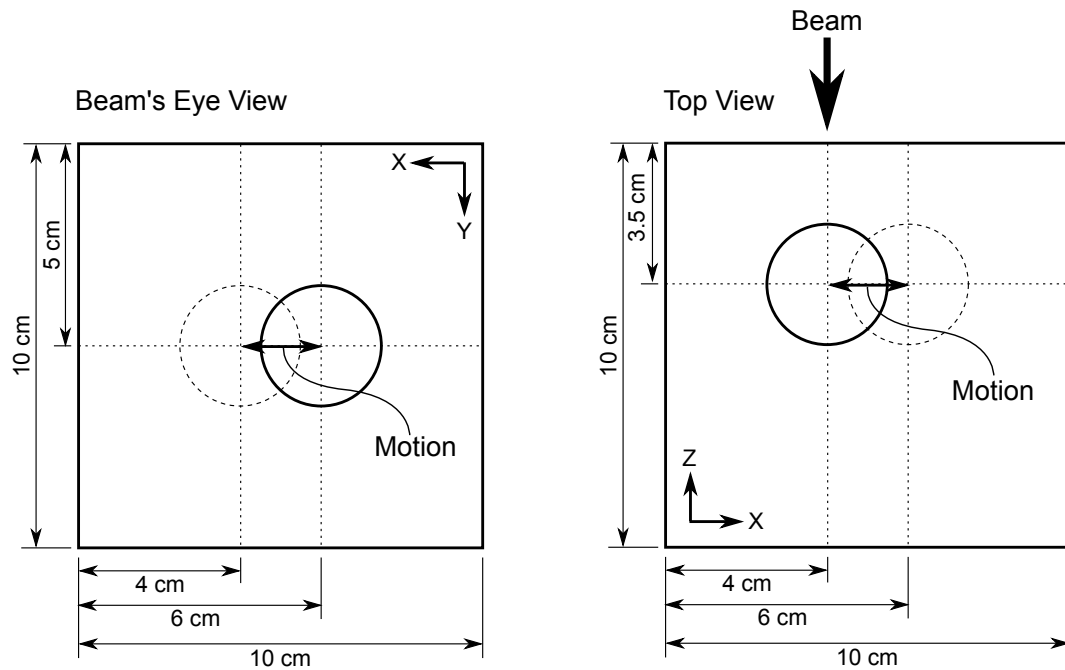
Figure 3.1: Schematic drawing of Phantom 1. A 3-cm spherical target (black circle) moves sinusoidally along the x-axis ($A_x = 2$ cm) with no change in depth in a uniform water phantom.
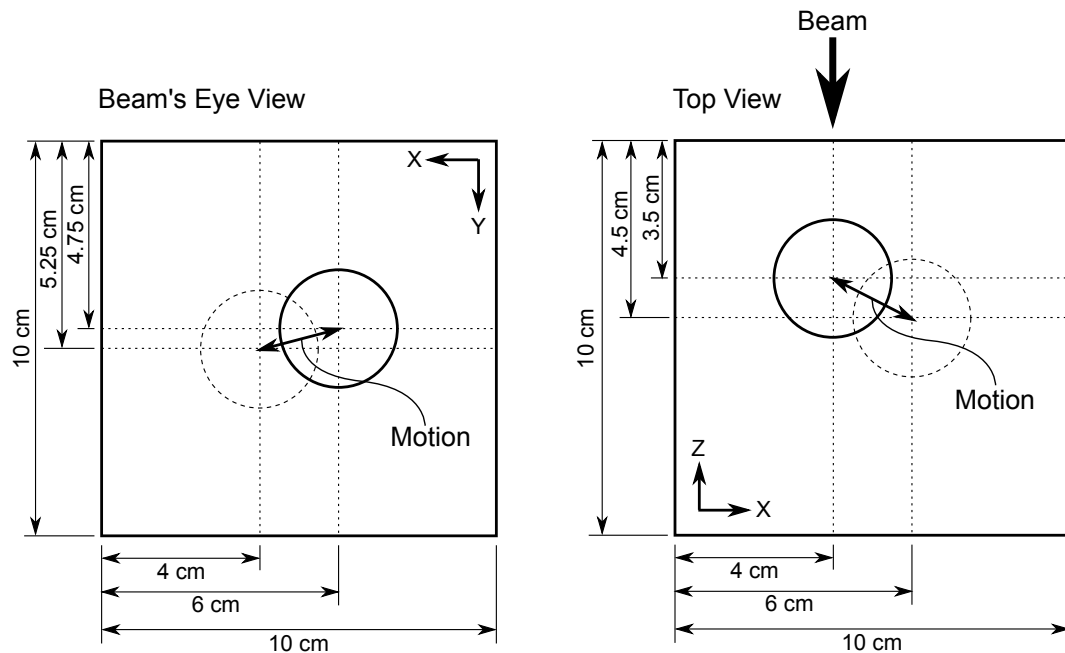
Figure 3.2: Schematic drawing of Phantom 2. A 3-cm spherical target (black circle) moves sinusoidally in 3D ($A_x = 2$ cm, $A_y = 0.5$ cm, $A_z = 1$ cm,) with 1-cm change in depth in a uniform water phantom.
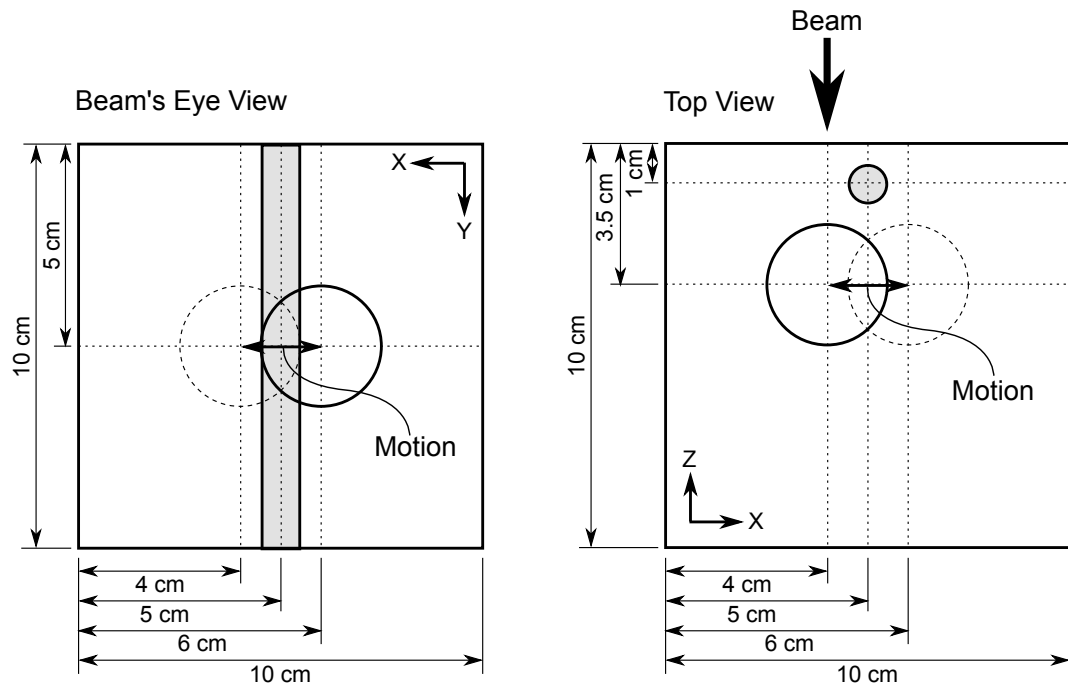
Figure 3.3: Schematic drawing of Phantoms 3 and 4. A 3-cm spherical target (black circle) moves sinusoidally along the x-axis ($A_x = 2$ cm) in a water phantom. A heterogeneity (grey shaded area) is modeled upstream of the target as a cylinder (1-cm diameter, 10-cm length) parallel to the y-axis. For Phantom #3, the cylinder has uniform Hounsfield value of 750, to approximate a rib. For Phantom #4, the cylinder has uniform Hounsfield value of -1000, to represent an air cavity.

corresponding to their unique geometry and motion characteristics.

Treatment Planning for Scanned Carbon Ion Beam Tracking

Treatment planning and 4D dose calculation for scanned carbon ion beam tracking was performed using the TRiP4D research TPS code (Richter *et al.*, 2013) as follows.

(1) 3DCT and 3D target contours for a reference motion state were loaded into the TPS.

(2) A 3D scanned carbon field was planned to irradiate the target in the reference motion state.

- A focal spot size of approximately 6.5 mm, full-width at half-maximum (FWHM), was planned for each pencil beam. In our study, the *focal spot size* was defined as the lateral beam width in air of a single pencil beam at the isocenter of the treatment room, *i.e.*, a reference coordinate near the middle of the patient treatment couch.

- Pencil beam Bragg peaks were regularly spaced on a 2-mm Cartesian grid within each isoenergy layer.

- Pencil beam energies were selected to provide a 3-mm water-equivalent depth spacing between isoenergy layers, and a 3-mm ripple filter (Weber and Kraft, 1999) was used to blur the carbon Bragg peaks in the depth direction.

- A radial target margin of 1.1× FWHM, *i.e.*, perpendicular to the beam central axis, was used to ensure sufficient lateral-scatter-equilibrium to achieve target dose coverage at the off-axis target boundary.

- A distal target margin of 4-mm water-equivalent was used to achieve target dose coverage at the distal target boundary.

(3) The numbers of carbon ions in each beam spot were optimized to achieve uniform target dose for the 3D static case in the reference motion state.

(4) 4DCT and 4D image registration vectors were loaded into the TPS.

(5) Beam tracking offsets were calculated for each pencil beam for each motion state so that each pencil beam Bragg peak would remain in the same local anatomic subvolume of the target for all motion states (see Figure 3.4).

- Lateral tracking offsets, *i.e.*, x- and y-offsets in the beam coordinate system, were calculated by projecting the 4D image registration vectors onto an xy-plane perpendicular to the beam central axis (z).

51
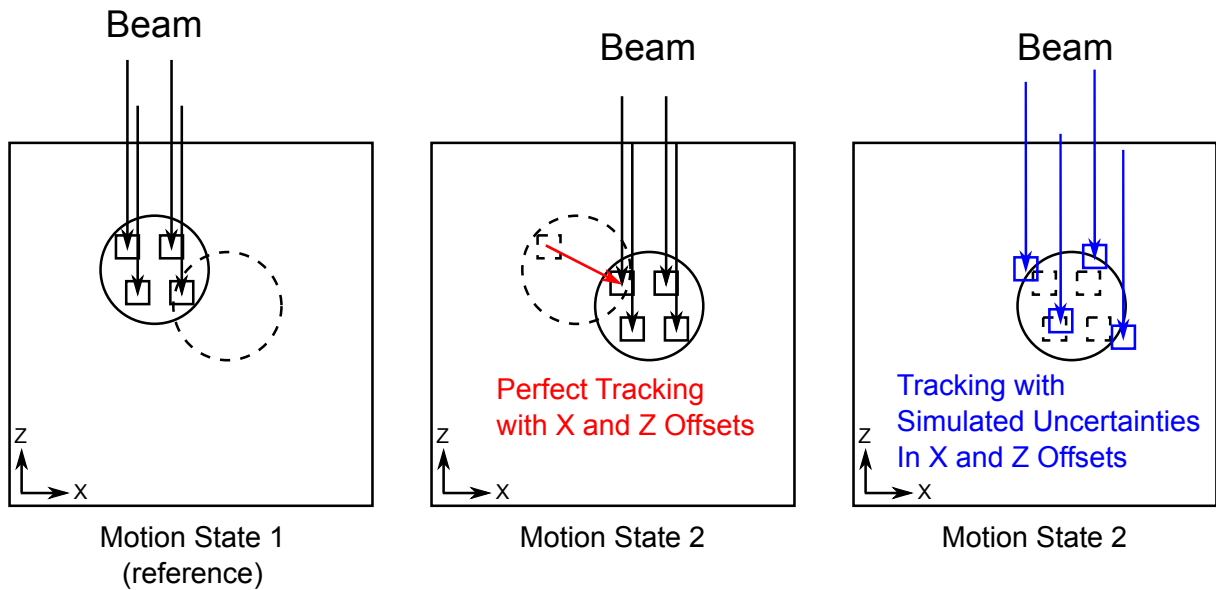
Figure 3.4: Diagram of perfect beam tracking and beam tracking with simulated motion uncertainties. For perfect tracking, a set of ion pencil beams (arrows) are distributed throughout a target volume (circle) in the reference Motion State 1 (left) with individual Bragg peaks located in subvolumes of the target (small squares). After the target moves to Motion State 2 (middle), each pencil beam also moves to track the subvolumes. To simulate the effect of motion uncertainties, we offset individual pencil beam positions (right). The offset pencil beams (right) are shown to irradiate new subvolumes (small squares) that partially or fully miss their planned subvolumes in the target (dashed small squares), usually leading to deterioration of the planned target dose coverage.

- Range-tracking offsets, *i.e.*, z-offsets, were calculated to compensate changes in the radiological depth of the target at points coinciding with the Bragg peak position for each pencil beam. First, 4D image-registration vectors were used to map the movement of a subvolume in the target (*e.g.*, a single voxel containing a pencil beam Bragg peak) from its position in the reference motion state to its position for all other motion states. Second, the radiological depth of that (moving) subvolume was calculated uniquely for each motion state using an existing ray-tracing algorithm in TRiP4D and using the appropriate 3DCT subset of the 4DCT. Finally, a range tracking offset was calculated based on the change in radiological depth of the subvolume (containing the Bragg peak coordinate) for all motion states.

(6) Idealized patient respiratory motion signals, *i.e.*, with constant respiratory period, were loaded into the TPS. These motion signals were used to simulate those that would be monitored in real-time during treatment delivery, for example using a respirometer.

(7) Beam-tracking 4D delivery was simulated.

- Based on the patient respiratory motion signal (*e.g.*, period and starting phase), the required particles per pencil beam, and the availability of particles from the accelerator spill sequence, temporal characteristics of 4D delivery were simulated by binning each pencil beam into the motion state in which it would most likely be irradiated (Richter *et al.*, 2013).

- The corresponding tracking offsets (from Step 5) were added to each pencil beam Bragg peak coordinate depending on the motion state into which it was binned.

- Using new TPS codes developed in this work, *errors* were added to the x, y, and z components of each tracking offset to simulate the effect of motion uncertainties, described in further detail in the next section.

(8) Finally, 4D dose was calculated by accumulating dose to voxels from all pencil beams for all discrete motion states (Richter *et al.*, 2013). Coordinates of the target voxels were transformed for each motion state using the image registration vectors to allow summation of 4D dose to the moving voxels.

For perfect tracking, we simulated 18 motion scenarios for each phantom with variation in motion trace signals with period, $\tau = 3$, 4, and 5 s, and starting respiratory phase at beginning of irradiation, $\phi = 0$, 60, 120, 180, 240, and 300 degrees. Our rationale for

these multiple motion scenarios was that, even when pencil beams perfectly track target motion and depth changes, some deviations in off-axis dose contributions for individual pencil beams are expected (van de Water *et al.*, 2009). By sampling these 18 scenarios of motion, we avoided the chance that our findings would be confounded by a single "lucky" or "unlucky" choice of τ or ϕ.

Simulation of Motion Uncertainties and Beam Tracking Uncertainties

We modeled both systematic and random positional uncertainties as well as temporal lags during beam tracking therapy. Ultimately, uncertainties were simulated by shifting pencil beam coordinates and modifying target motion signals prior to 4D dose calculation as illustrated in Figure 3.4. For each individual uncertainty modeled, we also included 18 motion scenarios of respiration with variable period and starting phase as described for the perfect tracking case above. A list of modeled uncertainties and a brief description of our rationale and implementation in our TCS is given below.

(A) Phase Delays in Beam Tracking

- *Rationale:* Delays in applying the correct tracking offset to individual pencil beams for given motion states might be caused either by delays in the motion state detection system or by delays in the beam tracking control system or beam delivery system.

- *Implementation:* Delays were simulated by loading both an internal motion signal (*i.e.*, representing the "true" tumor motion) and an external motion signal (*e.g.*, that could represent motion of an external surrogate marker) into the TPS (Richter *et al.*, 2013). The internal motion signal was used to synchronize the temporal delivery of pencil beams to their appropriate 4DCT motion state for 4D dose calculation (see Step 7 above), but the external motion signal was used to determine a given beam tracking offset. By delaying the external motion signal, we caused tracking offsets to be applied from an incorrect motion state, depending on the amount of delay.

- *Variables Simulated:* Phase delays of 0, 5, 10, and 15 degrees were simulated.

(B) Random Errors in Pencil Beam Coordinates

- *Rationale:* Random errors in pencil beam coordinates during beam tracking might be caused by limited precision of the beam tracking system, *i.e.*, scanner magnets and range-tracking wedge.

- *Implementation:* Random errors were sampled from Gaussian distribution with a user specified width σ using a random number generator and added to pencil beam tracking offsets prior to 4D dose calculation.

- *Variables Simulated:* We applied 1D random errors independently to x, y, and z with σ of 0, 0.5, 1.0, and 1.5 mm. We also applied combined 3D random errors to x, y, and z with σ values of 0, 0.5, 1.0, and 1.5 mm.

(C) Systematic Errors in Pencil Beam Coordinates

- *Rationale:* Systematic errors in pencil beam coordinates during beam tracking therapy might be caused by misalignment of the patient, patient shifting after setup, or by weight loss of the patient.

- *Implementation:* Systematic errors were added to pencil beam tracking offsets prior to 4D dose calculation.

- *Variables Simulated:* We applied 1D errors of 0, 1, 2, 3, and 4 mm independently to x, y, and z pencil beam coordinates. We also applied combined 3D errors of 0, 1, 2, 3, and 4 mm simultaneously to x, y, and z pencil beam coordinates.

(D) Limited Acceleration of Range-tracking Wedge System

- *Rationale:* When a motion state change occurs or a new pencil beam begins irradiation, a new range-tracking offset must be applied. The tracking system at GSI uses a passive acrylic wedge system mounted on linear drive motors that move material in or out of the beam path. This motorized system has a finite acceleration of 8 g (1 g = 9.81 m/s^2), *i.e.*, in water-equivalent range changes, (Saito *et al.*, 2009) that delays immediate application of the range-tracking offset.

- *Implementation:* We implemented equations for 1D motion of the range-tracking wedge under the influence of constant acceleration, constant deceleration, or no acceleration into our TPS. When a new tracking range-offset was requested during treatment simulation, *e.g.*, when a new pencil beam started irradiation or a motion state change occurred, we considered the current position and velocity of the range-tracking wedge and simulated its trajectory that would allow it to most quickly reach and stop at the desired new position. From this trajectory we determined the mean wedge-position for each pencil beam for each motion state and used that mean position as the range-tracking offset for our simulations.

- *Variables Simulated:* We simulated range-tracking wedge acceleration values of 0.001, 0.01, 0.1, 1, 8, 10, and 100 g and a hypothetical wedge with infinite

acceleration. The infinite acceleration wedge was used for our reference case simulations. Acceleration was defined along the beam central axis (z) in terms of changing water-equivalent thickness of the acrylic wedge in the beam path.

Analysis of Computed Dose Distributions

In order to analyze the large number of simulations performed in our robustness study for scanned carbon beam tracking, we wrote Linux scripts to extract dose-volume statistics from each treatment simulation record and to automatically plot these dose-volume statistics. All 4D dose distributions were transformed to a reference 3D motion state for analysis. For each phantom and each variable studied, we combined the target dose distributions for the 18 scenarios of possible respiratory patterns. From these combined distributions, we prepared box-whisker plots to allow easy visualization of the entire range of target dose distribution expected for a single modeled uncertainty. We also determined the volume of the target receiving at least 95% of the prescribed dose (V_{95}), the volume of target receiving greater than 107% of the prescribed dose (V_{107}), and $D_5 - D_{95}$, the difference between the highest dose in the target, after excluding 5% of the target volume receiving the very highest dose, and the lowest dose in the target, after excluding 5% of the target volume receiving the very lowest dose. V_{95} was used to quantify target dose coverage, V_{107} was used to quantify target overdosage, and $D_5 - D_{95}$ was used to quantify target dose homogeneity. For select cases, we plotted 2D cuts from the dose distributions as colorwash overlaying the phantom and target contours.

3.2.2 Robustness of Beam Tracking to Simulated Motion Uncertainties for 1 Lung Patient

We simulated the impact of motion uncertainties on target dose coverage for Lung Patient #1, who had a peak-to-peak tumor motion amplitude of 25 mm, as discussed in Section 2.2.3. For this lung cancer patient, treatment planning for scanned carbon beam tracking was similar to that described for the water phantoms in Section 3.2.1, with the following differences. Instead of 1 field, we used the 4-field irradiation protocol developed at NIRS for hypofractionated lung cancer therapy with carbon beams (Miyamoto *et al.*, 2007). We used gantry angles of +20, -20, -70, and -110 degrees that corresponded to the angles used at NIRS. For reference, in TRiP4D, 0 degrees represents a lateral beam and -90 degrees represents an AP beam. The couch angle was -90 degrees, hence all beams fell in an axial plane. We used the Local Effect Model Version IV at GSI (Scholz *et al.*, 1997; Elsässer *et al.*, 2010) along with TRiP4D to optimize and calculate RBE-weighted

carbon dose distributions, *i.e.*, with the biological endpoint of lung tumor control. We used an α/β ratio of 6 Gy for lung tumor control ($\alpha = 0.021$ Gy^{-1}, $\beta = 0.0035$ Gy^{-2}, $D_T = 10$ Gy) (Lüchtenborg, 2011). We planned 8.2 Gy (RBE) for each of the 4 fields for a total dose of 32.8 Gy (RBE) to the target. We used a combination of both rigid image registration vectors and deformable image registration vectors to plan beam tracking offsets and to calculate 4D accumulated dose, respectively. Lüchtenborg (2011) demonstrated that keeping a rigid spacing between neighboring pencil beams can provide a more homogeneous target dose for beam tracking, since a deforming grid can lead to bunching and dispersion of pencil beams that causes local overdosing and underdosing within the target, respectively. Thus, we used rigid vectors to plan beam tracking offsets, but we used deformable image registration vectors in the 4D dose calculations. For calculation of rigid image registration vectors, we only considered motion of tissue within the CTV boundary. For calculation of deformable image registration vectors, we used the entire 4DCT data set.

For Lung Patient #1, motion uncertainties and beam tracking uncertainties were simulated identical to those described for the water phantom studies in Section 3.2.1. Analysis of target dose distributions was similar to that described for the water phantoms. In all cases, the 4D dose distributions from the combined 4 fields were transformed to a 3D reference motion state at end-exhale for analysis. In addition, we also plotted the full distribution of beam tracking offsets required for each pencil beam and each motion state.

3.2.3 Robustness of Beam Tracking to Interfractional Changes in Organ Motion for 6 Lung Cancer Patients

Rationale

One serious criticism of scanned ion beam tracking is that the approach currently assumes true periodic organ motion and that there exists a fixed correlation between the patient respiratory phase and the motion of internal anatomy. For example, if only external motion surrogates, such as markers fixed to the sternum, were monitored during treatment delivery, an internal motion deviation might be missed. If drifts in absolute tissue position would occur, *e.g.*, due to muscle relaxation over the course of several minutes, then respiratory phase alone may not accurately be used to predict the position of internal organs. In addition, weight loss of the patient during a course of treatment likely leads to changes in the range of ion pencil beams in tissue. Therefore, we sought to better understand the dosimetric consequences of relying on these assumptions by simulating scanned carbon beam tracking treatment using an initial 4DCT for treatment planning and then using a multiple-week series of 4DCT images, acquired for the same set of patients, to simulate

treatment and delivery of 4D dose distributions to the patients at later time points.

Patient Sample

To study the effects of interfractional changes in organ motion on target dose coverage for scanned carbon beam tracking, we selected 6 lung cancer patients who were previously enrolled in a research study at UTMDACC and had undergone multi-week serial 4DCT imaging. These patients received a 4DCT imaging sequence each week following the methods of Pan *et al.* (2004), with images binned into 10 phases of their respiratory cycle. Our approach was to prepare a scanned carbon ion beam tracking treatment plan using the first 4DCT image set and, then, to simulate treatment delivery using the later 4DCT image sets.

Treatment Planning and Simulation on Multi-week 4DCTs

We used the software program Plastimatch (Shackleford *et al.*, 2010) to calculate deformable image registration vectors for each patient for each 4DCT image series to use in 4D dose calculation. We calculated rigid image registration for all phases of the first 4DCT set to plan beam tracking offsets as described in Section 3.2.2. In addition, we rigidly registered the patient position at a reference state of end-exhale throughout all weeks of 4DCT images. From this, we rigidly offset the CT voxel coordinates when simulating treatment on later week 4DCTs. This concept is similar to aligning the patient before each treatment, *e.g.*, using an onboard imaging device such as orthogonal x-ray planar images or cone-beam CT images. Treatment plans were prepared as described in Sections 3.2.1 and 3.2.2, again using 4 fields and 32.8 Gy (RBE) total dose. For patients with targets in the right lung, the couch angle was changed from -90 to 90 degrees. For calculation of dose on later 4DCTs, the correct 4DCT and corresponding deformable image registration vector map was loaded into the TPS just before calculating 4D dose. For 6 patients, we calculated dose on 3 4DCTs, *i.e.*, week 0, 1, and 2. For Lung Patient #1, we also used a second 4DCT scan from week 0 to investigate interfractional motion changes that might occur during a single day, however, this data was not available for the other 5 patients in our study. For each treatment simulation, we used 18 different respiratory motion signals with variable period and starting phase as described in Section 3.2.1.

Analysis of Computed Dose Distributions

Analysis of target dose distributions was similar to that described for the water phantoms. In all cases, the 4D dose distributions from the combined 4 fields were transformed to a 3D reference motion state at end-exhale for analysis.

3.3 Results

Target dose coverage for scanned carbon ion beam tracking was found to be sensitive to a number of independently varying errors in beam tracking. As expected, robustness of target dose coverage to these errors in beam tracking was generally poorer when heterogeneities were present near the target. However, robustness was generally better for patient plans, where we used 4 equal-weight beams, compared to the mathematical phantom plans with simulated heterogeneities, where we used only a single beam. Overall, target dose was found to be most sensitive to phase delays in beam tracking, systematic spatial errors in tracking, and interfractional changes in organ motion. Limited acceleration of the range-tracking wedge was found to have a moderate impact on target dose coverage, particularly for the lung patient. Random errors in beam tracking were found to have minimal impact on target dose coverage.

In the following sections, we present our dose calculations for scanned carbon ion beam tracking for each modeled error in beam tracking. First, we present dose-colorwash plots to illustrate our treatment plans for perfect tracking scenarios. Then, we present dose-volume statistics for the moving targets for all cases of simulated errors in beam tracking. We also present tables to summarize the robustness of V_{95}, our main metric for target coverage, as a function of the simulated errors in beam tracking. Finally, we present the robustness of target dose coverage to interfractional changes in organ motion for 6 lung cancer patients.

3.3.1 Robustness of Beam Tracking to Motion Uncertainties for 4 Phantoms

Target Dose Distributions for Perfect Tracking

For our simulations of perfect beam tracking (for the motion scenario with $\tau = 4$ s and $\phi = 0$ degrees), we found a highly uniform and nearly identical target dose for Phantoms #1 and #2 with mean target doses of 100 ± 1 %, *i.e.*, percent of the prescribed target dose, for both phantoms. However, we found slightly non-uniform target dose for Phantoms #3 and #4, which both had a cylindrical heterogeneity upstream of the moving target, with mean target doses of 100 ± 3 % and 99 ± 5 %, respectively. Dose distributions are shown as 2D colorwash cuts in the XZ plane in Figure 3.5 for perfect tracking. Dose-volume statistics for perfect tracking are shown in Figure 3.6, at points where the phase delay is 0 degrees (*i.e.*, no delay). We observed that the target dose coverage for perfect tracking for Phantoms #1 and #2 was not affected by respiratory period or starting phase, and all 18 data points (for the 18 scenarios of respiratory motion with variable period (τ) and starting phase (ϕ)) overlay exactly. However, for Phantoms #3 and #4, we observed differences
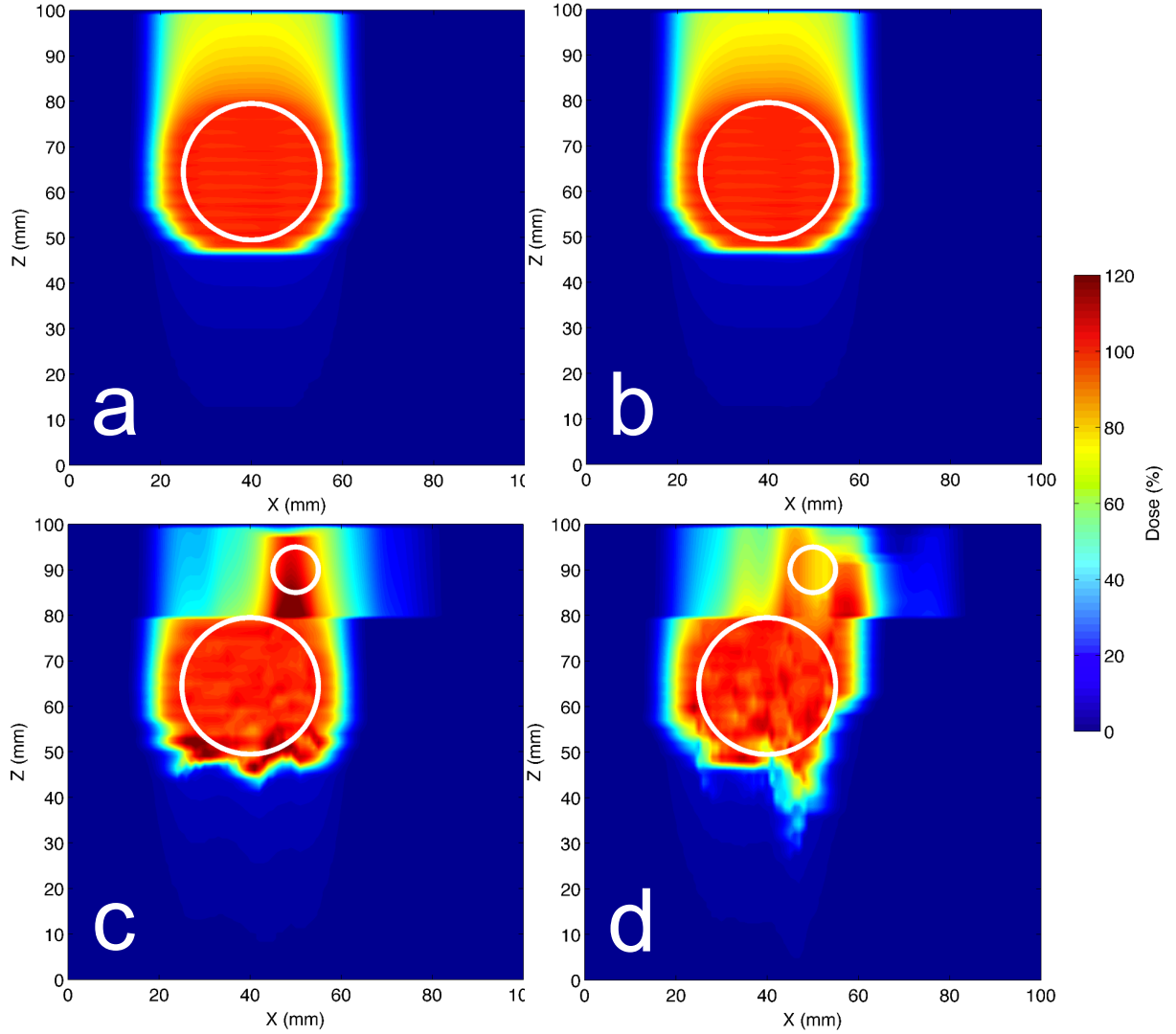
Figure 3.5: Perfect beam tracking dose distributions in XZ plane shown for a reference scenario ($\tau = 4$ s and $\phi = 0$ degrees) for Phantom #1 (a), Phantom #2 (b), Phantom #3 (c), and Phantom #4 (d). Target indicated by large white circle. Beam direction was $-z$. For Phantoms #3 and #4, a proximal slab (z in 80-100 mm) did not move and contained the rib cylinder and air cylinder heterogeneities, respectively, indicated by the small white circles. Irregular dose distributions are seen in the target for Phantoms #3 and #4 even for perfect tracking.
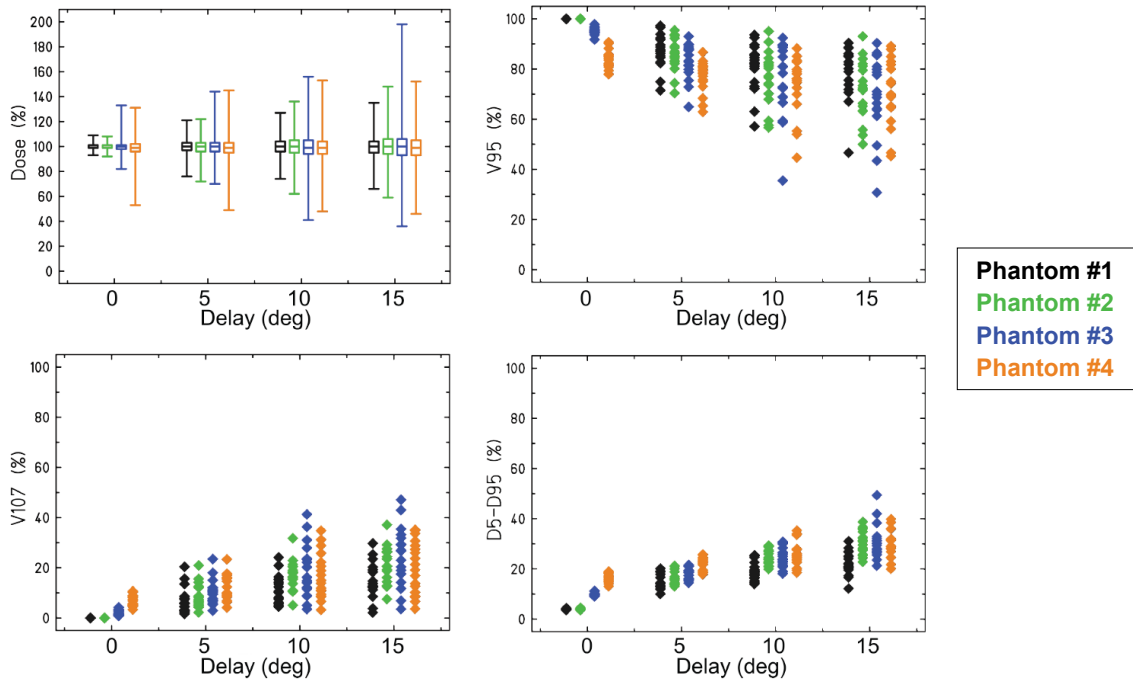
Figure 3.6: Robustness of target dose coverage to phase delays in tracking shown for the 4 phantoms. Each box-whisker plot (top left) summarizes the minimum, first quartile, median, third quartile, and maximum target dose (values are percent of prescribed dose) over all 18 scenarios of motion (with variable period τ and starting phase ϕ) for each value of phase delay. Dose-volume statistics for each of the 18 individual motion scenarios are shown by the markers for V_{95}, V_{107}, and $D_5 - D_{95}$ for each value of phase delay. Dose and volume values are reported as percent of prescribed target dose and percent of total target volume, respectively. Markers are offset slightly to ease viewing. For all phantoms, target dose coverage (V_{95}) degrades rapidly with increasing phase delays in beam tracking.

in target dose coverage for those 18 scenarios depending on the respiratory period and respiratory starting phase. Thus, even for perfect tracking, target dose coverage was found to be degraded by heterogeneous tissue upstream of the moving target.

Phase Delays in Beam Tracking

The robustness of target dose coverage to simulated phase delays in beam tracking is shown in Figure 3.6. A rapid degradation of target dose coverage (V_{95}) with increasing phase delay is seen for all 4 phantoms. For an example, if the respiratory period were 4 s, these phase delays of 5, 10, and 15 degrees would correspond to temporal delays of 56, 111, and 167 ms, respectively. Such phase delays in beam tracking could potentially arise either in real-time detection of a patients current motion state or in real-time application of tracking offsets with the beam delivery system.

Random Errors in Beam Tracking

The impact of random spatial errors in beam tracking on target dose coverage was found to be minimal (V_{95} changed less than 1%) when errors were sampled from Gaussian distributions with $\sigma \leq 0.5$ mm (cf. Table 3.1). Furthermore, only slight degradation of target dose coverage was seen with random errors sampled with σ values up to 1.5 mm. For reference, the precision in lateral x and y pencil beam spot position for beam tracking, as determined by the dipole scanning magnets and position feedback system, is approximately 0.16 mm for the GSI carbon ion synchrotron, and the precision in the z range-tracking offsets, determined by the water-equivalent pathlength through the range-tracking wedge system, is approximately 0.25 mm (Saito *et al.*, 2009). Plots of the robustness of target dose coverage to random errors in beam tracking for the phantoms are included in Appendix A.

Systematic Errors in Beam Tracking

Target dose coverage was found to be highly sensitive to systematic spatial errors in beam tracking. Errors up to 4 mm led to an approximately 21% drop in target coverage V_{95}, averaged over all phantoms. Figure 3.7 shows the robustness of target dose coverage to combined systematic errors in tracking x-, y-, and z-coordinates. Results for *individual* systematic errors in tracking x-, y-, and z-coordinates are included in Appendix A. For Phantoms #1 and #2, minimal effect on target dose was seen until the errors were greater than 2 mm, with visible drops in coverage with errors of 3 and 4 mm, likely caused when the scanned ion field edge moves very close to the target boundary. In contrast, for Phantoms #3 and #4, loss of target dose coverage is seen even for 1 mm systematic errors and increases

Table 3.1: Robustness of target dose coverage to tracking errors for 4 phantoms. $\bar{V}_{95}$ is the mean V_{95} for 4 phantoms and 18 motion scenarios. Changes in coverage ($\Delta \bar{V}_{95}$) more than 5% indicated in red. Derivative is the change in $\bar{V}_{95}$ per unit error.

Variable (units)	Error Magnitude	$\bar{V}_{95}$ (%)	$\Delta \bar{V}_{95}$ (%)	Derivative (%/unit)
Perfect Tracking	-	94.8	-	-
Phase Delay (degrees)	5.0	83.1	**-11.7**	-2.3
	10.0	76.4	**-18.4**	-1.3
	15.0	72.8	**-22.0**	-0.7
Random X Offset (mm)	0.5	93.9	-0.9	-1.8
	1.0	90.7	-4.1	-6.3
	1.5	86.2	**-8.6**	-9.1
Random Y Offset (mm)	0.5	93.9	-0.8	-1.7
	1.0	90.9	-3.9	-6.1
	1.5	86.5	**-8.2**	-8.7
Random Z Offset (mm)	0.5	95.2	0.5	0.9
	1.0	95.6	0.9	0.8
	1.5	95.7	0.9	0.2
Random XYZ Offset (mm)	0.5	93.3	-1.5	-2.9
	1.0	87.1	**-7.6**	-12.3
	1.5	80.6	**-14.2**	-13.1
Systematic X Offset (mm)	1.0	93.1	-1.6	-1.6
	2.0	90.8	-3.9	-2.3
	3.0	88.0	**-6.8**	-2.9
	4.0	84.3	**-10.4**	-3.6
Systematic Y Offset (mm)	1.0	94.7	0.0	-0.0
	2.0	94.5	-0.2	-0.2
	3.0	93.4	-1.4	-1.1
	4.0	90.9	-3.9	-2.5
Systematic Z Offset (mm)	1.0	94.5	-0.3	-0.3
	2.0	94.0	-0.8	-0.5
	3.0	93.0	-1.7	-0.9
	4.0	91.1	-3.7	-1.9
Systematic XYZ Offset (mm)	1.0	92.7	-2.0	-2.0
	2.0	88.8	**-5.9**	-3.9
	3.0	82.3	**-12.5**	-6.6
	4.0	74.3	**-20.5**	-8.0
Wedge Acceleration (g)	0.001	75.6	**-19.2**	-
	0.01	81.3	**-13.5**	637.8
	0.1	86.0	**-8.8**	52.0
	1	93.1	-1.6	7.9
	8	94.6	-0.2	0.2
	10	94.6	-0.2	0.0
	100	94.7	0.0	0.0
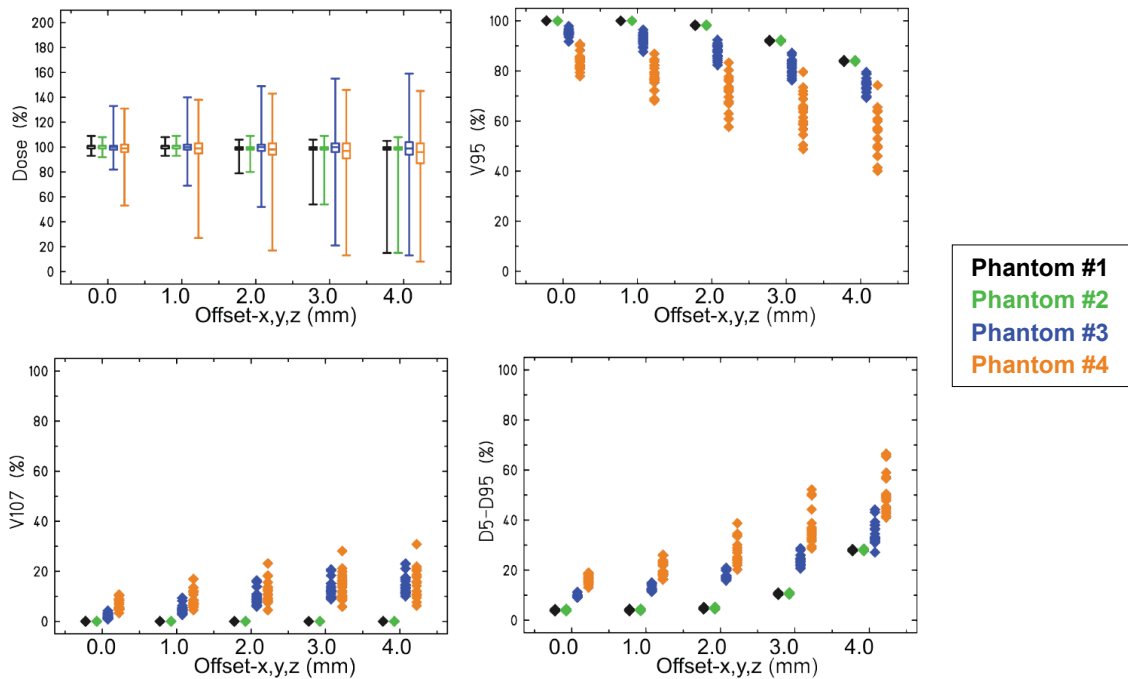
Figure 3.7: Robustness of target dose coverage to systematic errors in tracking x-, y-, and z-coordinates shown for the 4 phantoms. A rapid deterioration of target dose coverage (V_{95}) with increasing offset is seen for Phantom #4 and, to a lesser extent, Phantom #3 even for offsets as little as 1 mm. Phantoms #1 and #2 showed a greater robustness to systematic errors but target dose coverage also degraded with shifts greater than 2 mm.
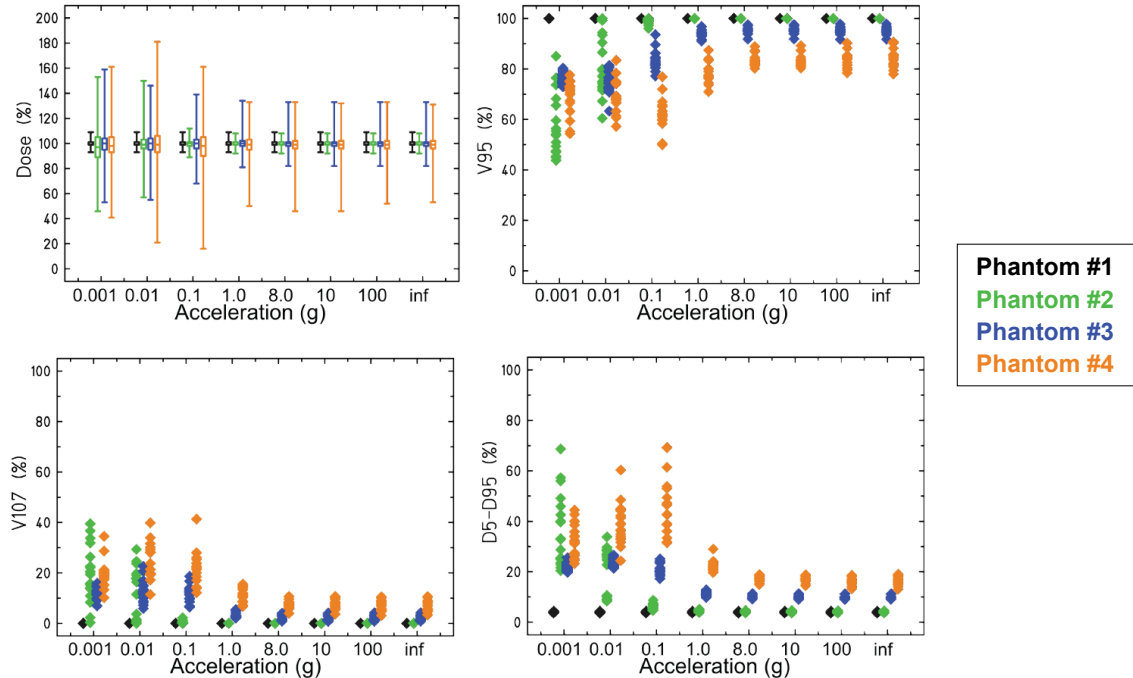
Figure 3.8: Robustness of target dose coverage to to limited acceleration of the range-tracking wedge shown for the 4 phantoms. Note that Phantom #1 (black markers) did not require any range tracking, and, therefore, dose coverage does not depend on range-tracking acceleration. (1 g = 9.81 m/s^2)

with the amount of error. This effect was dominated by x-axis errors in tracking (cf. Table 3.1), since relatively small x-shifts introduced comparably large changes in radiological depth of the target due to the cylindrical heterogeneities present upstream of the target for Phantoms #3 and #4. Therefore, the robustness of beam tracking to systematic errors was poorer when heterogeneities were present.

Limited Acceleration of Range-tracking Wedge

For the 4 phantoms, we found target dose coverage to be mostly insensitive to wedge acceleration for $a \geq 8$ g (1 g $=$ 9.81 m/s^2). However, for acceleration less than 1 g, target dose coverage deteriorated with decreasing acceleration. Note that the direction of acceleration is reported not in the direction of wedge motion but rather in the beam direction, *i.e.*, quantifying the change in water-equivalent pathlength through the acrylic wedge. Figure 3.8 shows the robustness of target dose coverage when we simulated variable acceleration of the range-tracking wedge system. Our reference case of perfect tracking was modeled with infinite wedge acceleration. To put these numbers in perspective, the range tracking wedge system implemented at GSI can modify the beam range with an
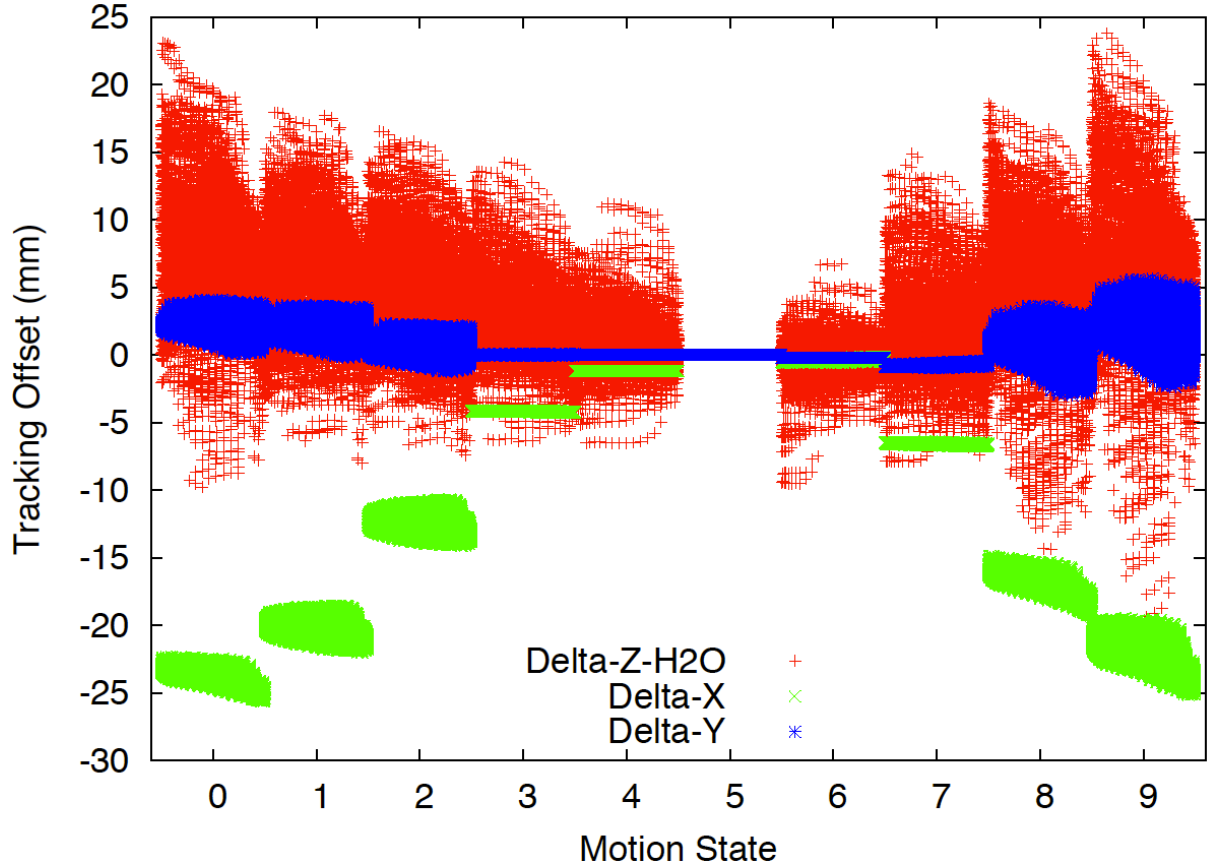
Figure 3.9: Perfect beam tracking offsets for Lung Patient #1 for Field #1. Pencil beam x-offsets (green), y-offsets (blue), and z-offsets (red) are shown for each pencil beam for each motion state. Note the x-offsets of up to approximately 25 mm correspond directly to SI target motion. z-offsets (*i.e.*, range-offsets) exhibit a more complex pattern due to motion of the target in heterogeneous tissue. The reference motion state was 5.

acceleration of approximately 8 g (Saito *et al.*, 2009).

3.3.2 Robustness of Beam Tracking to Simulated Motion Uncertainties for 1 Lung Patient

Example of Beam Tracking Offsets Calculated for Perfect Tracking

The robustness of scanned carbon ion beam tracking to tracking errors in patient cases can be better understood by looking at an exemplary distribution of tracking parameters needed for a lung tumor moving in heterogeneous tissue. Figure 3.9 shows the distribution off beam tracking offsets required for Lung Patient #1 for Field #1 (gantry angle of -20 degrees) for all pencil beams and all motion states for perfect tracking. The x tracking offsets compensated SI motion of up to approximately 25 mm, while y tracking offsets compen-

sated mainly AP motion up to approximately 5 mm. The z offsets compensated changes in radiological depth of the target tissue, requiring up to 25 mm of range-compensation in some motion states, with large variations in range tracking needed for different pencil beams within single motion states. These large fluctuations in range-tracking offset values put high technical demands on the treatment delivery system for patient cases, *e.g.*, when a tumor moves in heterogeneous lung tissue, and are a concerning factor for tracking robustness.

Target Dose Distributions for Perfect Tracking

Our treatment plan for Lung Patient #1 is shown in Figure 3.10 with 2D cuts of 4D RBE-weighted dose overlaying CT images in the reference motion state at end-exhale for perfect beam tracking ($\tau = 4$ s and $\phi = 0$ degrees). We observed a uniform target dose coverage of 32.7±1.1 Gy (RBE) with a rapid falloff of dose outside the target volume. Dose-volume statistics for perfect tracking (for all 18 scenarios of variable respiratory period and starting phase) are shown in Figure 3.11, at points where the phase delay is 0 degrees (*i.e.*, no delay). Similar to Phantom #3 with the rib heterogeneity, some dependence of target dose coverage on respiratory period and starting phase is seen even for perfect tracking, though not as much as that seen for Phantom #4 with the air heterogeneity. These 18 dose distributions provide our baseline estimate of target dose coverage ($\bar{V}_{95} = 95.5\%$) for perfect beam tracking for Lung Patient #1, against which we compare our dose distributions with simulated errors in tracking, discussed in the remainder of this section and summarized in Table 3.2.

Phase Delays in Beam Tracking

Target dose coverage was found to be highly sensitive to phase delays in beam tracking. Figure 3.11 shows the robustness of target dose coverage to simulated phase delays up to 15 degrees, which led to drops in target dose coverage ($\bar{V}_{95}$) up to 18%. These findings were similar to those in our phantom study (cf. Section 3.3.1). Thus, phase delays in tracking were a major detriment to target dose coverage for beam tracking for both phantom and patient cases.

Random Errors in Beam Tracking

The impact of random spatial errors in beam tracking on target dose coverage for the lung patient was found to be minimal ($\bar{V}_{95}$ changed less than 1%) when errors were sampled from Gaussian distributions with $\sigma \leq 1$ mm (cf. Table 3.2). Compared with the
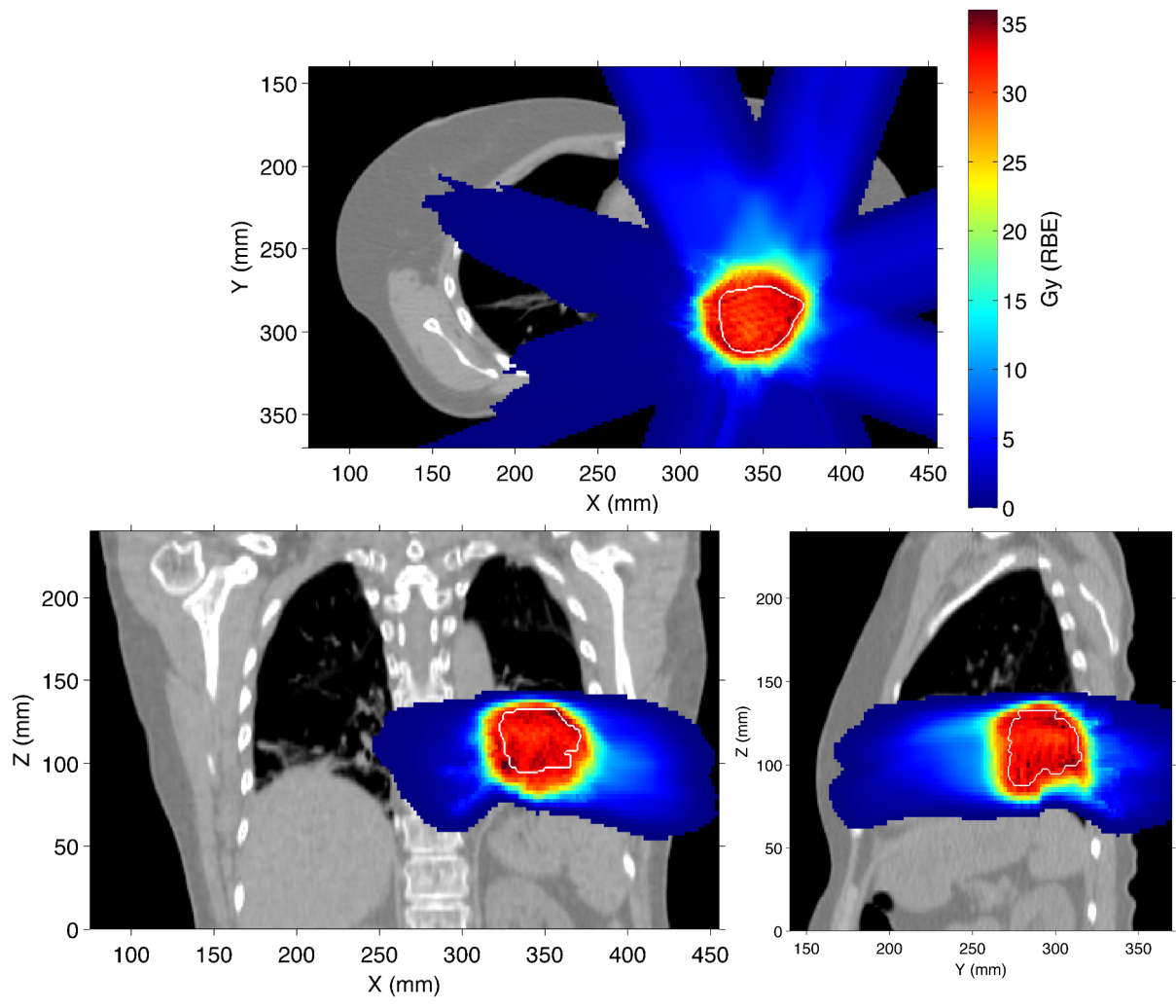
Figure 3.10: 4D RBE-weighted dose distributions overlaying CT images for the reference case of perfect beam tracking for Lung Patient #1 with axial (top), coronal (bottom left), and sagittal (bottom right) views. 4D RBE-weighted dose and CT data are shown in the reference motion state at end-exhale. The CTV boundary is indicated by the white curve. The prescribed target dose was 32.8 Gy (RBE). This plot shows the treatment plan but does not contain information about robustness.
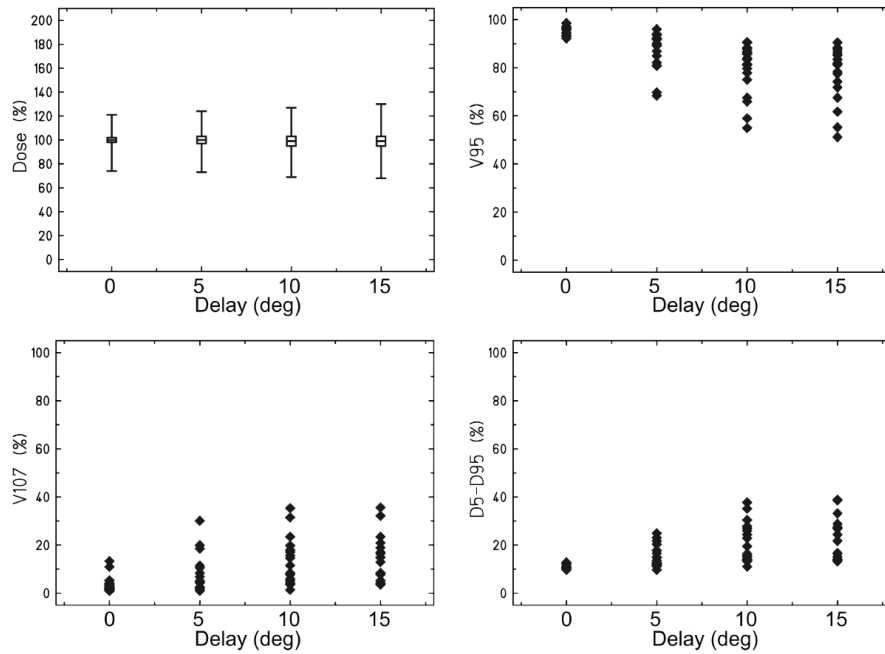
Figure 3.11: Robustness of target dose coverage to phase delays in tracking shown for Lung Patient #1. Target coverage decreases with increasing phase delay, as seen in V_{95} (top right). An increase in overdosed volumes, as quantified by V_{107} (bottom left), might be attributed to interplay effects that occur when lagging pencil beams have incorrect lateral coordinates or incorrect range coordinates.

69

Table 3.2: Robustness of target dose coverage $\bar{V}_{95}$ to tracking errors for Lung Patient #1. $\bar{V}_{95}$ is the mean V_{95} for 4 phantoms and 18 motion scenarios. Changes in coverage ($\Delta\bar{V}_{95}$) more than 5% indicated in red. Derivative is the change in $\bar{V}_{95}$ per unit error.

Variable (units)	Error Magnitude	$\bar{V}_{95}$ (%)	$\Delta\bar{V}_{95}$ (%)	Derivative (% / unit)
Perfect Tracking	-	95.5	-	-
Phase Delay (degrees)	5.0	86.9	**-8.7**	-1.7
	10.0	79.2	**-16.3**	-1.5
	15.0	77.2	**-18.3**	-0.4
Random X Offset (mm)	0.5	95.5	0.0	0.1
	1.0	95.6	0.1	0.0
	1.5	95.4	-0.1	-0.3
Random Y Offset (mm)	0.5	95.4	-0.1	-0.2
	1.0	95.2	-0.3	-0.4
	1.5	94.9	-0.7	-0.8
Random Z Offset (mm)	0.5	95.9	0.3	0.7
	1.0	96.4	0.9	1.0
	1.5	96.6	1.1	0.4
Random XYZ Offset (mm)	0.5	95.8	0.3	0.6
	1.0	96.1	0.6	0.5
	1.5	95.9	0.4	-0.4
Systematic X Offset (mm)	1.0	95.0	-0.5	-0.5
	2.0	94.1	-1.4	-1.0
	3.0	92.5	-3.0	-1.6
	4.0	90.4	**-5.2**	-2.1
Systematic Y Offset (mm)	1.0	95.4	-0.1	-0.1
	2.0	94.9	-0.6	-0.5
	3.0	93.6	-1.9	-1.2
	4.0	91.6	-3.9	-2.0
Systematic Z Offset (mm)	1.0	95.6	0.0	0.1
	2.0	95.2	-0.3	-0.4
	3.0	94.5	-1.0	-0.7
	4.0	93.6	-1.9	-0.9
Systematic XYZ Offset (mm)	1.0	94.9	-0.6	-0.6
	2.0	92.7	-2.8	-2.3
	3.0	87.7	**-7.8**	-5.0
	4.0	79.6	**-15.9**	-8.2
Wedge Acceleration (g)	0.001	79.0	**-16.5**	-
	0.01	79.7	**-15.8**	78.1
	0.1	87.5	**-8.0**	86.3
	1	90.3	**-5.2**	3.1
	8	90.5	-5.0	0.0
	10	90.7	-4.8	0.1
	100	95.2	-0.3	0.0
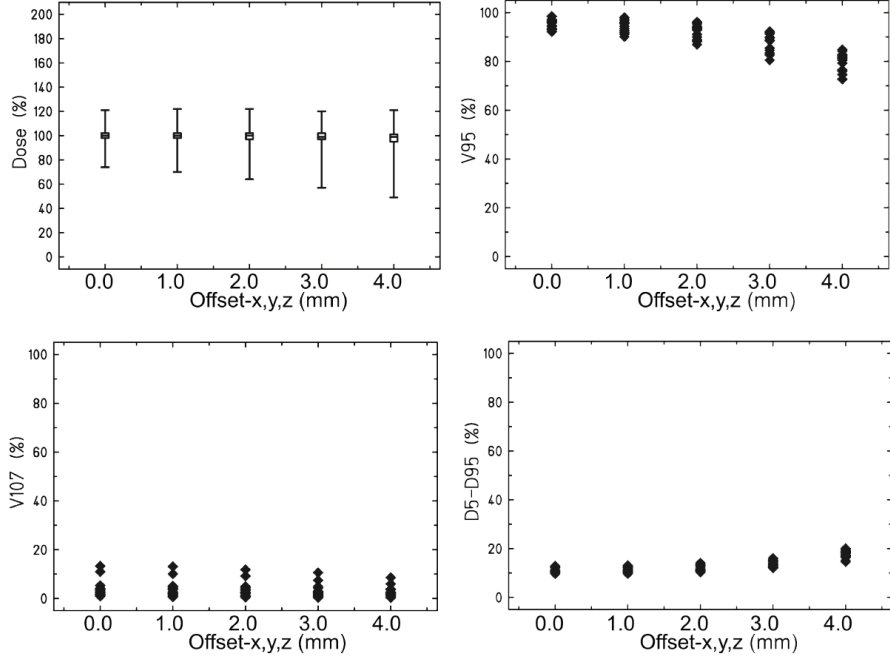
Figure 3.12: Robustness of target dose coverage to systematic errors in tracking x-, y-, and z-coordinates shown for Lung Patient #1. A more dramatic decrease in V_{95} and increase in $D_5 - D_{95}$ is seen, compared to systematic offsets in 1D only (cf. Figures A.12 and A.14).

phantoms, even less effect was seen in Lung Patient #1, likely due to averaging effects for the 4 beams. As discussed in Section 3.3.1, the precision in beam tracking is better than 0.3 mm for the experimental system at GSI. Plots of the robustness of target dose coverage to random errors in beam tracking for the lung patient are included in Appendix A. We determined that random spatial errors in beam tracking had negligible impact on target dose coverage for the precision of our tracking system.

Systematic Errors in Beam Tracking

Target dose coverage was found to be highly sensitive to systematic spatial errors in beam tracking. Errors up to 4 mm led to an approximately 16% drop in target coverage V_{95}, averaged over all phantoms. Figure 3.12 shows the robustness of target dose coverage to combined systematic errors in tracking x-, y-, and z-coordinates. Results for *individual* systematic errors in tracking x-, y-, and z-coordinates are included in Appendix A. Only minimal effect on target dose ($< 3\%$ change in $\bar{V}_{95}$) were seen until the errors were greater than 2 mm, with larger drops in target dose coverage and slight loss of dose homogeneity for errors of 3 and 4 mm, as the scanned ion field edge approaches the target boundary. The drop in target coverage V_{95} due to systematic errors for Lung Patient #1 was less dramatic

71
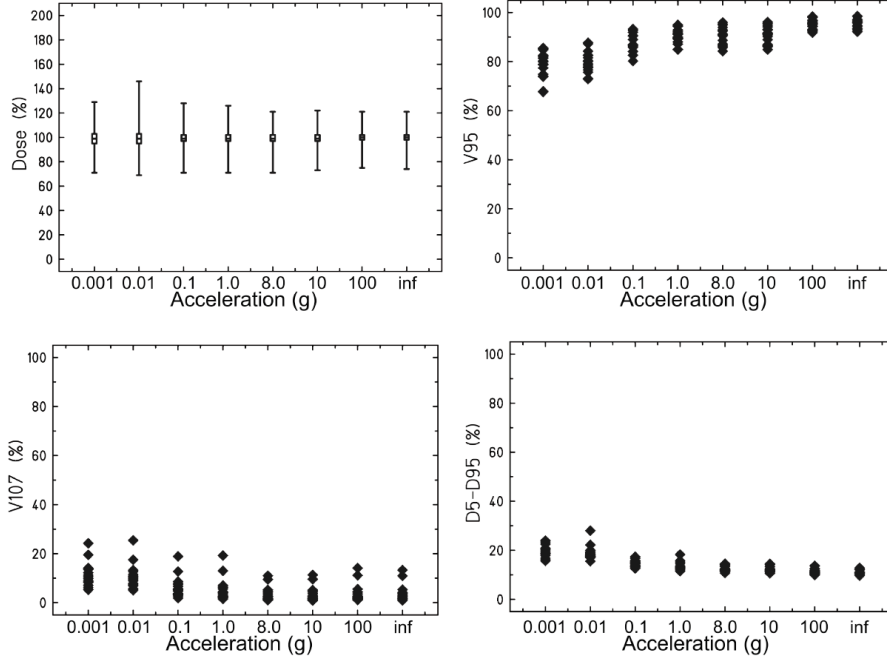
Figure 3.13: Robustness of target dose coverage to limited acceleration (a) of the range-tracking wedge shown for Lung Patient #1. A moderate drop in target dose coverage V_{95} is seen for $a < 100$ g and further worsening is seen for $a < 1$ g.

than for either of the phantoms with heterogeneities (cf. Figure A.5), likely explained by blurring out of dose errors by the 4 fields. Overall, the robustness of beam tracking to systematic errors was better for the patient case compared to the phantoms but still a major concern.

Limited Acceleration of Range-tracking Wedge

For Lung Patient #1, target dose coverage was degraded due to limited acceleration of the range tracking wedge, except for very high wedge acceleration (*e.g.*, $a > 100$ g). Figure 3.13 plots the robustness of target dose coverage to limited acceleration of the range-tracking wedge for the patient. The reference case of perfect tracking was represented by infinite wedge acceleration. Simulation of 100 g wedge acceleration produced nearly identical target dose coverage to that with infinite wedge acceleration. For wedge acceleration of 1 to 10 g, similar target dose coverage V_{95} is seen approximately 5% lower than that seen for perfect tracking (cf. Table 3.2). At wedge accelerations below 1 g, target dose coverage deteriorates even further with decreasing wedge acceleration. The range-tracking wedge system implemented for experiments at GSI has an acceleration of approximately 8 g and, thus, might not achieve desired target dose coverage for lung patients unless further

solutions are devised.

3.3.3 Robustness of Beam Tracking to Interfractional Changes in Organ Motion for 6 Lung Cancer Patients

Target dose coverage was found to deteriorate greatly due to interfractional changes in organ motion 1 and 2 weeks post-planning, as studied for 6 lung cancer patients using multi-week 4DCTs. To give an overview of these patients and the variety of lung tumors studied, Figure 3.14 shows our treatment plans overlaying CT images from the initial planning 4DCT (week 0), *i.e.*, for perfect tracking ($\tau = 4$ s and $\phi = 0$ degrees). Figure 3.15 shows the robustness of target dose coverage to interfractional motion changes for the 6 lung patients. The median target dose remained stable for all patients, within 4 % of the prescribed dose, even up to 2 weeks after planning. However, target dose coverage (V_{95}) deteriorated with time post-planning. For all 6 patients (and for the 18 motion scenarios), $\bar{V}_{95}$ dropped from 94.3% at week 0 to 85.9% and 86.2% for treatment simulated 1 and 2 weeks after planning, a mean decrease in $\bar{V}_{95}$ of 8.4% and 8.1%, respectively. Target dose coverage deteriorated more with time post-planning for Patients #1 and #2, who had the greatest motion amplitudes (up to 25 mm). Overall, target dose coverage (V_{95}) was degraded by interfractional changes in organ motion though median target dose was approximately stable. While this chapter focuses on the robustness of 3D-optimized beam tracking, we also performed similar calculations to those described here to investigate the robustness of *4D-optimized* beam tracking to interfractional changes in organ motion for Lung Patient #1. Those results are included in Table A.1 in Appendix A.

3.3.4 Summary of Results

- For simulations of perfect tracking of moving targets in heterogeneous matter, we found that dose distributions were sensitive to the phase of respiration at the start of irradiation and to the respiratory period. Even when the pencil beam Bragg peaks were directed to perfectly track the moving target, off-axis dose contributions from individual pencil beams were affected by variation in tissue upstream of the moving target and dose was degraded. This finding is in agreement with the findings of van de Water *et al.* (2009).

- Phase delays in tracking the moving targets led to large degradation of target dose coverage. This finding supports the need for predictive algorithms for motion tracking and fast, *i.e.*, few ms, hardware to apply beam tracking parameters in real time during
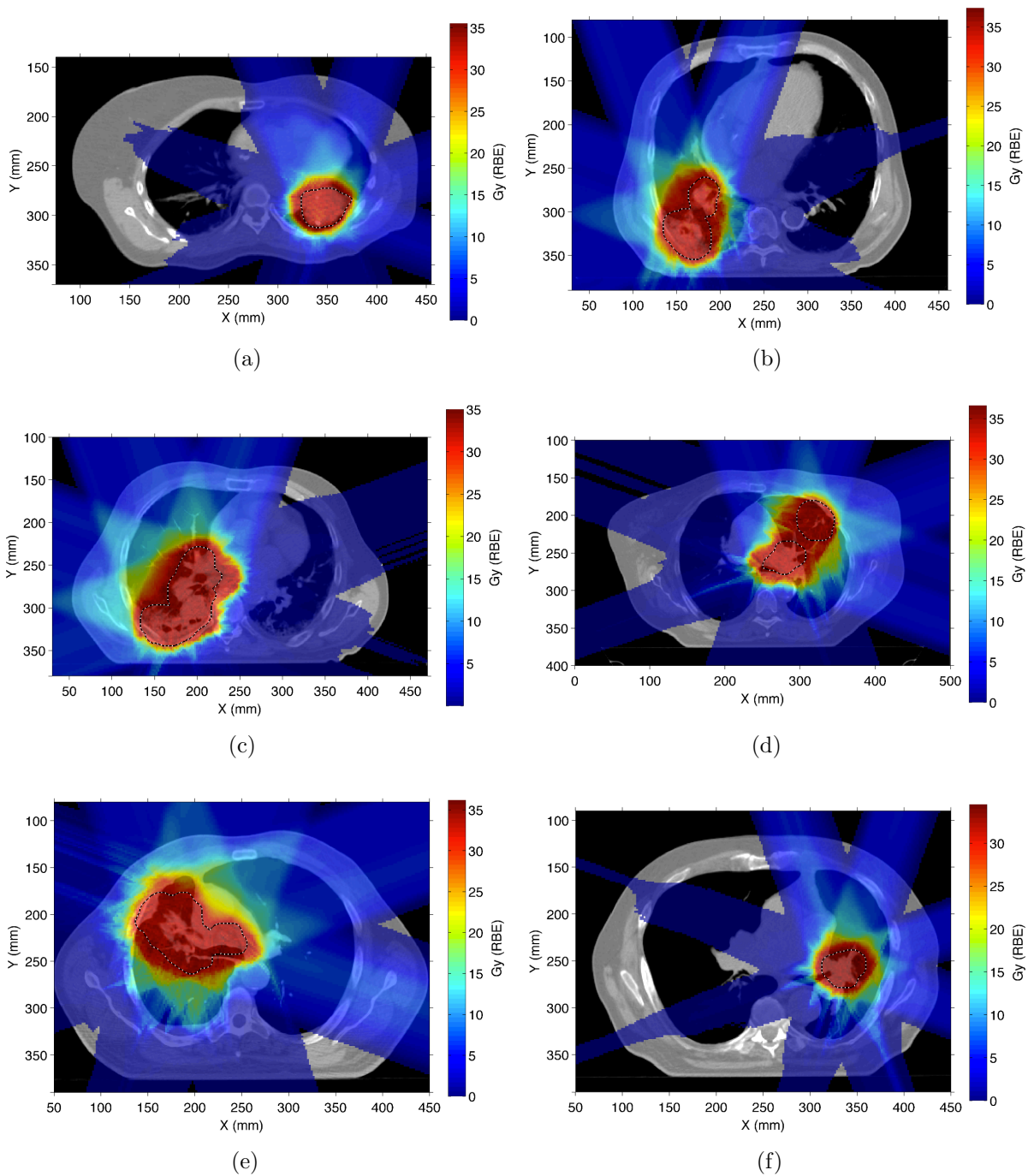
Figure 3.14: Axial view of RBE-weighted dose overlaying CT shown for Lung Patients #1 - #6, indicated by (a) - (f), respectively, for perfect tracking for a reference case with $\tau = 4$ s and $\phi = 0$ degrees. This figure gives a view of our treatment plans and shows the variation in patient anatomy and tumor size for our 6 lung patients.
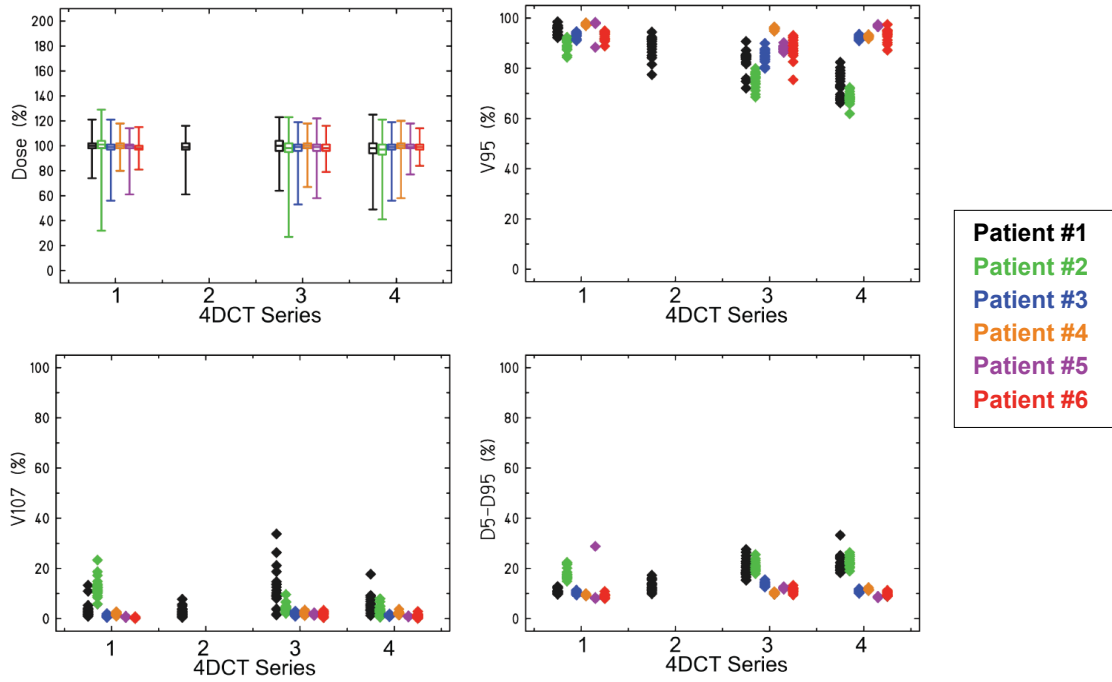
Figure 3.15: Robustness of target dose coverage to interfractional motion changes shown for the 6 lung patients. All treatment plans were prepared for an initial 4DCT Series #1, and dose was also calculated using the later 4DCTs. 4DCT Series #2 was acquired for only Patient #1 on the same day as the initial 4DCT. For all patients, 4DCT Series #3 was acquired 1 week after the initial 4DCT, and 4DCT Series #4 was acquired 2 weeks after the initial 4DCT. Target dose coverage V_{95} deteriorated with time post-planning, dropping approximately 8% after 1 week.

treatment.

- Random tracking errors sampled from a Gaussian distribution with $\sigma < 0.5$ mm had almost no effect on target dose coverage.

- Systematic errors in beam tracking, which could represent patient misalignment, baseline drifts in target position, or errors in image registration used for planning, caused two distinct ill effects on target dose coverage. First, simple misalignment of the target with the radiation field boundary led to underdosage of the target, as the target moved near the dose falloff region. This degradation was observed with errors greater than 2 mm and could likely be addressed simply by using treatment margins, similar to a PTV concept. Second, a more complex relation was seen in heterogeneous tissue, and even relatively small, *e.g.*, 1 mm, errors led to degraded dose, likely since the radiological thickness of tissue upstream of the target can vary greatly off axis. Thus, lateral misalignment of a pencil beam can manifest as an incorrect depth of its Bragg peak in a complex manner.

- The limited acceleration of the range-tracking wedge led to minimal degradation of target dose when acceleration was ≥ 8 g for phantoms. We observed an inflection and rapid worsening of target dose when acceleration was ≤ 1 g. Our patient simulations suggest that a higher wedge acceleration > 10 g might be required to improve target dose coverage, but our data do not suggest the need for acceleration greater than 100 g. If very fast range-tracking is needed in the future, the method of Chaudri *et al.* (2010), which uses magnetic beam deflection and a static wedge degrader, might be preferable to the motorized wedge system used in this study.

- For the 6 lung cancer patients in our study with multi-week 4DCTs, interfractional changes in organ motion did not lead to large changes in the median target dose, *i.e.*, median dose was within 4% of that prescribed, even up to 2 weeks after planning. However, as expected, dose coverage (V_{95}) worsened with time, dropping approximately 8% after 1 week post-planning. Larger degradation of dose coverage was observed for patients with greater tumor motion. For Lung Patient #1, V_{95} dropped approximately 7% due to variation in organ motion occurring during a single day.

3.4 Discussion

In this study, we evaluated the robustness of target dose coverage to motion uncertainties for 3D-optimized scanned carbon ion beam tracking therapy for moving targets. We implemented codes in a research TPS to allow simulation of a number of deviations from perfect tracking. Additionally, we investigated the robustness of beam tracking to interfractional changes in organ motion using multiweek 4DCTs for a sample of lung patients. We found target dose coverage for scanned carbon ion beam tracking therapy to be sensitive to a number of simulated motion uncertainties. Sensitivity was minimal for the lung cancer case against technical uncertainties even though no setup or motion margins were used. Higher sensitivity was seen with respect to changes of anatomy as studied in the multiweek analysis. Our findings can be used to inform the design specifications of future scanned ion beam tracking systems and to inspire future motion mitigation strategies.

One major strength of this work is that this approach gives a view of the motion problem that cannot be explored using commercial treatment planning systems. By the thousands (nearly 4000 dose calculations were reported in this chapter) of 4D dose calculations possible using a research TPS and a research computing cluster, we were able to isolate variables and model the specific impacts of these variables on target dose coverage for patients with moving tumors receiving scanned carbon ion therapy. Another strength is that many of these methods are general and might also be used to simulated the effect of motion uncertainties on dose for other motion mitigation strategies for scanned ion therapy, such as beam gating or rescanning. In this work, we evaluated the robustness of target dose coverage for moving phantoms and lung patients without using setup or motion margins, *i.e.*, no "PTV-type" margins, which could mask underlying changes to the desired dose distribution caused by small errors in beam tracking. This means that our results can be used to understand the baseline robustness of scanned carbon beam tracking and also be used to decide margins and precision requirements that best ensure robustness of target dose coverage for future patient treatments.

Our finding of imperfect target dose coverage even for perfect tracking agreed with that reported by van de Water *et al.* (2009). However, their study did not include patient simulations, whereas we found target dose coverage to be more robust to tracking errors in patient anatomy compared with our mathematical phantoms. These heterogeneous phantoms could be viewed as a worst case example since such cylindrical geometries with discrete edges are rarely found in patients. Since we found target dose coverage to depend on patient starting phase and respiratory period, even for perfect tracking, we expect that rescanning with beam tracking, as suggested by van de Water *et al.* (2009) would likely

provide a more robust dose coverage for targets moving in heterogeneous tissue.

Our study had several limitations. One limitation was that we only investigated robustness to technical uncertainties for one lung patient, who had the highest motion amplitude in our sample of 6 patients. Thus, we might overestimate the sensitivity of target dose coverage to errors in tracking compared to that possible for patients with reduced tumor motion. Another limitation was that we performed 4D dose calculations using a central-axis pencil beam dose algorithm for scanned carbon-ion therapy, which likely introduced systematic errors in our dose distributions when heterogeneities were present near, but off-central-axis, to the ion pencil beams. However, in this study, the speed of the pencil beam dose algorithm allowed us to simulate a much greater number of treatment plans, with varying factors, than would have been possible in a practical timeframe using more accurate dose calculations such as Monte Carlo algorithms. Therefore, we chose speed over accuracy, but we also expect that our findings would not significantly change by using a more accurate dose algorithm. Another limitation was that we optimized the particle fluence for a single reference motion state, *e.g.*, at end-exhale, prior to calculating the beam tracking offsets for each pencil beam for each motion state. That is, we did not account for all motion states in the planning of particle numbers, which partially explains some of our degraded target dose seen even for perfect tracking. These limitations are being addressed in ongoing studies in our laboratory; however, these limitations did not prevent us from achieving our objective, which was to evaluate the robustness of target dose coverage to motion uncertainties for scanned carbon ion beam tracking therapy of moving targets.

Based on our findings, we propose the following future studies. First, we suggest that appropriate beam-specific margins could be designed to mitigate range errors introduced by lateral target misalignment, similar to the approach of Park *et al.* (2012), but also including motion margins needed to cover the deforming tissue during respiration (Graeff *et al.*, 2012). For beam tracking of a deforming target, the ideal field margins could be a "center-of-mass ITV," which covers any range and positional uncertainty for all motion states. Second, optimization could be used to further optimize pencil beam fluence in a way that is optimal for all motion states, which would be beneficial, since, for this 3D-optimized beam tracking approach, it is unknown prior to treatment in which motion state a pencil beam will be irradiated.

Strategies to improve robustness have already been developed for both photon therapy (Bortfeld *et al.*, 2008; Unkelbach *et al.*, 2009) and particle therapy (Unkelbach, 2007; Pflugfelder *et al.*, 2008; Chen *et al.*, 2012; Liu *et al.*, 2012). Many of these strategies incorporated uncertainties in plan optimization to improve probability of tumor control in the presence of patient setup uncertainty, though, to our knowledge, do not yet explicitly

address robustness to organ motion for particle therapy. Theoretically, robust 4D optimization could be used to optimize particle numbers that are both optimal for all motion states and robust to motion uncertainties, likely benefiting patients with thoracic motion receiving scanned ion beam therapy in the near future.

In summary, we developed a new method to model the impact of motion uncertainties for scanned ion beam tracking and implemented our work in a 4D research treatment planning system. We quantified the sensitivity of target dose to several uncertainties present in scanned carbon ion beam tracking for moving tumors using both mathematical phantom studies and retrospective lung cancer patient studies. Our results provide a better understanding of the importance of each of these uncertainties for beam tracking with scanned carbon ions.

Chapter 4

Predicted Risk of Second Cancer Incidence in the Breast for Hodgkin Lymphoma Patients After Carbon Ion Therapy *versus* Proton Therapy

4.1   Introduction

Approximately 9000 men and women will be diagnosed with Hodgkin lymphoma (HL) this year in the USA (*i.e.*, 2013), and nearly 200,000 citizens are currently living with a history of HL (Howlader *et al.*, 2013). Furthermore, HL is one of the most common cancers affecting adolescents and young adults (Bleyer *et al.*, 2006). Patients diagnosed with early stage HL are mainly treated with combined chemotherapy and radiation and can expect survival higher than 90% at 5 years (Armitage, 2010) and 60-80% at 20 years, with survival rates decreasing with age at diagnosis (Bleyer *et al.*, 2006). For this population of patients, side effects of therapy can in some cases be devastating, including second primary cancers, cardiac toxicity, and infertility (Robison *et al.*, 2002). For example, Dores *et al.* (2002) reported a 10.5% absolute excess risk of cancer in the female breast for patients treated with radiation, mainly using photon mantle fields. Due to their long expected survival after therapy, HL patients stand to greatly benefit from new treatment strategies that reduce risks of radiation late effects.

Research in the past decades has focused on reducing radiation dose to healthy tissue and the overall size of therapy fields. Reducing the radiation field size, *e.g.*, using Involved Field Radiation Therapy rather than Extended Field Radiation Therapy, can reduce dose to critical structures near the HL target (Koh *et al.*, 2007). Recently, Chera *et al.* (2009) demonstrated in planning studies that a reduction of dose to the breast, lung, and total

body was possible using proton therapy instead of photon therapy for a sample of HL patients with localized disease above the hilia. Due to the sharper physical dose gradients (Weber and Kraft, 2009) and higher relative biological effectiveness (RBE) (Elsässer *et al.*, 2010), carbon-ion therapy might provide further reductions in dose to normal tissues compared to proton therapy for some HL patients.

Carbon beams provide an increased relative biological effectiveness (RBE) for cell sterilization near their Bragg peak where linear energy transfer (LET) is fairly high, *i.e.*, tens to hundred of keV/μm. Upstream of the Bragg peak, carbon beams have lower LET and thus lower RBE than that found near the Bragg peak. Due to this differential RBE ratio, dose for carbon-ion therapy can be planned to provide equivalent tumor control to proton therapy but with lower physical dose to healthy tissue upstream of the tumor (Schardt *et al.*, 2010; Elsässer *et al.*, 2010). However, despite the reduced physical dose, the biological effectiveness of high LET radiation to induce late effects is much less understood than that of low LET radiation and could increase risks of second cancer after radiotherapy.

In order to estimate risks of secondary malignant neoplasms after exposure to radiation, many studies rely on epidemiological studies of atomic bomb survivors and follow up of cancer survivors exposed to *photon* radiation during the past century. Translation of these data to useful models that can predict risks of second cancer in partially irradiated organs for patients receiving modern radiotherapy is challenging. Most epidemiological data support a linear-no-threshold risk model (NRC, 2006), but Schneider *et al.* (2005), along with others, propose that support for a linear-no-threshold model may be an artifact of the epidemiological studies themselves, which typically only accounted for integral organ doses and thus may have missed any non-linear correlations between point organ doses and second cancer risks. Theoretically, healthy cells, susceptible to neoplastic transformation by radiation, could also be sterilized by radiation, which might lead to a decrease of cancer risk at very high doses. This is not clearly observed in epidemiological data except for the thyroid (NRC, 2006), but it is seen clearly in *in-vivo* experiments, *e.g.*, induction of myeloid leukemia in mice (Coggle, 1988). Recently, Schneider *et al.* (2011) developed a risk model for breast cancer incidence after photon therapy that accounted for the competing processes of radiation breast cell transformation, breast cell inactivation, and cell repopulation during fractionated radiotherapy. Their model parameters were fit to the epidemiological study of breast cancer incidence in HL survivors of Travis *et al.* (2003) and agreed closely with a linear-no-threshold model for atomic bomb survivor data at lower doses but modeled a non-linear decrease in risk at higher doses, *e.g.*, higher than 20 Gy.

In order to apply risk models developed for photon radiation exposures to patients receiving charged particle therapy, a method of calculating RBE for tumor induction by
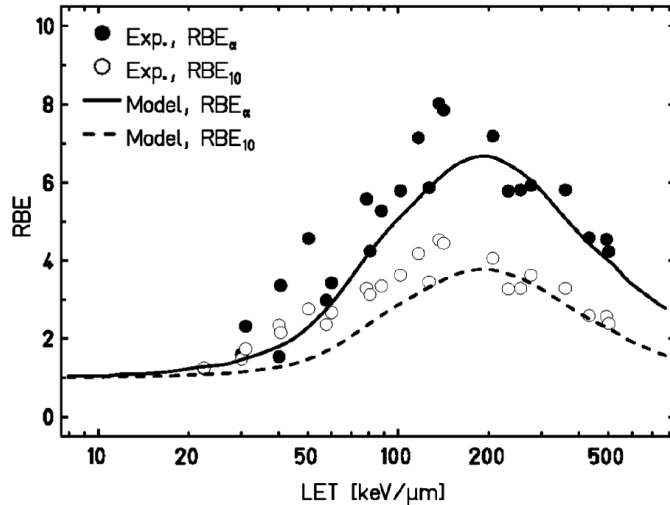
Figure 4.1: Example of RBE dependence on LET for carbon ion irradiation for the sterilization of V79 Chinese hamster ovary cells. Note that RBE generally increases with LET until reaching a peak RBE. After this peak RBE, a further increase in LET leads to a decrease in RBE, *i.e.*, the "overkill effect." Curves show the predictions of LEMIV. Figure reproduced from Friedrich *et al.* (2012), and the experimental data were acquired by Furusawa *et al.* (2000).

charged particles is needed. Very little data are available describing cancer incidence in humans exposed to charged particle radiation. Further, since the exact mechanism of cancer induction by radiation is not known, it is not possible to assume the same RBE will hold for different endpoints, *e.g.*, cell sterilization *versus* tumor induction. Furusawa *et al.* (2000) investigated cell sterilization as a function of ion species and LET, reporting RBEs for cell sterilization by helium, carbon, and neon ions in a range of approximately 1-10, depending on cell line and endpoint and generally increasing with LET until the overkill effect was reached, *i.e.*, with an RBE maximum at approximately 100-200 keV/μm for carbon ions (cf. Figure 4.1). Similar findings were reported for cell sterilization by carbon ions with dependencies on the repair capacity of cell lines (Weyrather *et al.*, 1999). Given this knowledge, a general increase of RBE *versus* LET might be expected for cancer induction after ion irradiation (Fry *et al.*, 1985) and, indeed, an increase in the yield of chromosomal aberrations with increasing LET per unit dose is seen in vitro for heavy ions, compared with photons (Durante *et al.*, 2002), but in vitro cell results cannot be directly used to infer cancer risks in vivo. Also, the saturation effect, *i.e.*, "overkill effect," that is typically seen in RBE *versus* LET studies for the endpoint of cell sterilization may or may not be expected for the endpoint of tumor induction. Alpen *et al.* (1993) studied the RBE for tumorigenesis in the Harderian gland of the mouse for irradiation with hydrogen,

helium, neon, iron, and niobium ions and reported a linear increase in RBE *versus* LET over a large range of 1-1000 keV/μm, with no observed decrease in RBE at high LET. Furthermore, RBE for ion beams has been shown to not only depend on the ion LET but also on the ion species (Furusawa *et al.*, 2000; Friedrich *et al.*, 2013a). Despite these challenges, risk estimations, however coarse, for cancer incidence after exposure to ion radiation can offer valuable insights and provide new fuel for future research efforts in the fields of both radiation oncology and space exploration. Indeed, the same difficulties in estimating RBE for tumor induction by ion irradiation exist for those who try to predict and minimize cancer risks for astronauts who would be exposed to cosmic rays during extended space missions (Durante and Cucinotta, 2008; NCRP, 2006; NRC, 2008).

For some HL patients, scanned carbon ion therapy might reduce physical dose to normal tissues upstream of the target compared with scanned proton therapy. However, estimation of the risks of secondary malignant neoplasms for these patients is not straightforward and likely depends on complex, competing relations between the RBE for HL tumor control, RBE for normal tissue tumor induction, and RBE for normal tissue sterilization, which likely all depend on the radiation particle spectrum and the radiosensitivity of individual tissues. To our knowledge, a study comparing second cancer risk in the breast for HL patients after carbon ion *versus* proton radiotherapy has not been reported in the literature.

The purpose of this study was to determine whether using carbon ion therapy instead of proton therapy would show a difference in the predicted risk of second cancer incidence in the breast for female HL patients. To achieve this, we simulated scanned proton and scanned carbon ion treatment for 6 HL patients using a research treatment planning system for ion radiotherapy. We calculated relative predicted risks of second cancer in the breast using a linear-no-threshold tumor induction model and a linear-quadratic breast cell inactivation model. We explicitly modeled RBE values for the ion fields for both breast tumor induction and cell inactivation. We further investigated the sensitivity of our risk predictions to uncertainties in our RBE calculations.

4.2   Methods

4.2.1   Patient Sample

We selected patient records for 6 women who had previously received passively scattered proton therapy for HL with stage IIA, IIB, or IIBE diagnoses and disease targets localized above the diaphragm. These patient records were consecutively sampled based

on 2 criteria: (1) these women were previously determined by radiation oncologists at UTMDACC to be valid candidates for proton therapy, (2) disease targets were located superior to the diaphragm. Many of these supradiaphramatic targets required particle beams traversing healthy breast tissue and thus were appropriate test cases for radiogenic second cancer incidence risk in the breast. Data for these patients were collected under a retrospective research protocol approved by our institutional review board. All protected health information was removed from the electronic medical record using the methods of Newhauser et al. (in preparation).

4.2.2 Treatment Planning

Treatment planning for scanned proton therapy and scanned carbon ion therapy was performed using the TRiP98 TPS (Krämer *et al.*, 2000; Krämer and Scholz, 2000) and the Local Effect Model Version IV (LEMIV) (Scholz *et al.*, 1997; Elsässer *et al.*, 2010) at GSI. To review, the principle of the Local Effect Model (LEM) (Scholz *et al.*, 1997) is that, microscopically, the biological response of DNA to photon and ion irradiation is essentially the same. However, the dose distributions produced by ion irradiation are highly non-uniform at the microscopic level (*e.g.*, nm to μm scale), and thus *macroscopic* dose is a poor indicator of biologic effect after ion irradiation. By using an amorphous track structure model, one can predict the microscopic distribution of dose from ion irradiation within a cell nucleus and use that to predict the distribution of "lethal events" (*e.g.*, that would be produced by an equivalent microscopic dose of photons). By integrating the number of these lethal events over the cell nucleus, one can compare that ion dose with the photon dose that would produce an equivalent number of lethal events and, thus, estimate a macroscopic RBE value for ion irradiation. A more recent extension of that model (LEMIV) (Elsässer *et al.*, 2010) uses similar theory but goes one step further to predict the number of DNA double-strand breaks (DSBs) and to score the complexity of DNA damage, *i.e.*, scoring the number of DSBs that occur within a very small (*e.g.*, 540 nm) distance scale. Multiple DSBs to the DNA within very small distances are considered more lethal than the same number of DSBs spread further apart throughout the DNA structure. Similar to the initial LEM, LEMIV links known photon biological response to predicted ion biological response, considering the microscopic track structure of ions and the complexity of DNA damage at a microscopic level. Hence, LEMIV can be used similarly to determine macroscopic RBE values for use in treatment planning and dose optimization for ion radiotherapy.

For all patients, scanned proton and scanned carbon treatment plans were prepared according to the following procedure.

① Following the methods of Elsässer *et al.* (2010), RBE tables were computed using LEMIV for the HL target and the breast. These tables consisted of the RBE values for carbon and all lighter ions down to hydrogen at various kinetic energies. The RBE values in these tables specifically represented the RBE values for the case when a single particle traverses the cell nucleus; these values were used as input to TRiP98 to allow calculation of RBE weighted dose for particle fields with mixed ion species and kinetic energies and mixed LET (Krämer and Scholz, 2006).

- For the HL target, RBE tables were calculated based on a linear-quadratic model for sterilization of the HL tumor using α/β of 8 Gy, with $\alpha = 0.2$ Gy^{-1} and $\beta = 0.025$ Gy^{-2}.

- For the breast, RBE tables were calculated for breast cell sterilization α/β of 3 Gy (Yarnold *et al.*, 1995, 2005; Schneider *et al.*, 2011), with $\alpha = 0.12$ Gy^{-1} and $\beta = 0.04$ Gy^{-2}.

② Computed tomograms (CT) and organ contours from the HL patient records were loaded into the TPS.

③ Scanned proton and scanned carbon fields were planned to irradiate the clinical target volume (CTV) using a single anterior-to-posterior beam direction for each patient.

- Pencil beams had focal spot sizes of 12.4 ± 1.7 mm full-width at half-maximum (FWHM) for protons and 7.0 ± 0.3 mm FWHM for carbon ions, typical of clinical parameters used at HIT (Heidelberg, Germany).

- Pencil beam Bragg peak coordinates were regularly spaced laterally with 2 mm between raster spots and isoenergy slices were regularly spaced with approximately 3 mm water-equivalent depth separation.

- A 3-mm ripple filter was used to broaden the carbon Bragg peak along the depth axis (Weber and Kraft, 1999).

- A lateral margin of 1.1× FWHM of the pencil beams was used to achieve sufficient lateral scatter equilibrium for dose coverage at the lateral target boundary. A distal margin of 4 mm was used to cover the deepest portion of the target.

④ Particle numbers were optimized for each pencil beam to provide a uniform RBE-weighted dose per fraction of 2 Gy (RBE) to the CTV, *i.e.*, that would be delivered in 18 fractions for 36 Gy (RBE) total. A gradient search minimization was used to minimize the objective function; the minimizer was stopped once the relative change in the objective function dropped below 1×10^{-3}.

(5) Both absorbed dose and RBE-weighted dose were calculated in each CT voxel using the TPS. For voxels in the CTV, the RBE table for HL tumor sterilization was used. For all other voxels in the patient, the RBE table for breast cell sterilization was used.

(6) Dose-averaged LET (*i.e.*, the LET value was weighted by the absorbed dose in averaging) was calculated in each CT voxel for the particle spectra produced by the proton and carbon fields (Krämer and Scholz, 2006).

For each treatment plan, we used the reference RBE table for breast cell sterilization with $\alpha/\beta = 3$ Gy, as mentioned above. However, we also performed a sensitivity test by recalculating RBE-weighted dose to the breast using RBE tables with $\alpha/\beta = 1$ Gy and $\alpha/\beta = 5$ Gy. Similarly, we recalculated treatment plans using RBE tables for the HL tumor with α/β ratios of 6, 8, and 10 Gy. Although the exact α/β ratio for HL tumors is not known (to our knowledge), we estimated a value of 8 Gy based on clinical experience at UTMDACC and attempted to bracket a range of plausible values from 6-10 Gy. D_T, the dose at which the linear-quadratic cell survival curve transitions to a purely linear curve, was estimated for each α/β ratio using an empirical estimate at GSI, that is $D_T = 1.1 \times \alpha/\beta + 4$ Gy.

To visualize our treatment plans, we prepared dose colorwash 2D cuts from the 3D dose distributions and overlaid these on corresponding CT slices along with the CTV and organ contours. We prepared histograms of RBE_S-weighted dose to the breast. We plotted dose-averaged LET colorwash maps overlaying the organ contours. To visualize the entire distribution of dose-averaged LET in the breast for the carbon and proton treatment plans simultaneously for all patients, we plotted histograms of dose-averaged LET in all breast voxels from all patients. Further, we plotted RBE_S colormaps and histograms of RBE_T in breast to better understand the spectra of RBE predicted for these patients.

4.2.3 Calculation of Relative Risks of Secondary Malignant Neoplasms

In order to minimize the number of variables that contribute to uncertainty in risk prediction for secondary malignant neoplasms, we considered only the *ratio* of predicted risks of breast cancer incidence for the carbon *versus* proton treatment plans. Following the methods of Newhauser *et al.* (2009) and Fontenot *et al.* (2010), we calculated the ratio of predicted breast cancer incidence risk (R_c/R_p) for each patient comparing proton (p) and carbon (c) therapy as

$$\frac{R_c}{R_p} = \frac{\langle T_c \cdot S_c \rangle}{\langle T_p \cdot S_p \rangle}, \tag{4.1}$$

where T is the probability of tumor induction and S is the surviving fraction of breast cells. We calculated T and S at points on a 3D grid with 8-mm spacing throughout the patient. The brackets indicate that we averaged the point calculations of $T \cdot S$ for all points in the breast for carbon and proton plans before taking the ratio of risk. For the tumor induction term, we used a linear-non-threshold model with a modification to account for the variable RBE of protons and carbon ions for carcinogenesis.

$$T = \mu \cdot D \cdot \text{RBE}_T, \tag{4.2}$$

where μ is the slope of risk per absorbed dose D that is typically seen in linear-non-threshold photon risk models. However, in this study, μ in the numerator and the denominator cancelled and thus had no effect on our ratio of risk (R_c/R_p). To estimate the RBE for ions for tumor induction (RBE_T), we developed a linear model of RBE *versus* LET, based on our interpretation of the literature (Alpen *et al.*, 1993; Hawkins, 1998; Carabe *et al.*, 2012; NCRP, 2006).

$$\text{RBE}_T = 1 + k \cdot \text{LET}, \tag{4.3}$$

where k depends on ion species. A precondition for this equation to be valid is that the LET is sufficiently small that saturation effects, such as the "overkill effect," do not play a role. We assumed a fixed relation between proton and carbon $(k_p = \kappa \cdot k_c)$ and estimated a plausible range for k_c as $(0.01 < k_c < 0.09)$ μm/keV, corresponding to an RBE maximum of 2-10 for carbon at 100 keV/μm, inferred from cell survival RBE data reported by Furusawa *et al.* (2000). We estimated κ to fall in the plausible range of $(1 < \kappa < 5)$ (Schardt *et al.*, 2010; Friedrich *et al.*, 2013a). Assuming that only surviving breast cells pose risk for tumor induction, we used a linear-quadratic survival calculation (Hall and Giaccia, 2006)

$$S = \exp\left\{ -n \left[\alpha \cdot d \cdot \text{RBE}_S + \beta (d \cdot \text{RBE}_S)^2 \right] \right\}, \tag{4.4}$$

where n is the number of fractions (*i.e.*, $n = 18$), d is the absorbed dose per fraction to a point in the breast. RBE_S was calculated using the treatment planning system, and α and β values for breast cell sterilization were those described in Section 4.2.2.

To test the sensitivity of our computed risk ratios to uncertainties in our risk model parameters, we plotted (R_c/R_p) for all patients for the range of k_c and κ discussed above and with varying α/β ratios for breast cell sterilization of 1, 3, and 5 Gy and with varying α/β ratios for HL tumor sterilization of 6, 8, and 10 Gy. In addition, we prepared histograms of RBE_T for all breast voxels for the proton and carbon treatment plans for a reference case with $k_c = 0.05$ μm/keV and $\kappa = 3$ to better illustrate the distribution of RBE_T predicted

by our model.

4.2.4 Statistical Analysis of Risks

For our risk comparisons and range of sensitivity testing, we performed a two-sided Sign Test using MATLAB (MathWorks, Natick, Massachusetts). That is, we tested the null hypothesis H_o that proton therapy and carbon-ion therapy provided equal risk of second cancer incidence in the breast for the 6 HL patients. This could be expressed mathematically as

$$H_o : \Delta = 0, \tag{4.5}$$

and

$$H_1 : \Delta \neq 0, \tag{4.6}$$

where

$$\Delta = \text{median} \left[\left(\frac{R_c}{R_p} \right)_i - 1 \right], i = 1, 2, 3, 4, 5, 6. \tag{4.7}$$

For each of the sensitivity tests described in Section 4.2.3, we analyzed (R_c/R_p) for all patients (i) and computed a p-value. If the p-value was less than 0.05, we rejected the null hypothesis and accepted the alternative hypothesis H_1. When we accepted the alternative hypothesis, we interpreted findings of $\Delta < 0$ to imply that carbon-ion therapy tended to result in a lower risk of second cancer incidence in the breast than proton therapy. Conversely, we interpreted findings of $\Delta > 0$ to imply that carbon-ion therapy tended to result in a higher risk of second cancer incidence in the breast than proton therapy.

4.3 Results

4.3.1 Treatment Plans and RBE-Weighted Dose Distributions

A comparison of proton and carbon ion treatment plans are shown in Figure 4.2 for HL Patient #1. Compared to the proton plan, the carbon plan shows higher conformity of dose to the CTV with more rapid falloff of the high dose region both laterally and distally to the CTV. A lower RBE-weighted dose (*i.e.*, RBE$_S$-weighted dose) is seen in the left breast for carbon *versus* proton, both in the lateral penumbra and in the primary beam entrance path. A lower RBE-weighted dose is also seen in the right breast, due to the sharper lateral penumbra of the carbon beam. Interestingly, the carbon treatment plan shows a halo-shaped region of overdose in healthy tissue near the border of the CTV on
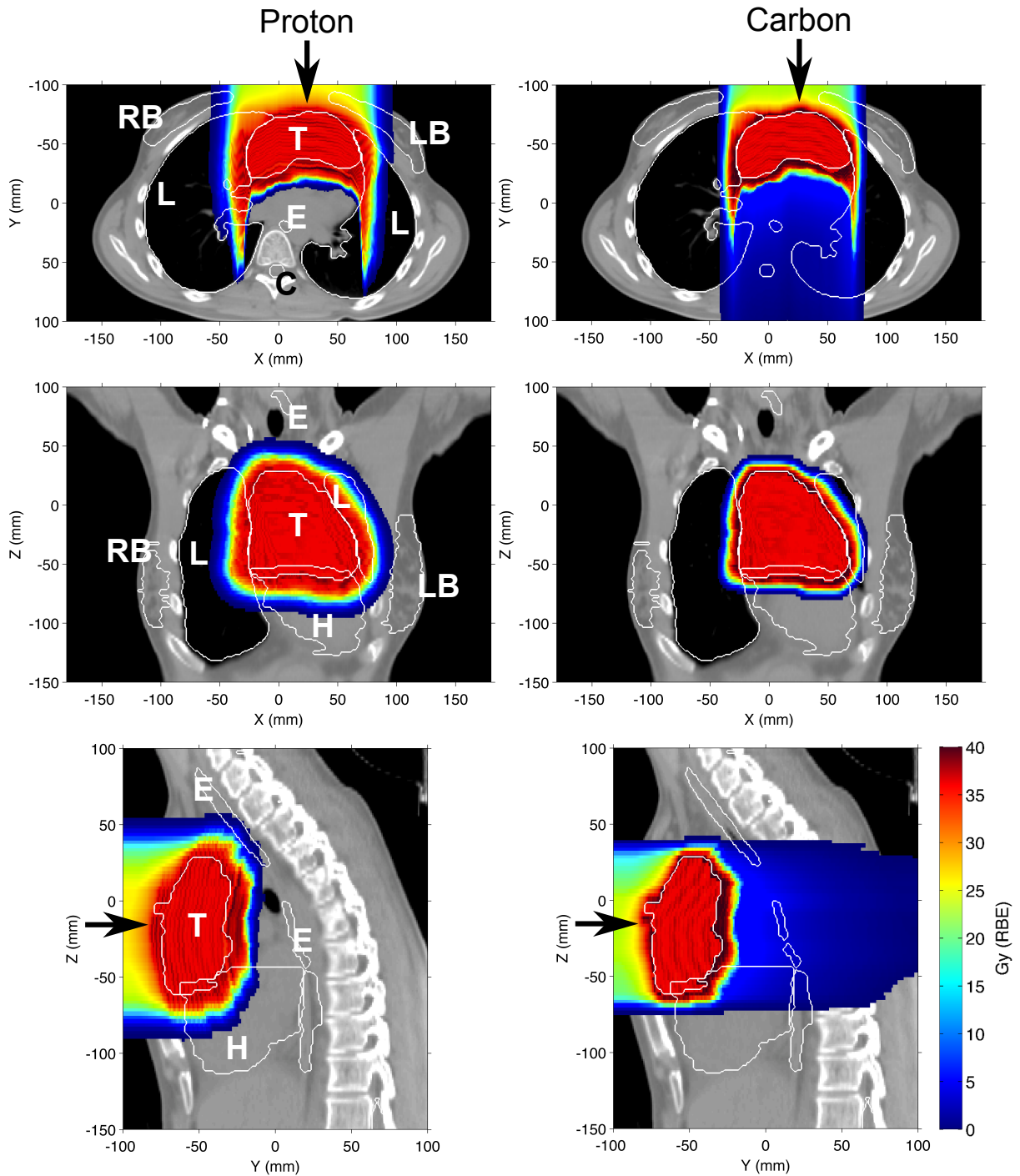
Figure 4.2: Scanned proton (left) and scanned carbon ion (right) treatment plans for HL Patient #1. RBE-weighted dose colorwash is shown overlaying axial (top), coronal (middle), and sagittal (bottom) CT slices. Contours (white lines) are shown for the CTV (T), right breast (RB), left breast (LB), lung (L), esophagus (E), spinal cord (C), and heart (H). RBE-weighted dose was calculated using one RBE table for HL tumor sterilization inside the CTV ($\alpha/\beta = 8$ Gy) and another RBE table for breast cell sterilization for all tissues outside the CTV ($\alpha/\beta = 3$ Gy). The prescribed CTV RBE-weighted dose was 36 Gy (RBE). Note the lower RBE-weighted dose, *i.e.*, RBE_S, in the left breast seen for the carbon plan compared with the proton plan.

all sides, due to the different radiosensitivity of the HL tumor and the surrounding normal tissue. It should be noted again that the RBE-weighted doses to all normal tissues were calculated using the RBE table for breast cell sterilization ($\alpha/\beta = 3$ Gy). In addition, a non-zero exit dose is seen for carbon that extends far beyond the distal CTV boundary, due to fragmentation of the carbon projectiles.

Figures 4.3 and 4.4 show axial views of the proton and carbon treatment plans for HL Patients #2 - #6. Differences between the carbon and proton plans for all patients were similar to those seen for Patient #1, namely:

- Carbon plans show a sharper lateral penumbra and higher conformity of therapeutic dose to the CTV than proton plans.

- Carbon plans show a faster distal falloff of dose than proton plans except for the fragmentation tail, which extends low dose far beyond the distal target boundary.

- Carbon plans show a lower RBE-weighted dose to the breast, *i.e.*, RBE_S-weighted dose, than proton plans for all patients.

- Carbon plans introduce a halo-shaped region of overdose in normal tissue near the CTV boundary, particularly on the downstream side of the target.

Figure 4.5 shows the distribution of RBE_S-weighted doses seen in the breast for all 6 HL patients as a histogram where all breast voxels for all patients have been combined in a single plot. The overall shapes of these differential RBE_S-weighted dose histograms were similar for the proton and carbon plans.

4.3.2 LET Distributions

To complement the treatment planning views presented above, Figure 4.6 shows 2D colorwash plots of the dose-averaged LET for proton and carbon ion therapy plans for HL Patient #1. As the ion beams enter the tissue, the LET is generally seen to increase with depth in tissue, as the ions lose kinetic energy. The highest LET is seen at the distal field boundary, where the deepest Bragg peaks are positioned. Carbon ion LET values are roughly 10 times higher than proton LET values, and for both ion species, the LET is lower in the breast than in the CTV. Entire distributions of dose-averaged LET for all breast voxels for all patients are shown as histograms in Figure 4.7 for the proton and carbon plans. Importantly, values of dose-averaged LET in the breast for both the proton and carbon ion plans for all patients were lower than typical values of LET where saturation
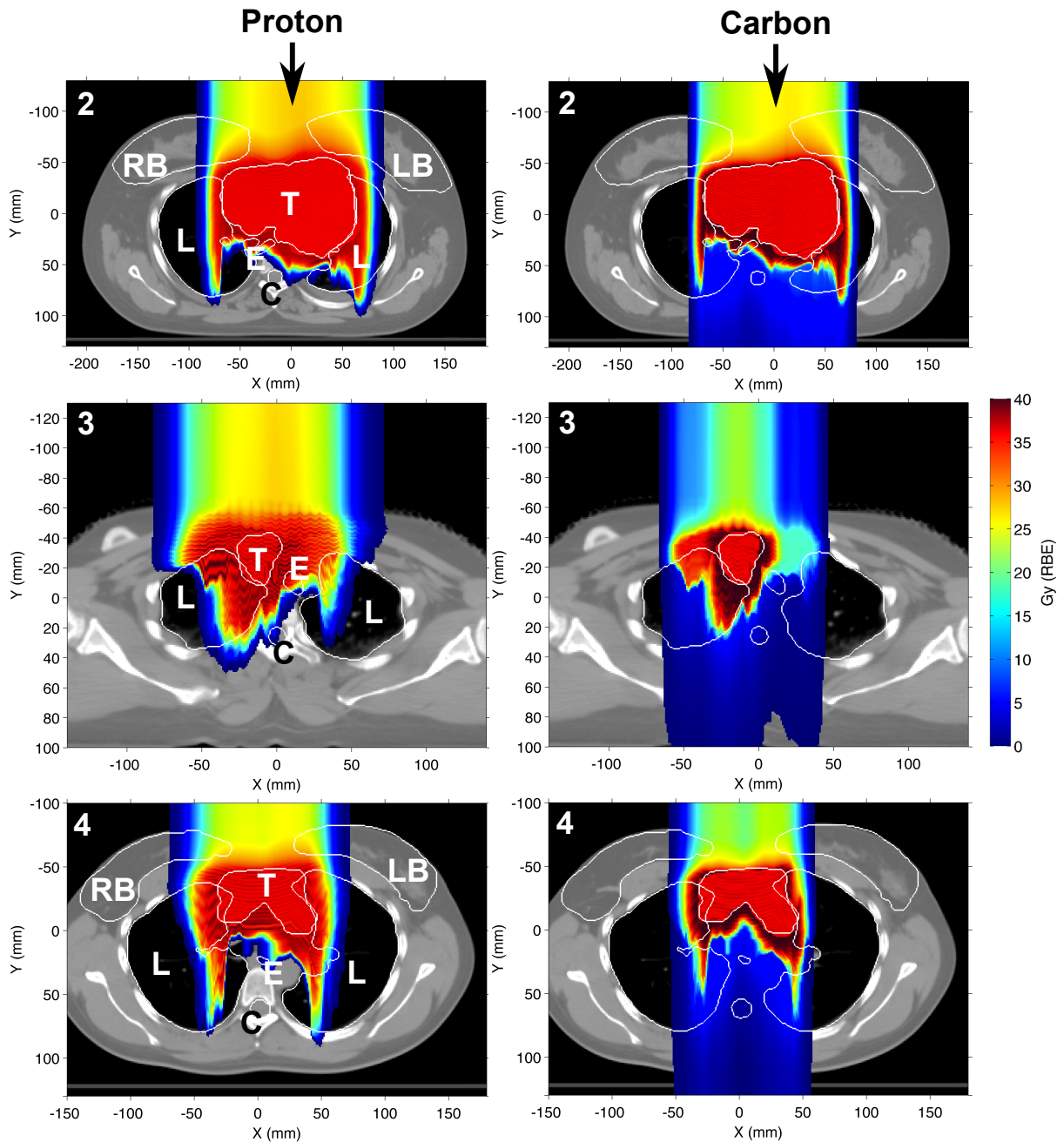
Figure 4.3: Axial view of scanned proton and scanned carbon ion treatment plans for HL Patients #2, #3, and #4. Patient number is indicated in the top left of each image. Contours (white lines) are shown for the CTV (T), right breast (RB), left breast (LB), lung (L), esophagus (E), spinal cord (C), and heart (H). RBE-weighted dose was calculated using one RBE table for HL tumor sterilization inside the CTV ($\alpha/\beta = 8$ Gy) and another RBE table for breast cell sterilization for all tissues outside the CTV ($\alpha/\beta = 3$ Gy). The prescribed CTV dose was 36 Gy (RBE).
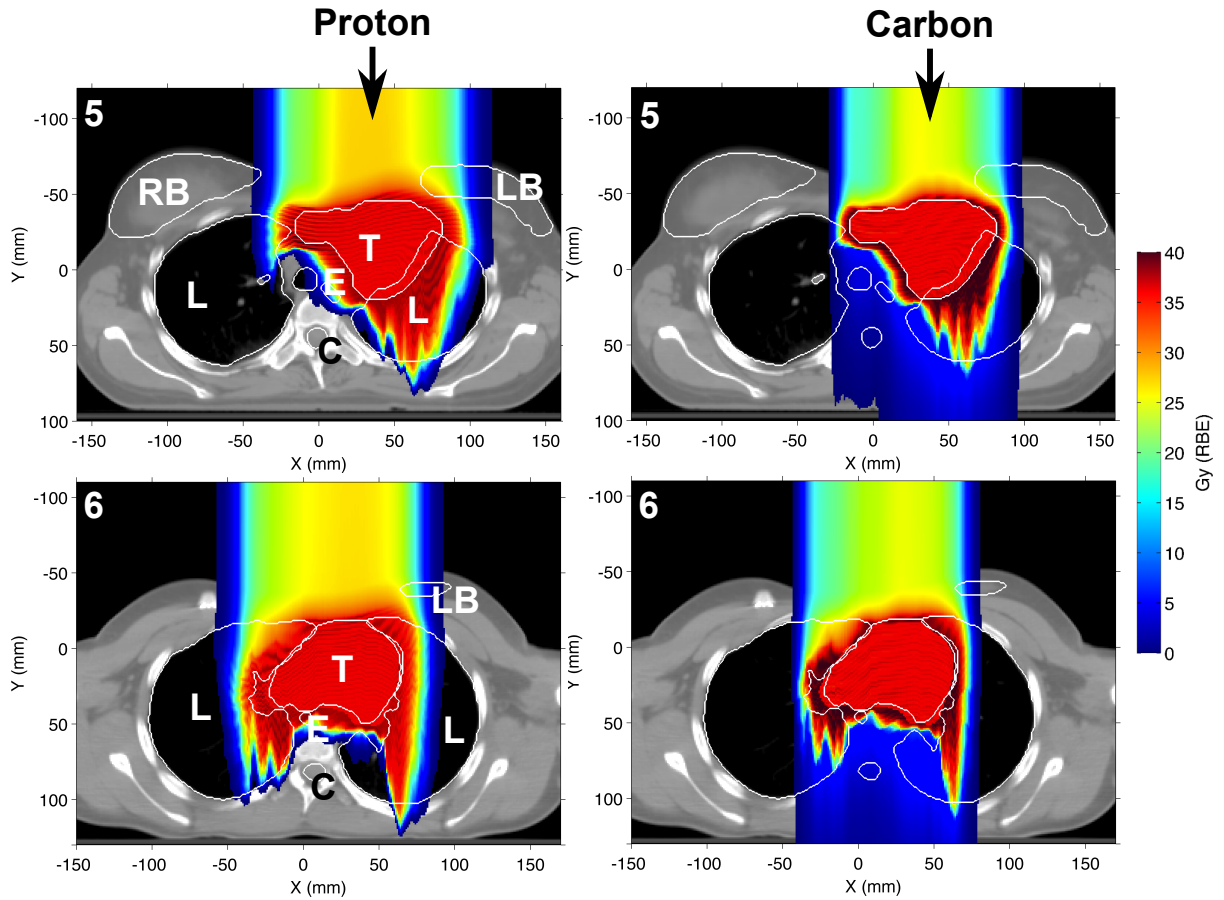
Figure 4.4: Axial view of scanned proton and scanned carbon ion treatment plans for HL Patients #5 and #6. Patient number is indicated in the top left of each image. Contours (white lines) are shown for the CTV (T), right breast (RB), left breast (LB), lung (L), esophagus (E), spinal cord (C), and heart (H). RBE-weighted dose was calculated using one RBE table for HL tumor sterilization inside the CTV ($\alpha/\beta = 8$ Gy) and another RBE table for breast cell sterilization was used for all tissues outside the CTV ($\alpha/\beta = 3$ Gy). The prescribed CTV dose was 36 Gy (RBE).
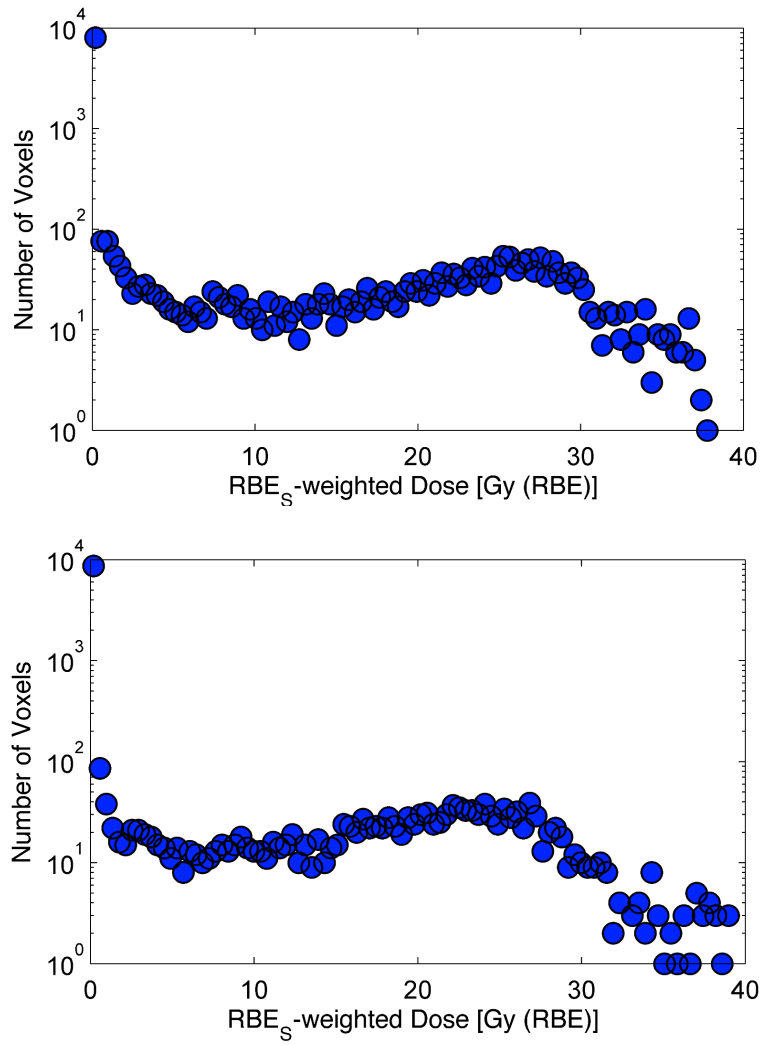
Figure 4.5: Histogram of RBE$_S$-weighted dose in breast voxels for scanned proton (top) and scanned carbon ion (bottom) treatment plans for all 6 patients.
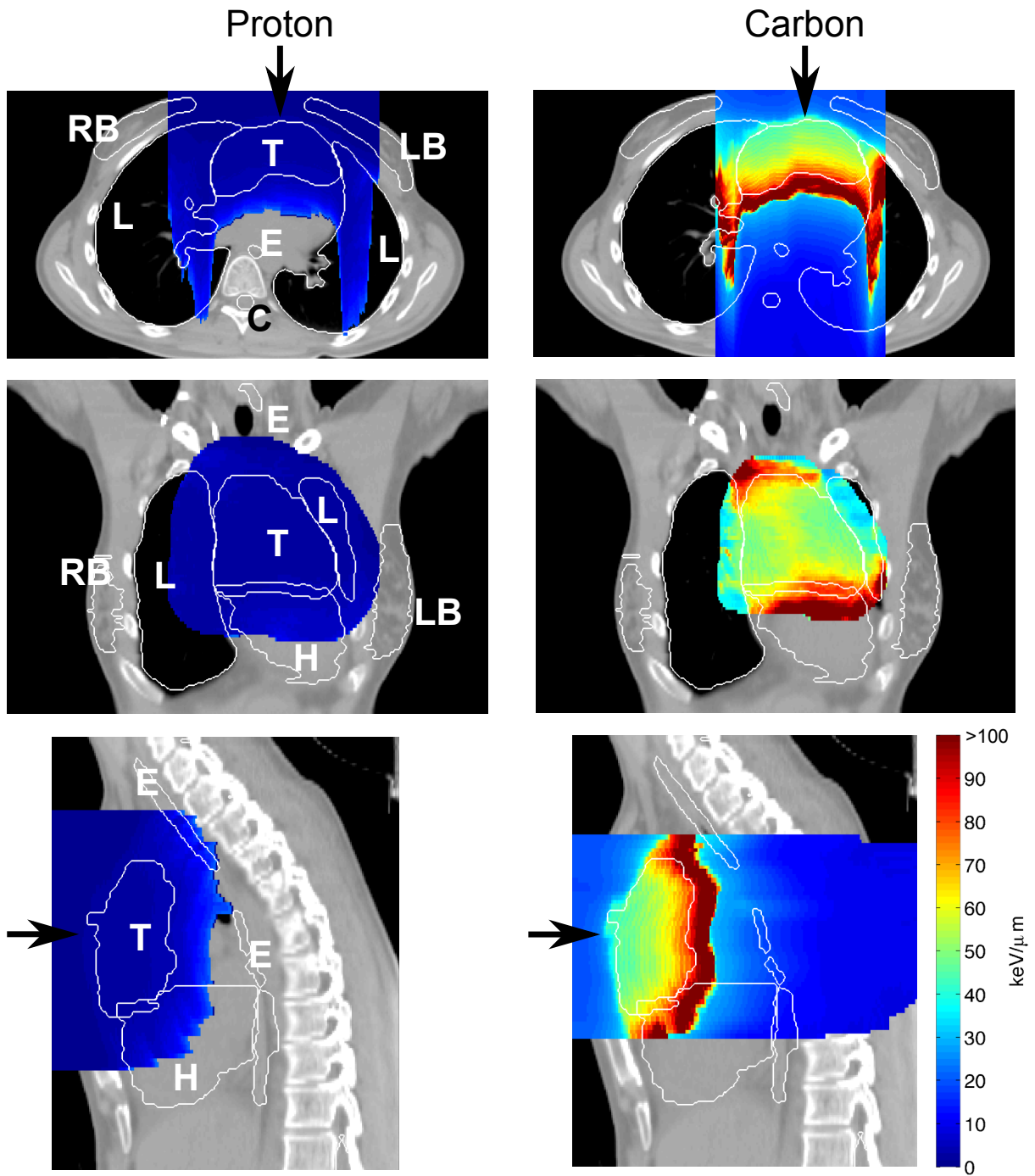
Figure 4.6: Distributions of dose-averaged LET shown for the scanned proton (left) and scanned carbon ion (right) treatment plans for HL Patient #1. Organ contours (white contours) are shown for the CTV (T), right breast (RB), left breast (LB), lung (L), esophagus (E), spinal cord (C), and heart (H). For both plans, higher LET is seen near the distal edge of the CTV but comparably low LET is seen in the breast.

Figure 4.7: Histogram of dose-averaged LET in breast voxels for scanned proton (top) and scanned carbon ion (bottom) treatment plans for all 6 patients.
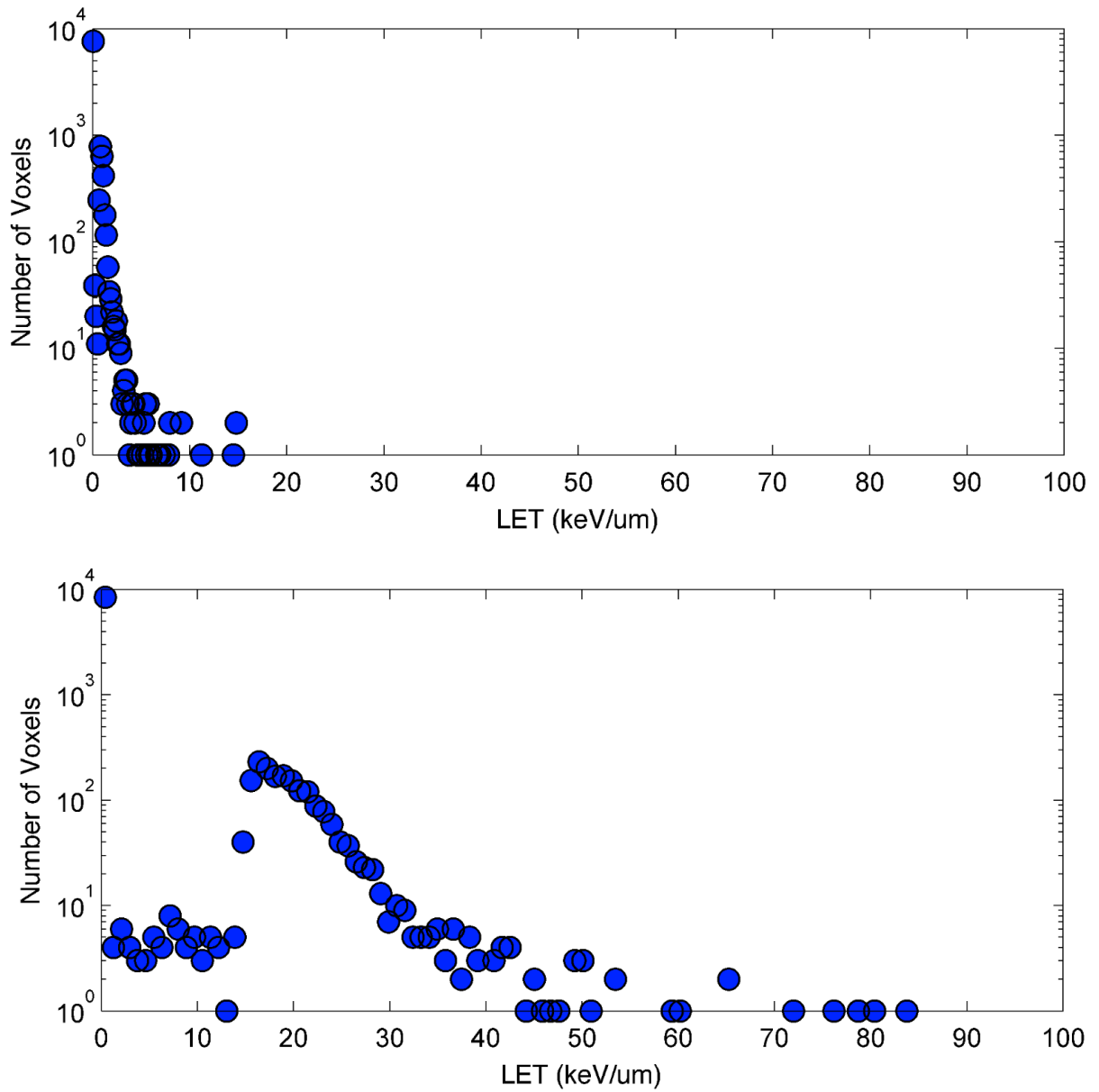
effects in RBE_S are known to occur, namely near 20-30 keV/μm for protons and near 100-200 keV/μm for carbon ions (cf. Figures 1.4 and 4.1).

4.3.3 RBE Distributions

An illustration of the predicted RBE_S values for cell sterilization, calculated by LEMIV, is shown for HL Patient #1 in Figure 4.8 for the reference case with breast cell $\alpha/\beta = 3$ Gy. Similar to the distributions of LET, the highest values of RBE_S, up to approximately 6 for both proton and carbon plans, were seen near the distal field boundary. Carbon plans showed a generally higher RBE_S in the target with a more gradual increase in RBE_S as the carbon ions approach the distal target edge compared to proton plans. Predictions of our model for RBE_T *versus* LET, *i.e.*, RBE values for tumor induction, are shown in Figure 4.9. Based on this model, an example of predicted RBE_T for voxels in the breast for all 6 patients for proton and carbon plans is shown in Figure 4.10. For our reference case of $k_c = 0.05$ μm/keV and $\kappa = 3$, RBE_T values are seen ranging from 1 to 3.3 for proton dose to the breast and from 1 to 5.3 for carbon dose to the breast.

4.3.4 Relative Risks of Second Cancer Incidence in Breast

The predicted ratios of risk (R_c/R_p) of breast cancer incidence for the 6 HL patients receiving scanned carbon ion *versus* scanned proton therapy are shown in Figures 4.11, 4.12, and 4.13, with α/β ratios for breast cell sterilization of 1, 3, and 5 Gy, respectively. For a breast α/β of 1 Gy, the mean ratio of risk for all patients, all k_c, and all κ was $(R_c/R_p) = 0.50 \pm 0.24$. For a breast α/β of 3 Gy, the mean ratio of risk for all patients, all k_c, and all κ was $(R_c/R_p) = 0.77 \pm 0.35$. For a breast α/β of 5 Gy, the mean ratio of risk for all patients, all k_c, and all κ was $(R_c/R_p) = 0.90 \pm 0.40$. Mean ratios of risk (R_c/R_p) for the 6 patients and results of our statistical analysis are presented in Table 4.1 for all variations of breast α/β, k_c, and κ for HL α/β of 8 Gy. For our reference case with breast $\alpha/\beta = 3$ Gy, HL tumor $\alpha/\beta = 8$ Gy, $k_c = 0.05$ μm/keV, and $\kappa = 3$, we did *not* find a significant difference in the risk of second cancer incidence in the breast using carbon-ion therapy instead of proton therapy for our sample of HL patients. However, some significant differences were found for some conditions examined in our sensitivity testing (cf. Table 4.1). First, we found that a lower breast α/β led to a lower predicted ratio of risk (R_c/R_p). Second, we found a higher k_c led to a higher ratio of (R_c/R_p). Third, we found that a higher κ led to a lower ratio of (R_c/R_p). We found the exact α/β ratio for the HL tumor to have minimal impact on our results for α/β of 6-10 Gy (cf. Appendix B).

Overall, these findings demonstrated that our predicted ratio of risk (R_c/R_p) was
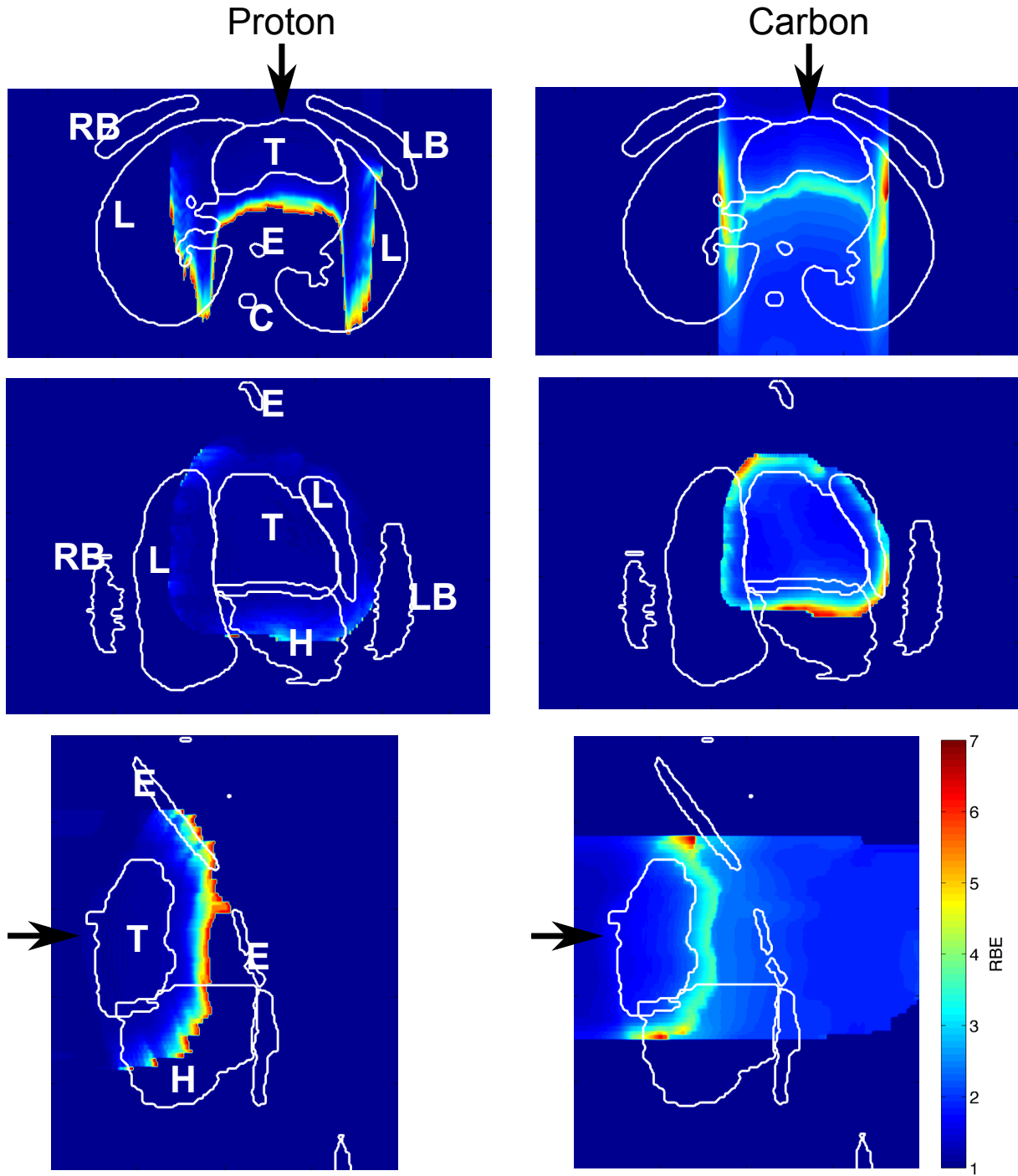
Figure 4.8: Distributions of RBE_S calculated with LEMIV shown for the scanned proton (left) and scanned carbon ion (right) treatment plans for HL Patient #1. These values correspond to the RBE_S-weighted dose distributions shown in Figure 4.2. In these calculations, α/β was 8 Gy for the HL CTV and 3 Gy for the breast and all other tissue. Organ contours (white contours) are shown for the CTV (T), right breast (RB), left breast (LB), lung (L), esophagus (E), spinal cord (C), and heart (H). For both plans, higher RBE is seen near the distal edge of the CTV, where the dose-averaged LET was highest (cf. Figure 4.6).
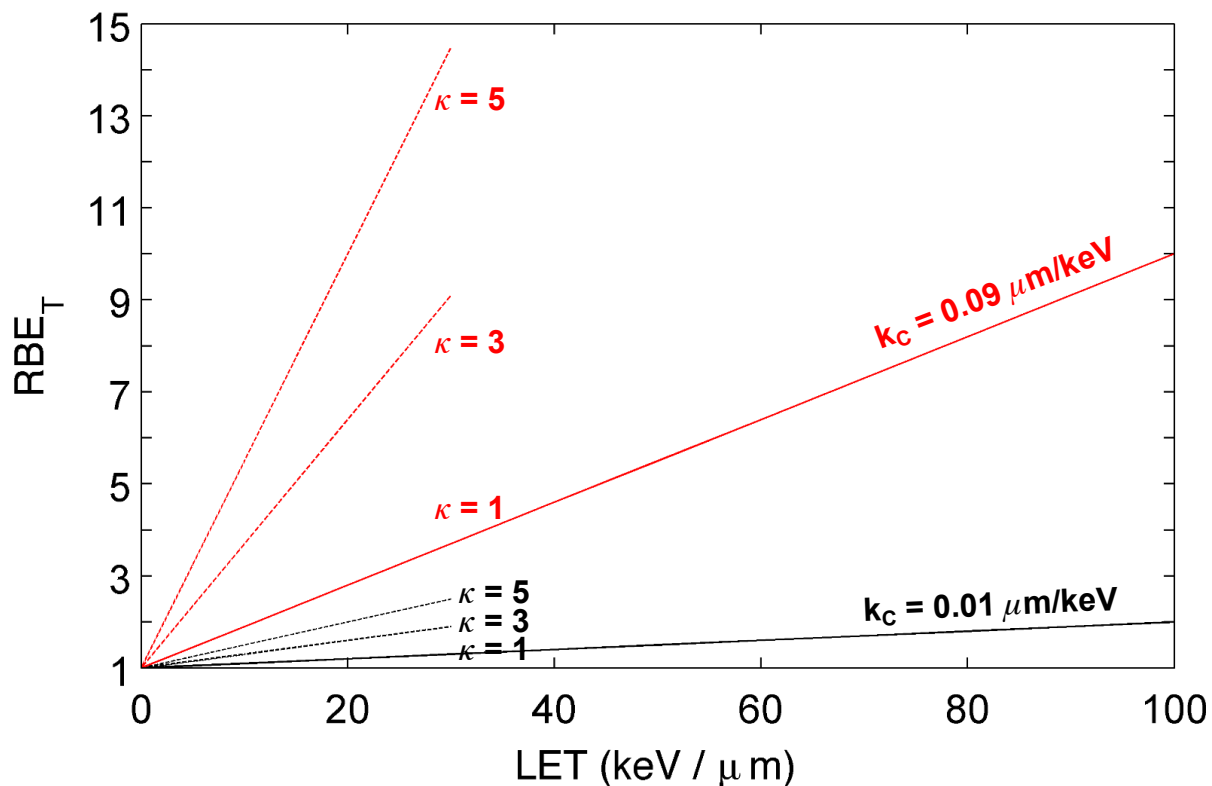
Figure 4.9: RBE_T *versus* LET model predictions (cf. Equation 4.3) shown over the range of parameters used in this study, with $k_c = 0.01$ μm/keV (black lines) and 0.09 μm/keV (red lines) and $\kappa = 1$, 3, and 5. The solid lines represent the RBE_T for carbon irradiations and the dashed lines, which stop at 30 keV/μm, represent the RBE_T for proton irradiations. If $\kappa = 1$, then $k_p = k_c$. Model predictions for $k_c = 0.05$ μm/keV are not shown here but appeared similar in shape.

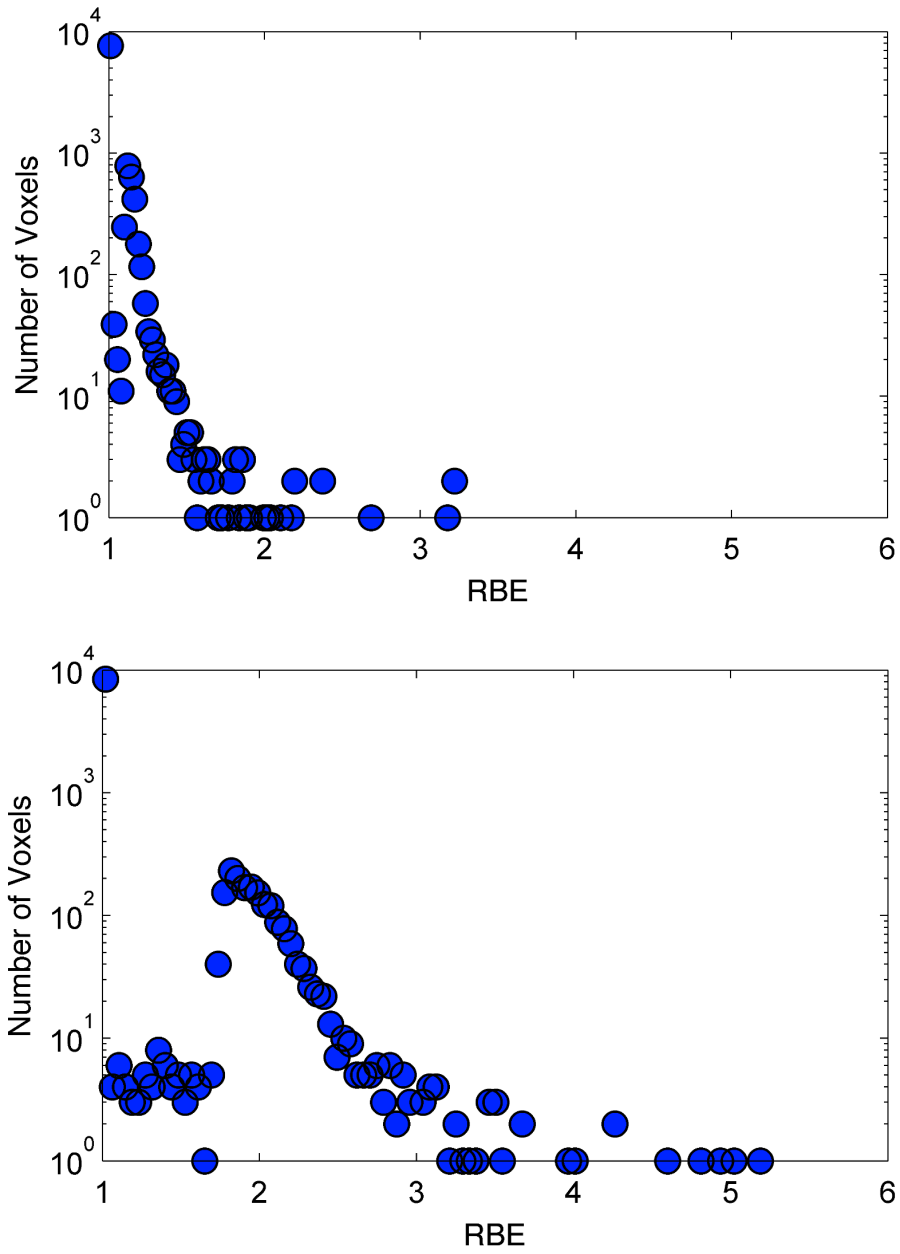Figure 4.10: Histograms of predicted RBE$_T$ for tumor induction in breast voxels for proton plans (top) and carbon ion plans (bottom) for all 6 patients for our reference case with $k_c = 0.05$ μm/keV and $\kappa = 3$ (cf. Equation 4.3).

Figure 4.11: Predicted ratio of risk (R_c/R_p) for breast cancer incidence for the 6 HL patients receiving scanned carbon *versus* scanned proton therapy when $\alpha/\beta = 1$ Gy for breast cell sterilization and $\alpha/\beta = 8$ Gy for HL tumor sterilization. For each patient, risk ratios are shown for k_c values of 0.01 μm/keV (squares), 0.05 μm/keV (circles), and 0.09 μm/keV (triangles), *i.e.*, corresponding to peak RBE_T values for carbon of 2, 6, and 10 at 100 keV/μm, respectively. For each k_c, we also calculated risk ratios with variable κ of 1, 3, and 5. Within each cluster of like k_c values, an increasing ratio of risk was found with decreasing κ.
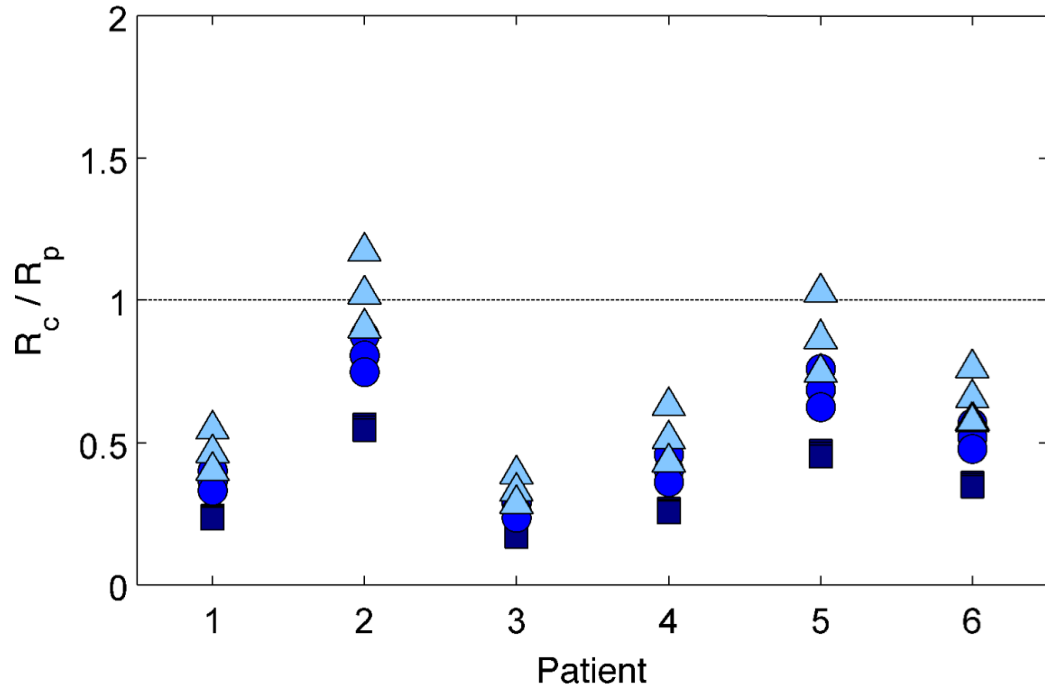
Figure 4.12: Predicted ratio of risk (R_c/R_p) for breast cancer incidence for the 6 HL patients receiving scanned carbon *versus* scanned proton therapy when $\alpha/\beta = 3$ Gy for breast cell sterilization and $\alpha/\beta = 8$ Gy for HL tumor sterilization. For each patient, risk ratios are shown for k_c values of 0.01 μm/keV (squares), 0.05 μm/keV (circles), and 0.09 μm/keV (triangles), *i.e.*, corresponding to peak RBE$_T$ values for carbon of 2, 6, and 10 at 100 keV/μm, respectively. For each k_c, we also calculated risk ratios with variable κ of 1, 3, and 5. Within each cluster of like k_c values, an increasing ratio of risk was found with decreasing κ.
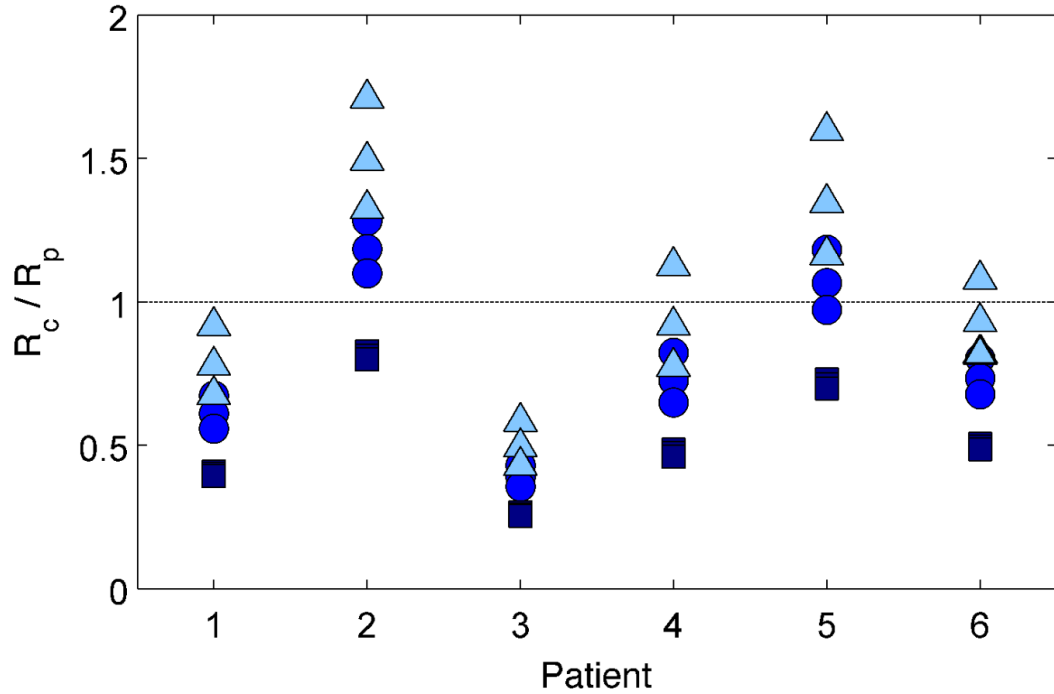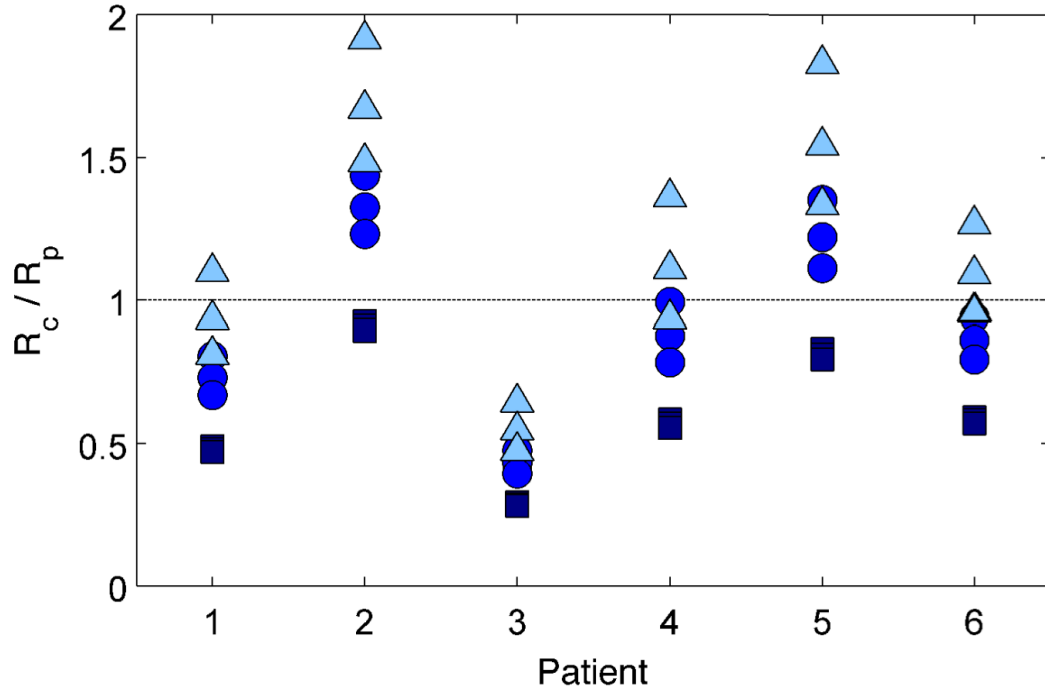
Figure 4.13: Predicted ratio of risk (R_c/R_p) for breast cancer incidence for the 6 HL patients receiving scanned carbon *versus* scanned proton therapy when $\alpha/\beta = 5$ Gy for breast cell sterilization and $\alpha/\beta = 8$ Gy for HL tumor sterilization. For each patient, risk ratios are shown for k_c values of 0.01 μm/keV (squares), 0.05 μm/keV (circles), and 0.09 μm/keV (triangles), *i.e.*, corresponding to peak RBE_T values for carbon of 2, 6, and 10 at 100 keV/μm, respectively. For each k_c, we also calculated risk ratios with variable κ of 1, 3, and 5. Within each cluster of like k_c values, an increasing ratio of risk was found with decreasing κ.

Table 4.1: Mean ratios of predicted risk $< R_c/R_p >$ (averaged over 6 patients) and significance (p-value) for second cancer incidence in breast for HL patients over the interval of biological parameters varied in our sensitivity testing (cf. Section 4.2.3) with α/β for HL tumor sterilization of 8 Gy. Δ was used for our Sign Test (cf. Equation 4.7). p-values greater than 0.05 were considered insignificant (shown in red).

Breast α/β (Gy)	k_c (μm/keV)	κ	$< R_c/R_p >$	Δ	p-value
1	0.01	1	0.35	-0.69	0.03
		3	0.34	-0.69	0.03
		5	0.33	-0.70	0.03
	0.05	1	0.56	-0.49	0.03
		3	0.51	-0.54	0.03
		5	0.46	-0.58	0.03
	0.09	1	0.75	-0.30	0.69
		3	0.64	-0.42	0.22
		5	0.56	-0.50	0.03
3	0.01	1	0.54	-0.51	0.03
		3	0.53	-0.52	0.03
		5	0.51	-0.53	0.03
	0.05	1	0.87	-0.19	0.69
		3	0.79	-0.27	0.69
		5	0.72	-0.34	0.22
	0.09	1	1.17	0.10	0.69
		3	0.99	-0.08	0.69
		5	0.86	-0.20	0.69
5	0.01	1	0.62	-0.41	0.03
		3	0.61	-0.42	0.03
		5	0.59	-0.44	0.03
	0.05	1	1.00	-0.03	0.69
		3	0.91	-0.13	0.69
		5	0.83	-0.21	0.69
	0.09	1	1.35	0.31	0.22
		3	1.15	0.10	0.69
		5	1.00	-0.05	0.69

highly dependent on the exact value of biological parameters used in our risk model. While carbon-ion therapy showed a lower predicted risk of second cancer incidence in breast compared to proton therapy for most of our sensitivity testing, the large uncertainties in biological parameters prevented us from rejecting the null hypothesis (H_o) that proton therapy and carbon-ion therapy provided equal risk of second cancer incidence in the breast for HL patients.

4.4   Discussion

In summary, we investigated whether using carbon ion therapy instead of proton therapy would show a difference in the predicted risk of second cancer incidence in the breast for female HL patients. We simulated proton and carbon-ion therapy for 6 HL patients and modeled the ratio of risk for breast cancer incidence after therapy, considering the biological effectiveness of ion beams. We found that the predicted risk of second cancer incidence in the breast after carbon ion therapy *versus* proton therapy was highly dependent on the RBE for tumor induction and highly sensitive to the α/β ratio for breast cell sterilization. (R_c/R_p) decreased with decreasing breast cell α/β. We found risk predictions to be only minimally sensitive to the α/β ratio for sterilization of the HL tumor (see Appendix B). For the estimated range of RBE_T studied in this work and for a reference α/β ratio of 3 Gy for breast cell sterilization, we did not find a significant difference in the predicted risk of second cancer incidence in the breast using carbon ion therapy instead of proton therapy. (R_c/R_p) was 0.77 ± 0.35. However, our findings support that carbon ion therapy might be beneficial to decrease risks of radiogenic second cancers for tissues with very low α/β ratios, *e.g.*, less than 3 Gy.

Due to the large biological uncertainties present, it is difficult to draw strong conclusions from this study. Nonetheless, our findings indicate an important trend, and our interval of calculated risk ratios suggest that it could be better to use carbon ion therapy for tissues with low α/β and better to use protons for tissues with high α/β with respect to carcinogenesis. We interpret this finding to mean that RBE for cell sterilization by carbon irradiation was higher for low α/β and, thus, the sterilization of cells decreased the risk of tumor induction by carbon at low α/β for the breast. This finding is theoretically consistent with the analysis of Friedrich *et al.* (2013b), who reported an inverse relation between RBE and α/β at low doses. Perhaps one of the greatest strengths of this work is that we bring some questions to light that must be answered before strong clinical decisions can be made. Our findings remind us that continued investigations of the RBE for tumor

induction by ion irradiation at various LET ranges are in dire need. These investigations would not only benefit the cancer patients undergoing radiotherapy but also could benefit manned space exploration programs (Durante and Cucinotta, 2008; NCRP, 2006). Although we hesitate to draw strong conclusions, one clinical implication of this study could be that, since carbon-ion therapy does not appear to offer a significant ability to reduce breast cancer risk compared with proton therapy, carbon-ion therapy might not be needed for HL patients. If true, that might benefit patients and taxpayers financially since proton therapy is generally less expensive than carbon-ion therapy to deliver. Whether carbon-ion therapy might reduce the risk of other side effects for HL patients compared to proton therapy, *e.g.*, lung cancer risk or cardiac toxicity risk, remains to be investigated. If no strong ability to reduce risks of side effects is found for carbon *versus* proton for HL patients, proton therapy might also be safer to deliver than carbon ion therapy, since the impact of some uncertainties in RBE modeling are dampened by the lower LET and greater range straggling of protons compared to carbon ions. That is, mistakes in RBE modeling might be washed out more in proton therapy than carbon ion therapy.

Reports from the literature caution that "the data for induction of cancer in humans by protons or heavy ions is insufficient for the estimation of [cancer] risks" (NCRP, 2006). However, much stands to be gained by carrying out this research, and scientists in both radiation oncology (Newhauser *et al.*, 2009) and space exploration fields (NRC, 2008) continue to coarsely estimate these risks, despite their large uncertainties. Furthermore, recent studies developed by Fontenot *et al.* (2010), among others, demonstrate that sensitivity testing can be included in these risk estimations in a way that provides a level of confidence in such findings. We used similar methods in this work, though we specifically modeled the RBE for tumor induction as a function of the LET for proton beams and carbon ion beams in patient tissue. In this work, our RBE *versus* LET model had a maximum RBE value of 10 for carbon at 100 keV/μm. That maximum RBE value was approximately consistent with RBE values determined by Furusawa *et al.* (2000) for sterilization of Chinese hamster ovary cells. Additionally, Dicello *et al.* (2004) reported RBEs of 10 or less for tumor induction by iron ions in rat mammary. Although the ion species was different, their finding supports our interval of sensitivity testing.

One strength of this work was that we performed the first *in-silico* comparison of carbon ion therapy *versus* proton therapy for HL patients reported worldwide. Another strength was that we calculated risks of second cancer incidence in the breast on a voxelized basis for ion therapy considering (1) absorbed dose, (2) dose-averaged LET, (3) cell sterilization, and (4) variable RBE. In addition, we performed a broad range of sensitivity testing to understand the robustness of our risk predictions to biological uncertainties.

Another strength was that we simulated therapy without using beam margins to account for patient setup. Thus, our risk findings reflect some of the most fundamental differences between carbon-ion therapy and proton therapy. Although treatment without large setup margins might be possible in the future, e.g., using real-time magnetic resonance imaging to identify tumor position and guide particle therapy, setup margins are routinely used now. Therefore, we also simulated treatment and calculated ratios of risk with 5-mm radial beam margins added to the proton and carbon-ion treatment plans. Those data are presented in Appendix B. We found a small (approximately 4%) increase in the ratio of risk of breast cancer incidence for carbon-ion versus proton therapy when 5-mm radial margins were included, compared to plans without setup margins.

This study had several limitations. First, we only analyzed the breast as an organ at risk. Other radiation side-effects, such as risks of cardiac toxicity, lung fibrosis, and esophageal fibrosis should be addressed in future studies and might affect the ultimate conclusion as to whether carbon or proton therapy is a better choice for HL patients. In fact, all RBE_S-weighted doses computed outside the HL targets were calculated using RBE tables with α/β of 1, 3, and 5 Gy, and, therefore, our RBE-weighted dose values could be used for estimating risks to other organs having an α/β ratio of in that interval, such as the lung and heart. Second, the true RBE_T of carbon ions at 100 keV/μm for breast tumor induction might be higher than our maximum sampled value of 10. In that case, our predicted risk ratios would likely become more dependent on the exact relation between k_c and k_p. Third, we used a linear RBE *versus* LET model for tumor induction, known to fail at high LET. However, in this work we only applied this model to relatively low LET values found in the breast in the beam entrance path. Further work is required to use this model for treatment plans that might deliver higher LET distributions to the breast, *e.g.*, for a lateral beam to complement the anterior-to-posterior beam. Fourth, we only calculated 3D dose and ignored the effects of patient respiration on accumulated 4D dose. Interplay effects might occur during scanned ion delivery, and motion mitigation strategies such as those described in Chapters 2 and 3 might be required to ensure accurate dose delivery. Some of these limitations are currently being addressed in ongoing studies in our laboratory, but they did not prevent us from achieving our objective, that was to determine whether using carbon ion therapy instead of proton therapy would show a difference in the predicted risk of second cancer incidence in the breast for female HL patients

Based on the findings of our study, we propose the following future studies. First, we propose to reanalyze treatment plans, dose, and LET distributions calculated in this study using risk models for other organs at risk, *e.g.*, lung, heart, and esophagus, to better understand risks of side-effects in organs other than the breast. Second, a study focused

on organ motion and 4D dose calculation might reveal whether motion strategies, *e.g.*, 4D-optimized beam tracking, might be beneficial for this HL patient population.

In conclusion, we completed a simulation study comparing predicted risks of second cancer incidence in the breast for HL patients receiving carbon ion therapy *versus* proton therapy. We explicitly modeled the biological effectiveness of the ion fields to induce the competing processes of breast tumor induction and breast cell inactivation. Ultimately, we did not find a significant difference in the predicted risks of second cancer incidence in the breast for female HL patients using carbon ion therapy instead of proton therapy for our reference case. Rather, we found relative risk predictions to depend heavily on both the α/β ratio for breast cell sterilization and the exact relation between ion LET and the RBE for tumorigenesis.

Chapter 5

Conclusion

In conclusion, we sought to test the hypothesis that using 4D-optimized carbon-ion therapy would reduce the predicted risk of radiation induced second cancers in the breast for female Hodgkin lymphoma patients while preserving tumor control compared with proton therapy. To test our hypothesis we completed 3 specific aims.

Specific Aims

① Determine whether 4D-optimized carbon tracking therapy can reduce dose to volumes outside a moving target while maintaining adequate target dose coverage. We developed a new scanned ion beam tracking approach using 4D optimization. We performed water phantom studies and patient studies using computer simulations to compare dose distributions for moving targets and avoidance volumes for 4D versus 3D-optimized carbon tracking. In addition, we demonstrated the feasibility of our 4D-optimized carbon tracking approach in an experiment using a moving phantom and a scanned carbon ion beam.

② Quantify the impact of uncertainties in patient respiratory motion on dose distributions in moving targets for scanned carbon ion beam tracking. We simulated dose for scanned carbon ion beam tracking using mathematical phantoms and lung cancer patient 4DCTs. We tested the sensitivity of dose distributions in the target to various systematic and random errors that are characteristic for lung motion and for the scanned carbon tracking system at GSI. We also investigated the effects of interfractional changes in organ motion on target dose coverage for the lung cancer patients by simulating treatment on multi-week 4DCTs.

③ Determine whether using carbon-ion therapy instead of proton therapy reduces the predicted risk of second cancer incidence in the breast for a sample of Hodgkin lym-

phoma patients. We simulated scanned proton and scanned carbon ion treatment for 6 HL patients using a research treatment planning system for ion radiotherapy. We calculated relative predicted risks of second cancer in the breast using a linear-non-threshold tumor induction model and a linear-quadratic breast cell inactivation model. In addition, we explicitly modeled RBE for the ion fields for both breast tumor induction and cell inactivation.

With respect to our central hypothesis, we did not find a conclusive difference in the predicted risk of radiation induced second cancers in the breast for HL patients using carbon-ion therapy instead of proton therapy. However, we did find that 4D-optimized scanned ion beam tracking therapy can reduce dose to avoidance volumes near moving targets, compared to 3D-optimized scanned ion beam tracking therapy, and can be delivered with a dedicated 4D treatment control system.

Summary of Major Findings

- 4D-optimized scanned ion beam tracking therapy can reduce dose to volumes near a moving target and improve target dose homogeneity for targets in heterogeneous tissue, compared to 3D-optimized scanned ion beam tracking.

- Delivery of 4D-optimized scanned carbon ion beam tracking is technically feasible using the GSI synchrotron or its equivalent.

- 3D-optimized scanned carbon ion beam tracking is sensitive to a number of motion uncertainties that negatively impact target dose coverage.

- For HL patients, we did not find a significant difference in the predicted risk of second cancer incidence in breast using carbon-ion therapy instead of proton therapy but discovered trends in predicted risks depending on the exact biological sensitivities of breast tissue to ion irradiation.

References

Alpen E. L., Powersrisius P., Curtis S. B., and Deguzman R. Tumorigenic potential of high-z, high-let charged-particle radiations. *Radiat. Res.*, 136(3):382–391, 1993.

Armitage James O. Early-stage hodgkin's lymphoma. *New Engl. J. Med.*, 363(7):653–62, 2010.

Bert C. and Durante M. Motion in radiotherapy: particle therapy. *Phys. Med. Biol.*, 56 (16):R113–44, 2011.

Bert C. and Rietzel E. 4d treatment planning for scanned ion beams. *Radiat. Oncol.*, 2, 2007.

Bert C., Saito N., Schmidt A., Chaudhri N., Schardt D., and Rietzel E. Target motion tracking with a scanned particle beam. *Med. Phys.*, 34(12):4768–71, 2007.

Bert C., Grözinger S. O., and Rietzel E. Quantification of interplay effects of scanned particle beams and moving targets. *Phys. Med. Biol.*, 53(9):2253–65, 2008.

Bleyer A., O'Leary M., Barr R., and Ries L. A. G. Cancer epidemiology in older adolescents and young adults 15 to 29 years of age, including seer incidence and survival: 1975-2000. Technical report, National Cancer Institute, NIH, 2006.

Bortfeld T., Chan T. C. Y., Trofimov A., and Tsitsiklis J. N. Robust management of motion uncertainty in intensity-modulated radiation therapy. *Oper. Res.*, 56(6):1461–1473, 2008.

Bush D. A., Slater J. D., Shin B. B., Cheek G., Miller D. W., and Slater J. M. Hypofractionated proton beam radiotherapy for stage i lung cancer. *Chest*, 126(4):1198–1203, 2004.

Carabe A., Moteabbed M., Depauw N., Schuemann J., and Paganetti H. Range uncertainty in proton therapy due to variable biological effectiveness. *Phys. Med. Biol.*, 57(5):1159–72, 2012.

Chapman J. D. Radiobiological characterization of the inactivating events produced in mammalian cells by helium and heavy ions. *Int. J. Radiat. Oncol.*, 3:97–102, 1977.

Chapman J. D., Blakely E. A., Smith K. C., Urtasun R. C., Lyman J. T., and Tobias C. A. Radiation biophysical studies with mammalian cells and a modulated carbon ion beam. *Radiat. Res.*, 74:101–111, 1978.

Chaudri N., Saito N., Bert C., Franczak B., Steidl P., Durante M., Rietzel E., and Schardt D. Ion-optical studies for a range adaptation method in ion beam therapy using

a static wedge degrader combined with magnetic beam deflection. *Phys. Med. Biol.*, 55: 3499–3513, 2010.

Chen W., Unkelbach J., Trofimov A., Madden T., Kooy H., Bortfeld T., and Craft D. Including robustness in multi-criteria optimization for intensity-modulated proton therapy. *Phys. Med. Biol.*, 57(3):591–608, 2012.

Chera B. S., Rodriguez C., Morris C. G., Louis D., Yeung D., Li Z., and Mendenhall N. P. Dosimetric comparison of three different involved nodal irradiation techniques for stage ii hodgkin's lymphoma patients: conventional radiotherapy, intensity-modulated radiotherapy, and three-dimensional proton radiotherapy. *Int. J. Radiat. Oncol.*, 75(4):1173–80, 2009.

Chin E. and Otto K. Investigation of a novel algorithm for true 4d-vmat planning with comparison to tracked, gated and static delivery. *Med. Phys.*, 38(5):2698–707, 2011.

Coggle J. E. Lung tumour induction in mice after x-rays and neutrons. *Int. J. Radiat. Biol. Re.*, 53(4):585–97, 1988.

Dicello J. F., Christian A., Cucinotta F. A., Gridley D. S, and Kathi. In vivo mammary tumourigenesis in the spraguedawley rat and microdosimetric correlates. *Phys. Med. Biol.*, 49:3817–30, 2004.

Dores G. M., Metayer C., Curtis R. E., Lynch C. F., Clarke E. A., Glimelius B., Storm H., Pukkala E., Leeuwen F. E. van, Holowaty E. J., Andersson M., Wiklund T., Joensuu T., Veer M. B. van't, Stovall M., Gospodarowicz M., and Travis L. B. Second malignant neoplasms among long-term survivors of hodgkin's disease: a population-based evaluation over 25 years. *J. Clin. Oncol.*, 20(16):3484–94, 2002.

Durante M. and Cucinotta F. A. Heavy ion carcinogenesis and human space exploration. *Nat. Rev. Cancer*, 8(6):465–72, 2008.

Durante M., George K., Wu H., and Cucinotta F. A. Karyotypes of human lymphocytes exposed to high-energy iron ions. *Radiat. Res.*, 158(5):581–90, 2002.

Elsässer T., Weyrather W. K., Friedrich T., Durante M., Iancu G., Krämer M., Kragl G., Brons S., Winter M., Weber K. J., and Scholz M. Quantification of the relative biological effectiveness for ion beam radiotherapy: direct experimental comparison of proton and carbon ion beams and a novel approach for treatment planning. *Int. J. Radiat. Oncol.*, 78(4):1177–83, 2010.

Fontenot J. D., Bloch C., Followill D., Titt U., and Newhauser W. D. Estimate of the uncertainties in the relative risk of secondary malignant neoplasms following proton therapy and intensity-modulated photon therapy. *Phys. Med. Biol.*, 55(23):6987–98, 2010.

Friedrich T., Scholz U., Elsässer T., Durante M., and Scholz M. Calculation of the biological effects of ion beams based on the microscopic spatial damage distribution pattern. *Int. J. Radiat. Biol.*, 88(1-2):103–7, 2012.

Friedrich T., Durante M., and Scholz M. Particle species dependence of cell survival rbe: Evident and not negligible. *Acta Oncol.*, 52(3):589–603, 2013a.

Friedrich T., Scholz U., Elsässer T., Durante M., and Scholz M. Systematic analysis of rbe and related quantities using a database of cell survival experiments with ion beam irradiation. *Radiat. Res.*, 54:494–514, 2013b.

Fry R. J., Powers-Risius P., Alpen E. L., and Ainsworth E. J. High-let radiation carcinogenesis. *Radiat. Res.*, 8(Suppl.):S188–95, 1985.

Furusawa Y., Fukutsu K., Aoki M., Itsukaichi H., Eguchi-Kasai K., Ohara H., Yatagai F., Kanai T., and Ando K. Inactivation of aerobic and hypoxic cells from three different cell lines by accelerated (3)he-, (12)c- and (20)ne-ion beams. *Radiat. Res.*, 154(5):485–96, 2000.

Graeff C., Durante M., and Bert C. Motion mitigation in intensity modulated particle therapy by internal target volumes covering range changes. *Med. Phys.*, 39(10):6004–13, 2012.

Grözinger S. O., Li Q., Rietzel E., Haberer T., and Kraft G. 3d online compensation of target motion with scanned particle beam. *Radiother. Oncol.*, 73(Suppl. 2):S77–9, 2004.

Hall E. J. and Giaccia A. J. *Radiobiology for the Radiologist.* Lippincott Williams and Wilkins, Philadelphia, 6th edition, 2006.

Hanley J., Debois M. M., Mah D., Mageras G. S., Raben A., Rosenzweig K., Mychalczak B., Schwartz L. H., Gloeggler P. J., Lutz W., Ling C. C., Leibel S. A., Fuks Z., and Kutcher G. J. Deep inspiration breath-hold technique for lung tumors: the potential value of target immobilization and reduced lung density in dose escalation. *Int. J. Radiat. Oncol.*, 45(3):603–11, 1999.

Hashimoto T., Tokuuye K., Fukumitsu N., Igaki H., Hata M., Kagei K., Sugahara S., Ohara K., Matsuzaki Y., and Akine Y. Repeated proton beam therapy for hepatocellular carcinoma. *Int. J. Radiat. Oncol.*, 65(1):196–202, 2006.

Hawkins R. B. A microdosimetric-kinetic theory of the dependence of the rbe for cell death on let. *Med. Phys.*, 25(7 Pt 1):1157–70, 1998.

Hof H., Herfarth K. K., Munter M., Hoess A., Motsch J., Wannenmacher M., and Debus J. Stereotactic single-dose radiotherapy of stage i non-small-cell lung cancer (nsclc). *Int. J. Radiat. Oncol.*, 56(2):335–41, 2003.

Horcicka M. Theorie und numerik zur nichtlinearen dosisoptimierung in der schwerionentherapie. Master's thesis, Technische Universität Darmstadt, 2011.

Howlader N., Noone A. M., Krapcho M., Garshell J., Neyman N., Altekruse S. F., Kosary C. L., Yu M., Ruhl J., Tatalovich Z., Cho H., Mariotto A., Lewis D. R., Chen H. S., Feuer E. J., and Cronin K. A. Seer cancer statistics review, 1975-2010. Technical report, National Cancer Institute, NIH, 2013.

Iwata Y., Furukawa T., Noda K., Shirai T., Takada E., Kadowaki T., Sano Y., and Uchiyama H. Update of an accelerator control system for the new treatment facility at himac. In *11th European Particle Accelerator Conference*, pages 1800–2, 2008.

Kanai T., Endo M., Minohara S., Miyahara N., Koyama-ito H., Tomura H., Matsufuji N., Futami Y., Fukumura A., Hiraoka T., Furusawa Y., Ando K., Suzuki M., Soga F., and Kawachi K. Biophysical characteristics of himac clinical irradiation system for heavy-ion radiation therapy. *Int. J. Radiat. Oncol.*, 44:201–210, 1999.

Kanai T. Y., Furusawa K., Itsukaichi H., Eguchi-Kasai K., and Ohara H. Irradiation of mixed beam and design of spread-out bragg peak for heavy-ion radiotherapy. *Radiat. Res.*, 147:78–85, 1997.

Keall P. J., Starkschall G., Shukla H., Forster K. M., Ortiz V., Stevens C. W., Vedam S. S., George R., Guerrero T., and Mohan R. Acquiring 4D thoracic CT scans using a multislice helical method. *Phys. Med. Biol.*, 49(10):2053–67, 2004.

Koh E. S., Tran T. H., Heydarian M., Sachs R. K., Tsang R. W., Brenner D. J., Pintilie M., Xu T., Chung J., Paul N., and Hodgson D. C. A comparison of mantle versus involved-field radiotherapy for hodgkin's lymphoma: reduction in normal tissue dose and second cancer risk. *Radiat. Oncol.*, 2, 2007.

Koto M., Miyamoto T., Yamamoto N., Nishimura H., Yamada S., and Tsujii H. Local control and recurrence of stage i non-small cell lung cancer after carbon ion radiotherapy. *Radiother. Oncol.*, 71(2):147–56, 2004.

Kraft G. Tumor therapy with heavy charged particles. *Prog. Part. Nucl. Phys.*, 45(Suppl. 2):S473–544, 2000.

Krämer M. and Scholz M. Treatment planning for heavy-ion radiotherapy: calculation and optimization of biologically effective dose. *Phys. Med. Biol.*, 45(11):3319–30, 2000.

Krämer M. and Scholz M. Rapid calculation of biological effects in ion radiotherapy. *Phys. Med. Biol.*, 51:1959–70, 2006.

Krämer M., Jäkel O., Haberer T., Kraft G., Schardt D., and Weber U. Treatment planning for heavy-ion radiotherapy: physical beam model and dose optimization. *Phys. Med.*

Biol., 45(11):3299–317, 2000.

Lambert J., Suchowerska N., McKenzie D. R., and Jackson M. Intrafractional motion during proton beam scanning. *Phys. Med. Biol.*, 50(20):4853–62, 2005.

Leo W. R. *Techniques for Nuclear and Particle Physics Experiments - A How-to Approach.* Springer-Verlag, Berlin, 2nd edition, 1994.

Liu W., Zhang X., Li Y., and Mohan R. Robust optimization of intensity modulated proton therapy. *Med. Phys.*, 39(2):1079–91, 2012.

Lomax A. J. Intensity modulated proton therapy and its sensitivity to treatment uncertainties 1: the potential effects of calculational uncertainties. *Phys. Med. Biol.*, 53(4): 1027–42, 2008a.

Lomax A. J. Intensity modulated proton therapy and its sensitivity to treatment uncertainties 2: the potential effects of inter-fraction and inter-field motions. *Phys. Med. Biol.*, 53(4):1043–56, 2008b.

Lu H. M., Brett R., Sharp G., Safai S., Jiang S., Flanz J., and Kooy H. A respiratory-gated treatment system for proton therapy. *Med. Phys.*, 34(8):3273–8, 2007.

Lüchtenborg R. *Real-time dose compensation methods for scanned ion beam therapy of moving tumors.* PhD thesis, Technische Universität Darmstadt, 2011.

Lüchtenborg R., Saito N., Durante M., and Bert C. Experimental verification of a real-time compensation functionality for dose changes due to target motion in scanned particle therapy. *Med. Phys.*, 38(10):5448–58, 2011.

Lujan A. E., Larsen E. W., Balter J. M., and Ten Haken R. K. A method for incorporating organ motion due to breathing into 3d dose calculations. *Med. Phys.*, 26(5):715–20, 1999.

Lyman J. T. and Howard J. Dosimetry and instrumentation for helium and heavy ions. *Int. J. Radiat. Oncol.*, 3:81–5, 1977.

Marks L. B., Ten Haken R. K., and Martel M. K. *Int. J. Radiat. Oncol.*, 76(Suppl. 3), 2010.

Mayahara H., Murakami M., Kagawa K., Kawaguchi A., Oda Y., Miyawaki D., Sasaki R., Sugimura K., and Hishikawa Y. Acute morbidity of proton therapy for prostate cancer: The hyogo ion beam medical center experience. *Int. J. Radiat. Oncol.*, 69(2):434–43, 2007.

Meyer J., Bluett J., Amos R., Levy L., Choi S., Nguyen Q. N., Zhu X. R., Gillin M., and Lee A. Spot scanning proton beam therapy for prostate cancer: treatment planning technique and analysis of consequences of rotational and translational alignment errors. *Int. J. Radiat. Oncol.*, 78(2):428–34, 2010.

Minohara S., Kanai T., Endo M., Noda K., and Kanazawa M. Respiratory gated irradiation system for heavy-ion radiotherapy. *Int. J. Radiat. Oncol.*, 47(4):1097–103, 2000.

Miyamoto T., Baba M., Sugane T., Nakajima M., Yashiro T., Kagei K., Hirasawa N., Sugawara T., Yamamoto N., Koto M., Ezawa H., Kadono K., Tsujii H., Mizoe J. E., Yoshikawa K., Kandatsu S., and Fujisawa T. Carbon ion radiotherapy for stage i non-small cell lung cancer using a regimen of four fractions during 1 week. *J. Thorac. Oncol.*, 2(10):916–26, 2007.

Mohr M., Abrams E., Engel C., Long W. B., and Bottlang M. Geometry of human ribs pertinent to orthopedic chest-wall reconstruction. *J. Biomech.*, 40(6):1310–7, 2007.

NCRP. Information needed to make radiation protection recommendations for space missions beyond low-earth orbit. Technical Report 153, 2006.

Newhauser W. D. and Durante M. Assessing the risk of second malignancies after modern radiotherapy. *Nat. Rev. Cancer*, 11(6):438–48, 2011.

Newhauser W. D., Fontenot J. D., Mahajan A., Kornguth D., Stovall M., Zheng Y., Taddei P. J., Mirkovic D., Mohan R., Cox J. D., and Woo S. The risk of developing a second cancer after receiving craniospinal proton irradiation. *Phys. Med. Biol.*, 54(8):2277–91, 2009.

Nihei K., Ogino T., Ishikura S., Kawashima M., Nishimura H., Arahira S., and Onozawa M. Phase ii feasibility study of high-dose radiotherapy for prostate cancer using proton boost therapy: First clinical trial of proton beam therapy for prostate cancer in japan. *Jpn. J. Clin. Oncol.*, 35(12):745–52, 2005.

Nihei K., Ogino T., Ishikura S., and Nishimura H. High-dose proton beam therapy for stage i non-small-cell lung cancer. *Int. J. Radiat. Oncol.*, 65(1):107–11, 2006.

Nohadani O., Seco J., and Bortfeld T. Motion management with phase-adapted 4d-optimization. *Phys. Med. Biol.*, 55(17):5189–202, 2010.

NRC. Health risks from exposure to low levels of ionizing radiation - beir vii phase 2. Technical report, 2006.

NRC. *Managing Space Radiation Risk in the New Era of Space Exploration*. National Academies Press, Washington D.C., 2008.

Pan T., Lee T. Y., Rietzel E., and Chen G. T. 4d-ct imaging of a volume influenced by respiratory motion on multi-slice ct. *Med. Phys.*, 31(2):333–40, 2004.

Park P. C., Zhu X. R., Lee A. K., Sahoo N., Melancon A. D., Zhang L., and Dong L. A beam-specific planning target volume (ptv) design for proton therapy to account for setup and range uncertainties. *Int. J. Radiat. Oncol.*, 82(2):e329–36, 2012.

Pflugfelder D., Wilkens J. J., Szymanowski H., and Oelfke U. Quantifying lateral tissue heterogeneities in hadron therapy. *Med. Phys.*, 34(4):1506–13, 2007.

Pflugfelder D., Wilkens J. J., and Oelfke U. Worst case optimization: a method to account for uncertainties in the optimization of intensity modulated proton therapy. *Phys. Med. Biol.*, 53(6):1689–1700, 2008.

Phillips M. H., Pedroni E., Blattmann H., Boehringer T., Coray A., and Scheib S. Effects of respiratory motion on dose uniformity with a charged particle scanning method. *Phys. Med. Biol.*, 37(1):223–34, 1992.

Press W. H., Teukolsky S. A., Vetterling W. T., and Flannery B. P. *Numerical Recipes - The Art of Scientific Computing.* Cambridge University Press, Cambridge, 3rd edition, 2007.

Richter D., Schwarzkopf A., Trautmann J., Krmer M., Durante M., Jäkel O., and Bert C. Upgrade and benchmarking of a 4d treatment planning system for scanned ion beam therapy. *Med. Phys.*, 40(5):051722, 2013.

Robison L. L., Mertens A. C., Boice J. D., Breslow N. E., Donaldson S. S., Green D. M., Li F. P., Meadows A. T., Mulvihill J. J., Neglia J. P., Nesbit M. E., Packer R. J., Potter J. D., Sklar C. A., Smith M. A., Stovall M., Strong L. C., Yasui Y., and Zeltzer L. K. Study design and cohort characteristics of the childhood cancer survivor study: A multi-institutional collaborative project. *Med. Pediatr. Oncol.*, 38(4):229–239, 2002.

Rossi B. and Greisen K. Cosmic-ray theory. *Rev. Mod. Phys.*, 13:240–315, 1941.

RPTC. Erfahrungsbericht zweiter monat klinischer betrieb rptc (may 2009). Technical report, 2011.

Saito N., Bert C., Chaudhri N., Gemmel A., Schardt D., Durante M., and Rietzel E. Speed and accuracy of a beam tracking system for treatment of moving targets with scanned ion beams. *Phys. Med. Biol.*, 54(16):4849–4862, 2009.

Schardt D., Elsässer T., and Schulz-Ertner D. Heavy-ion tumor therapy: Physical and radiobiological benefits. *Rev. Mod. Phys.*, 82(1):383–425, 2010.

Schneider U., Zwahlen D., Ross D., and Kaser-Hotz B. Estimation of radiation-induced cancer from three-dimensional dose distributions: Concept of organ equivalent dose. *Int. J. Radiat. Oncol.*, 61(5):1510–5, 2005.

Schneider U., Sumila M., Robotka J., Gruber G., Mack A., and Besserer J. Dose-response relationship for breast cancer induction at radiotherapy dose. *Radiat. Oncol.*, 6:67, 2011.

Schneider W., Bortfeld T., and Schlegel W. Correlation between ct numbers and tissue parameters needed for monte carlo simulations of clinical dose distributions. *Phys. Med.*

Biol., 45(2):459–78, 2000.

Scholz M. Effects of ion radiation on cells and tissues. *Adv. Polym. Sci.*, 62:96–155, 2003.

Scholz M., Kellerer A. M., Kraft-Weyrather W., and Kraft G. Computation of cell survival in heavy ion beams for therapy - the model and its approximation. *Radiat. Environ. Bioph.*, 36(1):59–66, 1997.

Schulz-Ertner D., Nikoghosyan A., Thilmann C., Haberer T., Jäkel O., Karger C., Kraft G., Wannenmacher M., and Debus J. Results of carbon ion radiotherapy in 152 patients. *Int. J. Radiat. Oncol.*, 58(2):631–40, 2004.

Shackleford J. A., Kandasamy N., and Sharp G. C. On developing b-spline registration algorithms for multi-core processors. *Phys. Med. Biol.*, 55(21):6329–51, 2010.

Slater J. D., Yonemoto L. T., Rossi C. J., Reyes-Molyneux N. J., Bush D. A., Antoine J. E., Loredo L. N., Schulte R. W. M., Teichman S. L., and Slater J. M. Conformal proton therapy for prostate carcinoma. *Int. J. Radiat. Oncol.*, 42(2):299–304, 1998.

Travis L. B., Hill D. A., Dores G. M., Gospodarowicz M., van Leeuwen F. E., Holowaty E., Glimelius B., Andersson M., Wiklund T., Lynch C. F., Van't Veer M. B., Glimelius I., Storm H., Pukkala E., Stovall M., Curtis R., Boice Jr., J. D., and Gilbert E. Breast cancer following radiotherapy and chemotherapy among young women with hodgkin disease. *J. Am. Med. Assoc.*, 290(4):465–75, 2003.

Trofimov A., Rietzel E., Lu H. M., Martin B., Jiang S., Chen G. T., and Bortfeld T. Temporo-spatial imrt optimization: concepts, implementation and initial results. *Phys. Med. Biol.*, 50(12):2779–98, 2005.

Tsuji H., Yanagi T., Ishikawa H., Kamada T., Mizoe J. E., Kanai T., and Morita S. R. Hypofractionated radiotherapy with carbon ion beams for prostate cancer. *Int. J. Radiat. Oncol.*, 63(4):1153–60, 2005.

Tsujii H., Mizoe J. E., Kamada T., Baba M., Kato S., Kato H., Tsuji H., Yamada S., Yasuda S., Ohno T., Yanagi T., Hasegawa A., Sugawara T., Ezawa H., Kandatsu S., Yoshikawa K., Kishimoto R., and Miyamoto T. Overview of clinical experiences on carbon ion radiotherapy at nirs. *Radiother. Oncol.*, 73(Suppl. 2):S41–9, 2004.

Tsunashima Y., Vedam S., Dong L., Umezawa M., Sakae T., Bues M., Balter P., Smith A., and Mohan R. Efficiency of respiratory-gated delivery of synchrotron-based pulsed proton irradiation. *Phys. Med. Biol.*, 53(7):1947–1959, 2008.

Unkelbach J. Including geometrical uncertainties in imrt and impt optimization. *Radiother. Oncol.*, 84:S90, 2007.

Unkelbach J., Bortfeld T., Martin B. C., and Soukup M. Reducing the sensitivity of

impt treatment plans to setup errors and range uncertainties via probabilistic treatment planning. *Med. Phys.*, 36(1):149–63, 2009.

Water S. van de, Kreuger R., Zenklusen S., Hug E., and Lomax A. J. Tumour tracking with scanned proton beams: assessing the accuracy and practicalities. *Phys. Med. Biol.*, 54(21):6549–63, 2009.

Weber U. and Kraft G. Design and construction of a ripple filter for a smoothed depth dose distribution in conformal particle therapy. *Phys. Med. Biol.*, 44(11):2765–75, 1999.

Weber U. and Kraft G. Comparison of carbon ions versus protons. *Cancer J.*, 15(4):325–32, 2009.

Weyrather W. K., Ritter S., Scholz M., and Kraft G. Rbe for carbon track-segment irradiation in cell lines of differing repair capacity. *Int. J. Radiat. Biol.*, 75(11):1357–64, 1999.

Wong J. W., Sharpe M. B., Jaffray D. A., Robertson J. M., Stromberg J. S., Kini V. R., and Martinez A. A. The use of active breathing control (abc) to minimize breathing motion during radiation therapy. *Int. J. Radiat. Oncol.*, 39(2):164, 1997.

Yarnold J., Ashton A., Bliss J., Homewood J., Harper C., Hanson J., Haviland J., Bentzen S., and Owen R. Fractionation sensitivity and dose response of late adverse effects in the breast after radiotherapy for early breast cancer: long-term results of a randomised trial. *Radiother. Oncol.*, 75:9–17, 2005.

Yarnold J. R., Price P., and Steel G. G. Non-surgical management of early breast cancer in the united kingdom: Radiotherapy fractionation practices. *Clin. Oncol.*, 7:223–6, 1995.

Zhang T., Jeraj R., Keller H., Lu W., Olivera G. H., McNutt T. R., Mackie T. R., and Paliwal B. Treatment plan optimization incorporating respiratory motion. *Med. Phys.*, 31(6):1576–86, 2004.

Appendix A: Additional Results for Beam Tracking Robustness Study

Results from the robustness studies in Chapter 3 that were not presented in the text are included here.
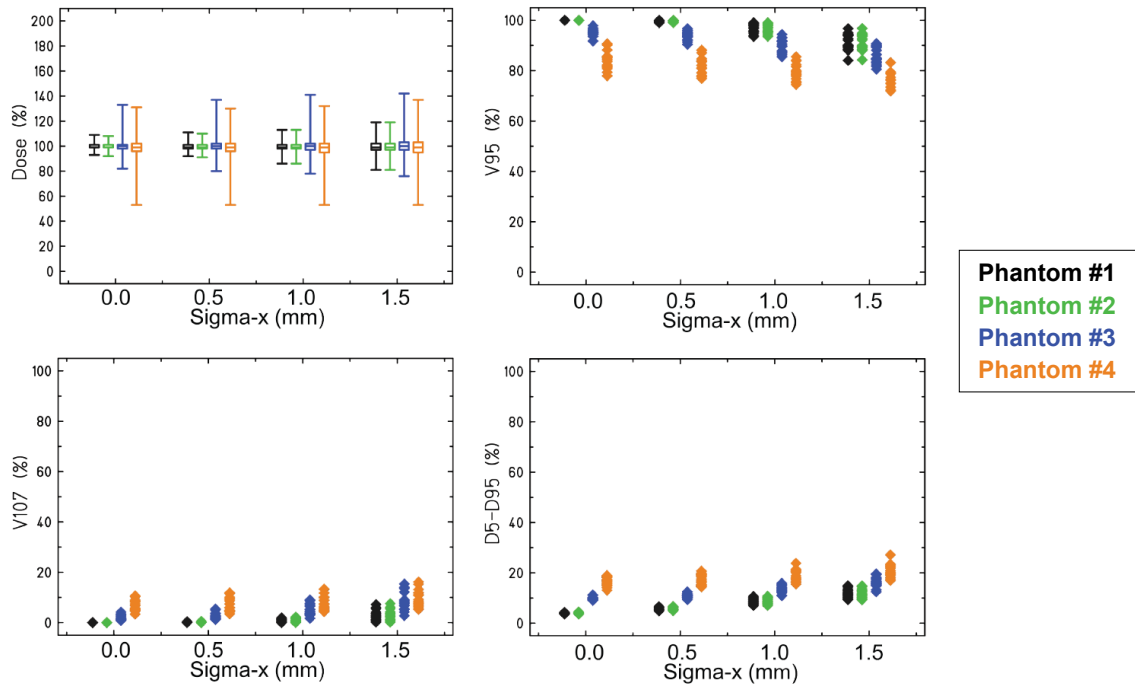
Figure A.1: Robustness of target dose coverage to random errors in tracking x-coordinates shown for the 4 phantoms. Target dose coverage V_{95} (top right) and dose homogeneity $D_5 - D_{95}$ (bottom right) are seen to degrade when random errors are added with $\sigma_x > 0.5$ mm.
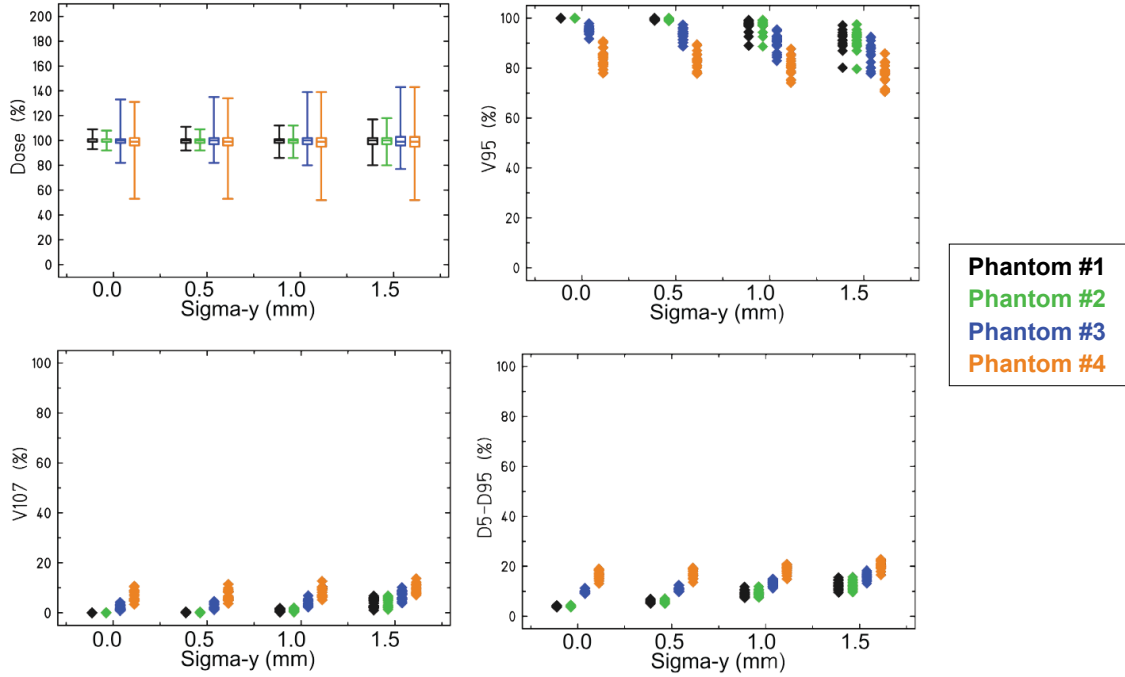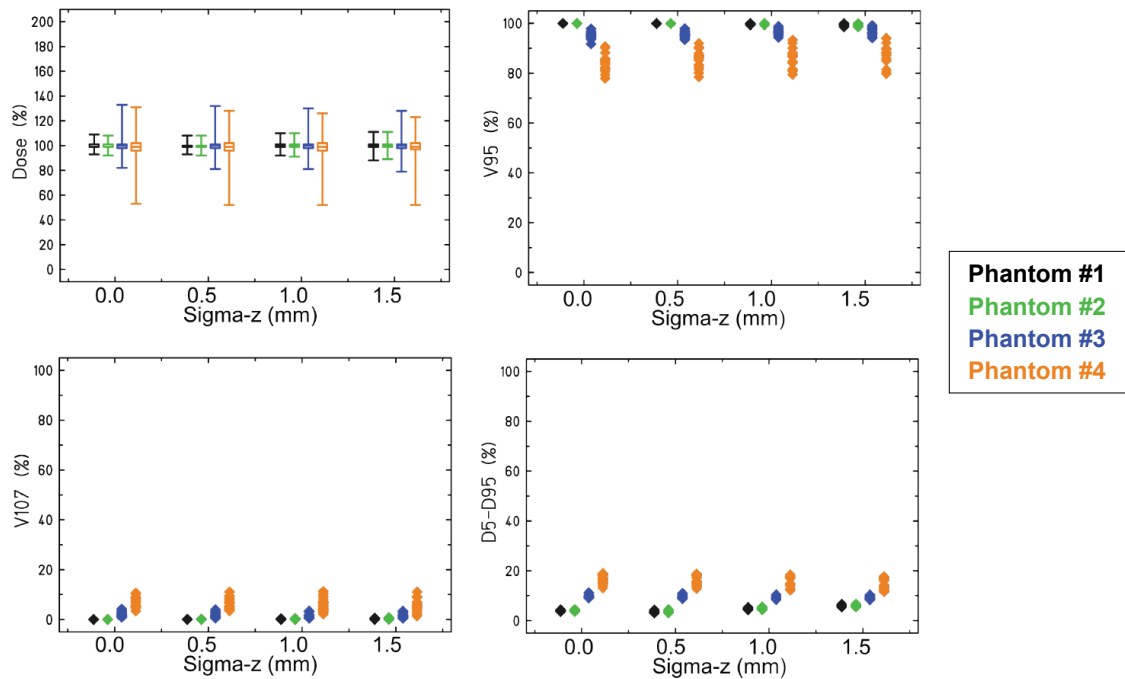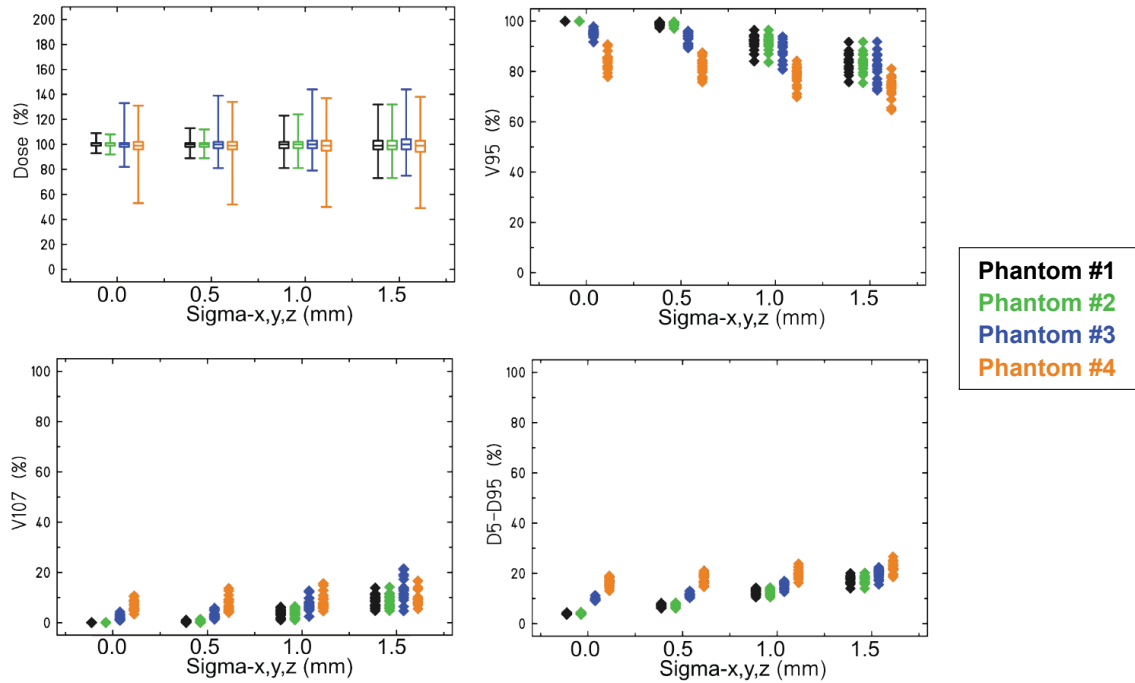
Figure A.2: Robustness of target dose coverage to random errors in tracking y-coordinates shown for the 4 phantoms. Target dose coverage V_{95} (top right) and dose homogeneity $D_5 - D_{95}$ (bottom right) are seen to degrade when random errors are added with $\sigma_y > 0.5$ mm.

Figure A.3: Robustness of target dose coverage to random errors in tracking z-coordinates shown for the 4 phantoms. Minimal changes in target dose coverage are seen.

Figure A.4: Robustness of target dose coverage to random errors in tracking x-, y-, and z-coordinates shown for the 4 phantoms. Target dose coverage V_{95} (top right) and dose homogeneity $D_5 - D_{95}$ (bottom right) are seen to degrade when random errors are added with $\sigma > 0.5$ mm. Similarly, the volume of overdose V_{107} (bottom left) increases when $\sigma > 0.5$ mm.
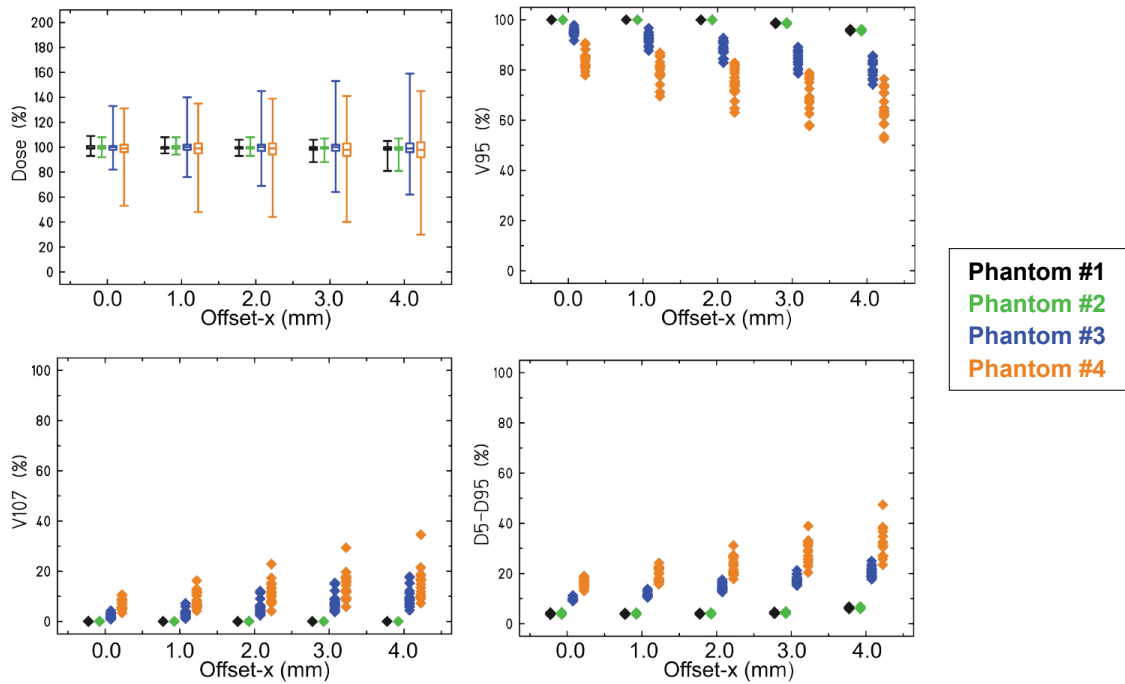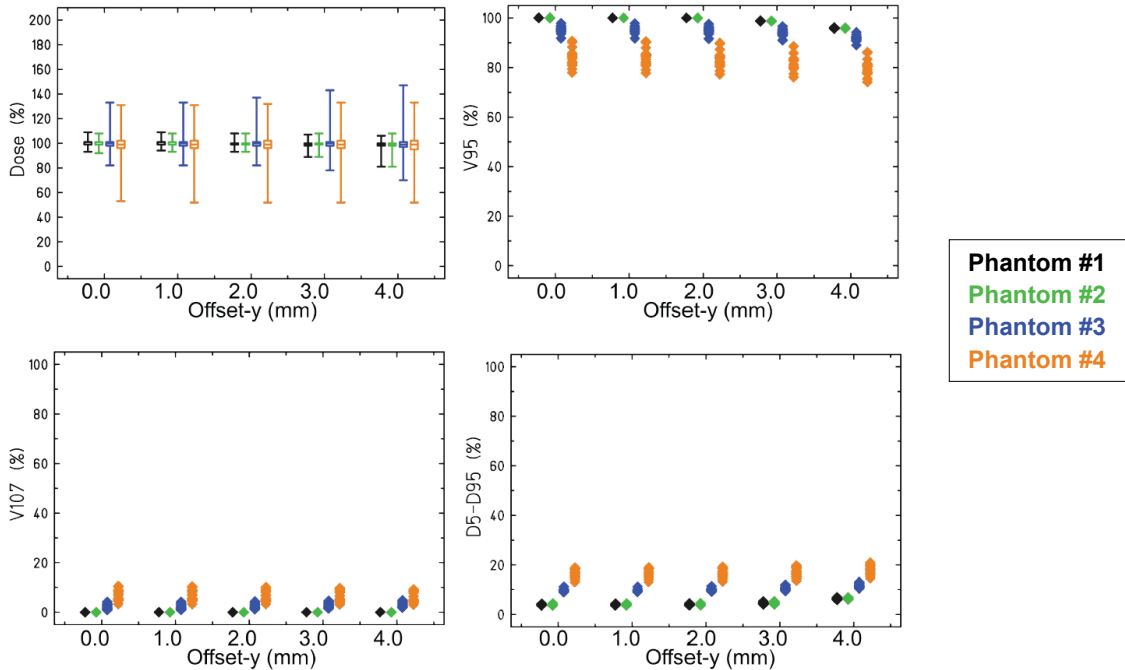
Figure A.5: Robustness of target dose coverage to systematic errors in tracking x-coordinates shown for the 4 phantoms. Note that the impact of x-axis offset is greatest for Phantom #4 (orange markers), since even small x-axis offset may also introduce more complicated range shifts due to the air cavity upstream of the target. A similar effect is seen for Phantom #3 (blue markers), which contained a rib heterogeneity upstream of the target. Phantoms #1 and #2 are homogeneous and exhibit negligible dependence on x-axis shifts until the shifts are large enough at 3 to 4 mm so that the target is relatively close to the lateral field edge boundary where multiple Coulomb scatter equilibrium conditions begin to deteriorate. Increase in overdose (V_{107}) with x-offset is also seen for Phantoms #3 and #4.

Figure A.6: Robustness of target dose coverage to systematic errors in tracking y-coordinates shown for the 4 phantoms. Very little effect on target dose coverage is seen until the y-offsets are greater than 2 mm.
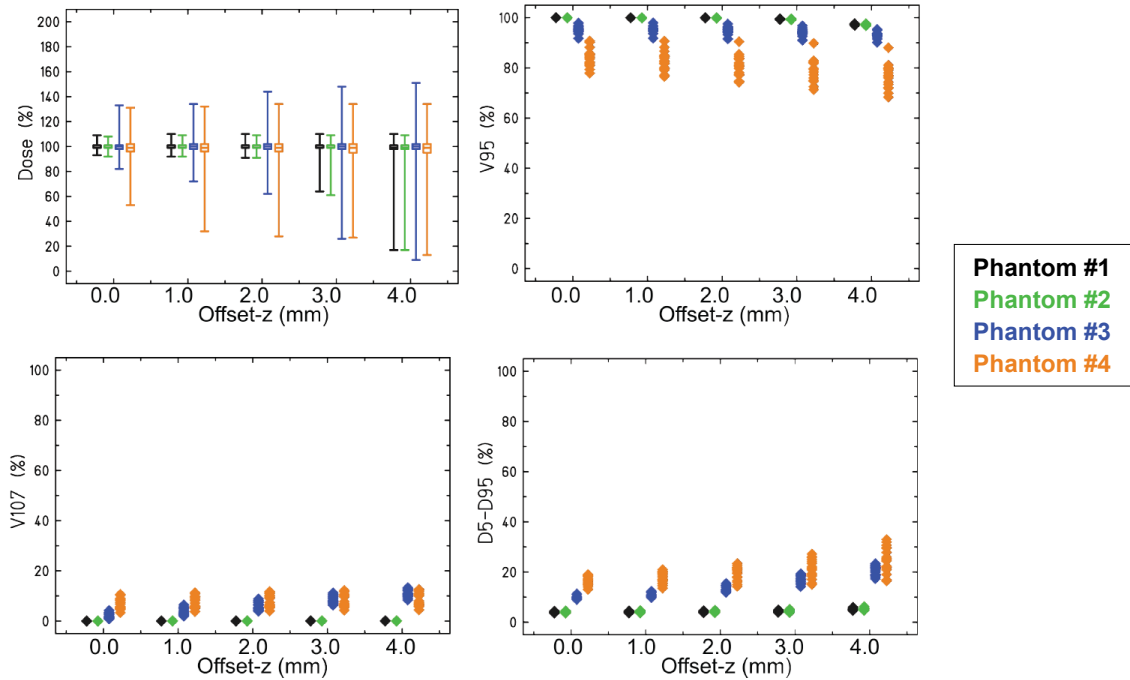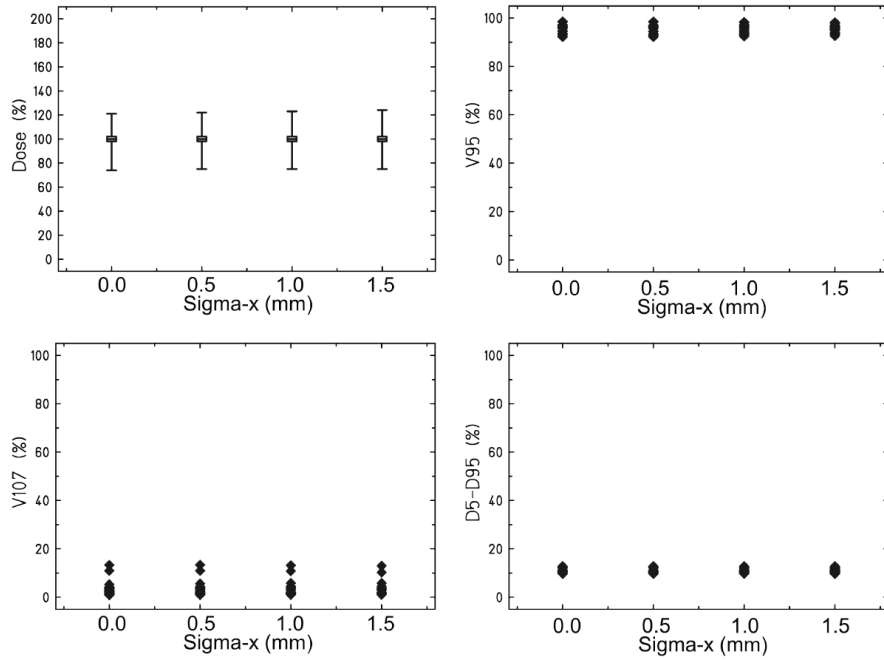

Figure A.7: Robustness of target dose coverage to systematic errors in tracking z-coordinates shown for the 4 phantoms. Very little effect on target dose coverage is seen until the z-offsets are greater than 2 mm.

Figure A.8: Robustness of target dose coverage to random errors in tracking x-coordinates shown for Lung Patient #1. Minimal effects are seen for this interval of simulated errors.
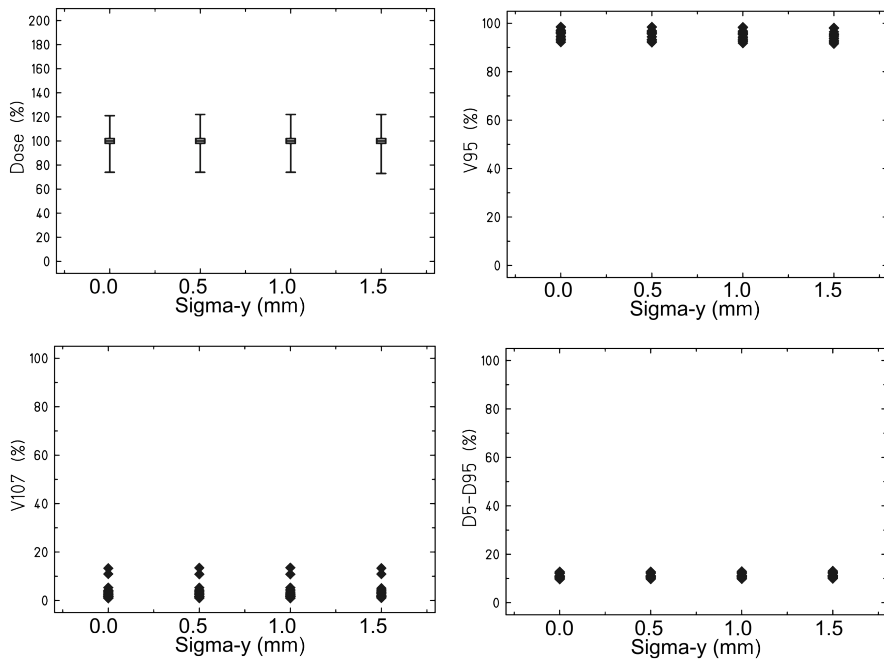
Figure A.9: Robustness of target dose coverage to random errors in tracking y-coordinates shown for Lung Patient #1. Minimal effects are seen for this interval of simulated errors.
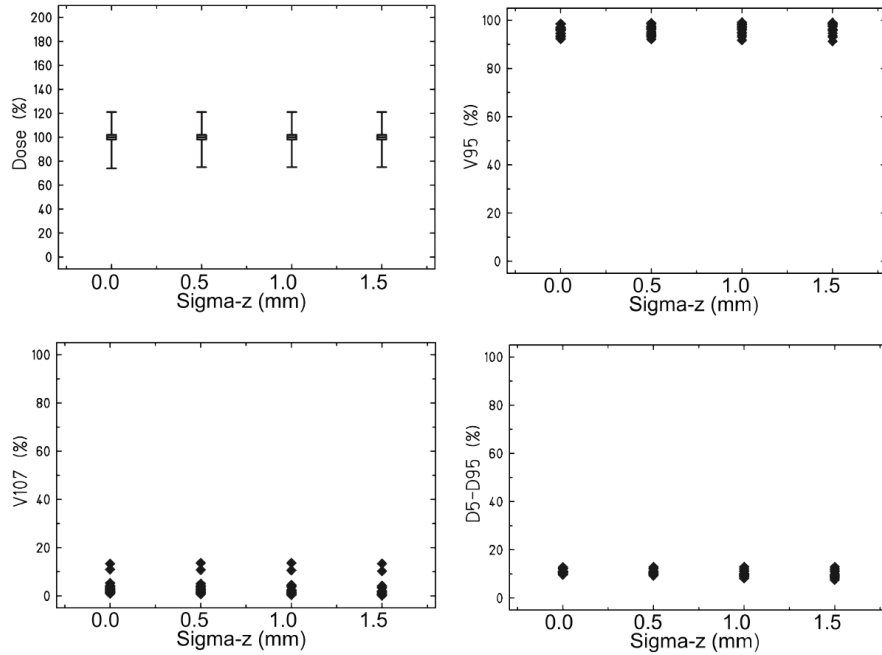
Figure A.10: Robustness of target dose coverage to random errors in tracking z-coordinates shown for Lung Patient #1. Slight effects on target dose coverage are seen for this interval of simulated errors.
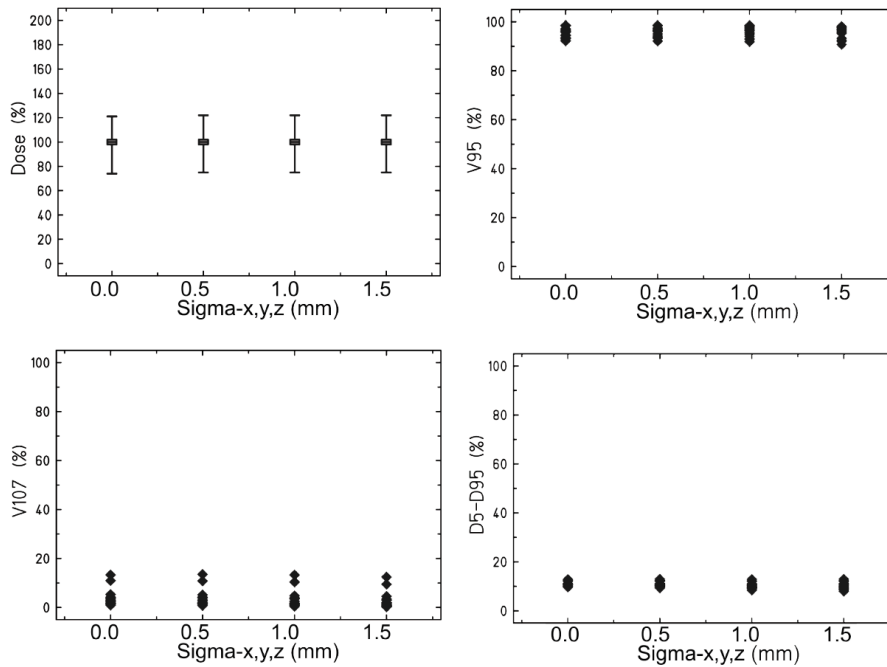

Figure A.11: Robustness of target dose coverage to random errors in tracking x-, y-, and z-coordinates shown for Lung Patient #1. Slight effects on target dose coverage are seen for $\sigma \geq 0.5$ mm.
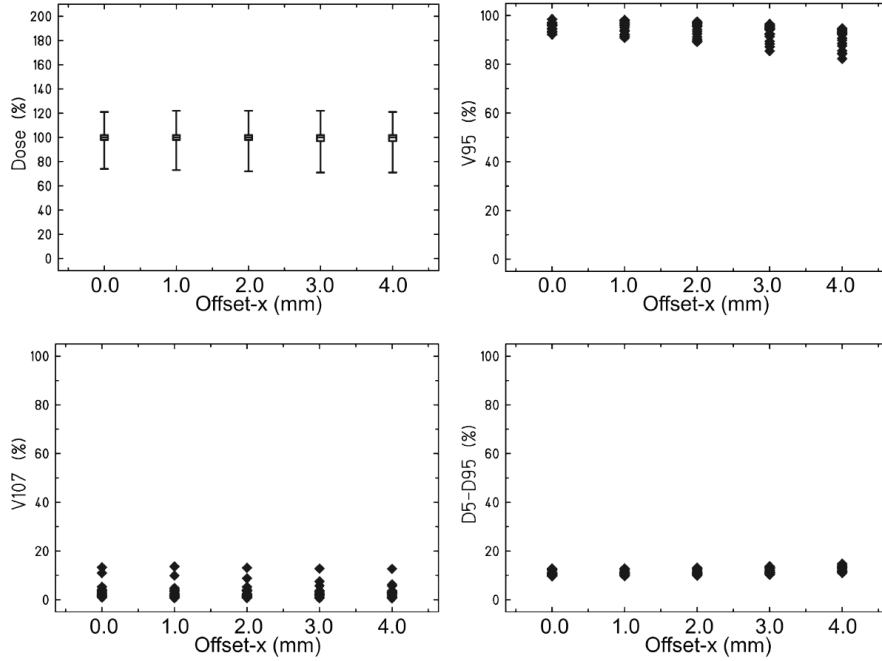
Figure A.12: Robustness of target dose coverage to systematic errors in tracking x-coordinates shown for Lung Patient #1. A decrease in V_{95} is seen with increasing magnitude of x-offset.
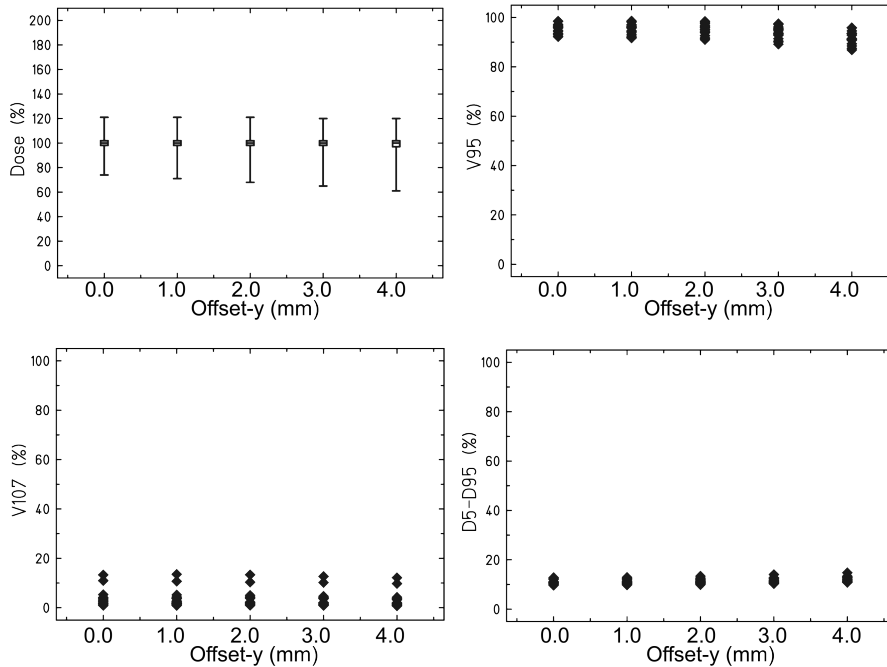

Figure A.13: Robustness of target dose coverage to systematic errors in tracking y-coordinates shown for Lung Patient #1. Very little effect on target dose coverage is seen until the z-offsets are greater than 2 mm.
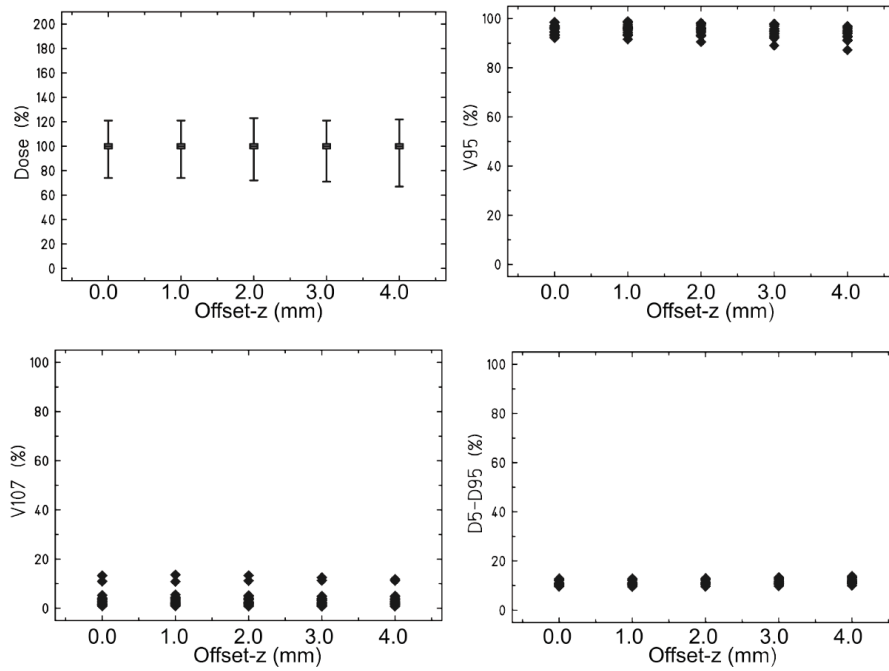
Figure A.14: Robustness of target dose coverage to systematic errors in tracking z-coordinates shown for Lung Patient #1. A gradual decrease in V_{95} is seen with increasing magnitude of z-offset.

Table A.1: Robustness of 4D-optimized beam tracking to interfractional changes in organ motion for Lung Patient #1. Dose and volume statistics compare treatment simulated on an initial planning 4DCT (i.e., Week 0) and a follow-up 4DCT acquired one week later (i.e., Week 1). Target dose coverage V_{95} degraded after one week by 11% but was better than that of 3D-optimized beam tracking at both Week 0 and Week 1 (cf. Figure 3.15). Maximum dose to the heart increased by 11% but remained lower than that for 3D-optimized beam tracking (see Table 2.1). Data reported as percentages. Difference calculated by subtracting the week 0 values from the week 1 values.

Volume	Metric	Week 0	Week 1	Difference (%)
CTV	$\bar{D}$	99.9	97.8	-2
	σ_D	0.9	6.2	+5
	$D_{\min}$	54.2	29.0	-25
	$D_{\max}$	109.7	108.4	-1
	V_{95}	99.9	88.9	**-11**
	V_{107}	0.1	0.1	0
	$D_5 - D_{95}$	1.8	13.4	+12
Heart	$\bar{D}$	7.1	11.8	+5
	$D_{\max}$	104.0	114.8	**+11**

Appendix B: Additional Results for Second Cancer Risk Study

Results from the second cancer risk study in Chapter 4 that were not presented in the text are included here.
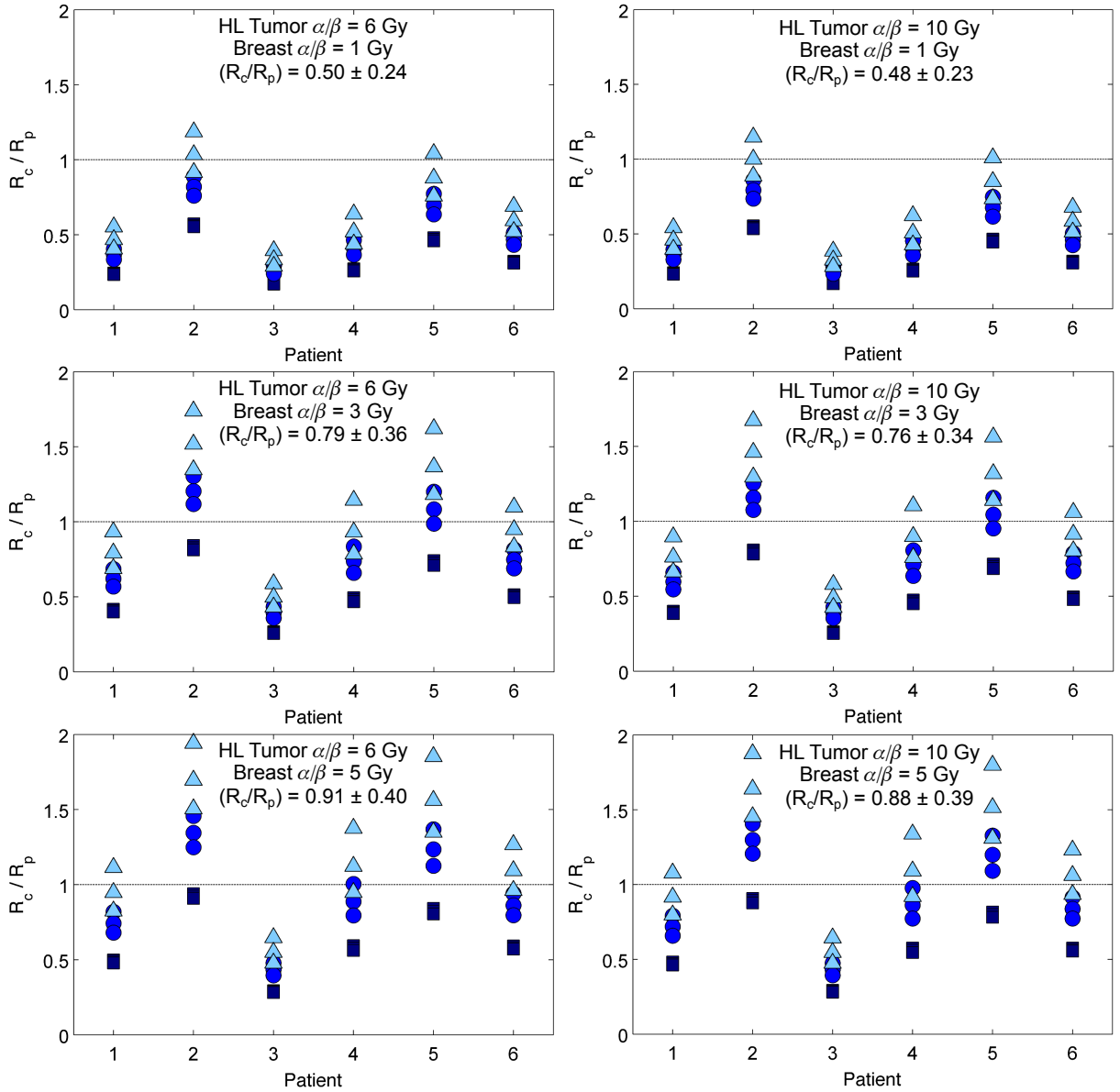
Figure B.1: Predicted ratio of risk (R_c/R_p) for breast cancer incidence for the 6 HL patients receiving scanned carbon versus scanned proton therapy when α/β for the HL target was 6 Gy (left) and 10 Gy (right) and α/β for the breast was 1 Gy (top), 3 Gy (middle), and 5 Gy (bottom). The various data points in each plot represent the k_p and k_c values for our sensitivity testing described in Chapter 4. The mean and standard deviation of (R_c/R_p) for all points are annotated for each plot. Importantly, our findings are seen to have only minimal dependence on the exact value of α/β for the HL target in the range of 6-10 Gy. However, strong dependence on the exact α/β value for the breast is seen in the range of 1-5 Gy.
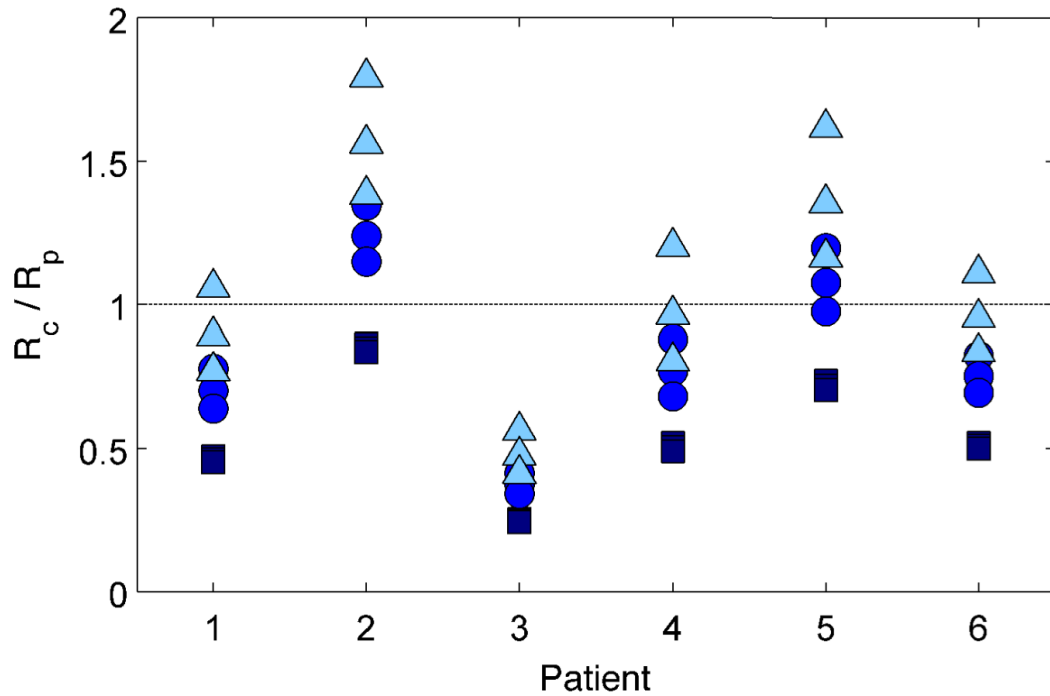
Figure B.2: Predicted ratio of risk (R_c/R_p) for breast cancer incidence for the 6 HL patients receiving scanned carbon versus scanned proton therapy when 5-mm radial beam margins are added to mitigate uncertainty in patient setup. α/β for the HL target was 8 Gy and α/β for the breast was 3 Gy. The various data points in each plot represent the k_p and k_c values for our sensitivity testing described in Chapter 4. For all points here, (R_c/R_p) was 0.81 ± 0.36. Increasing the radial beam margin increased the amount of breast tissue exposed to radiation for both proton therapy and carbon-ion therapy. However, we observed less than a 5% difference in our mean predicted risk ratios between these calculations including radial margins and those calculations presented in Chapter 4, which did not include margins for patient setup errors (cf. Figure 4.12).

Vita

John Gordon Eley was born in Jackson, Mississippi in 1983. He grew up with his parents and two sisters until his graduation from Saint Andrew's Episcopal School in 2001. Later that year, he moved to Charleston, South Carolina to attend the College of Charleston and pursue a Bachelor of Science in physics that he earned in 2005. From 2006 to 2009, he completed a Master of Science in medical physics at Louisiana State University. Afterwards, John moved to Houston, Texas to begin work on his doctorate in medical physics at The University of Texas M. D. Anderson Cancer Center. In 2010, he traveled to Darmstadt, Germany to work at the GSI Helmholtz Center for Heavy Ion Research. In 2011, John was married to his wife Dargan in Charleston. He plans to continue working as a physicist in the research field of ion radiotherapy.